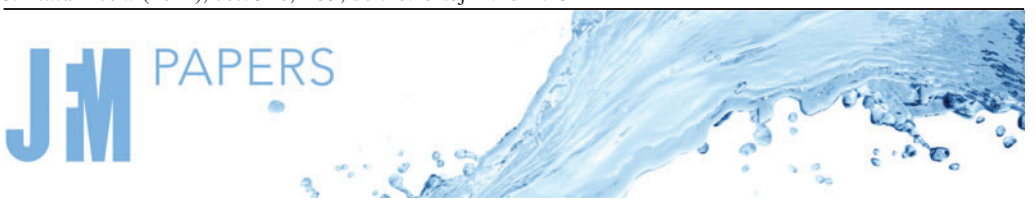
CrossMark

J. Fluid Mech. (2022), *vol*. 940, A39, doi:10.1017/jfm.2022.252



Nonlinear evolution and low-frequency acoustic radiation of ring-mode coherent structures on subsonic turbulent circular jets

Zhongyu Zhang[1] **and Xuesong Wu**[2,3],†

[1]Laboratory of High-Speed Aerodynamics, School of Mechanical Engineering, Tianjin University, Tianjin 300072, PR China

[2]School of Mechanical Engineering, Nantong University, Nantong 226019, PR China

[3]Department of Mathematics, Imperial College London, 180 Queen's Gate, London SW7 2AZ, UK

(Received 20 May 2021; revised 12 February 2022; accepted 16 March 2022)

By adapting the triple decomposition of an instantaneous turbulent flow into a time-averaged mean field, large-scale coherent motion and fine-scale random fluctuations, and treating the coherent motion as instability modes on the mean flow, a mathematical theory is developed to describe the nonlinear spatial–temporal modulation and acoustic radiation of a coherent structure (CS) on a circular jet in the form of a wavepacket consisting of an axisymmetric (ring) mode and its sideband components. The effect of fine-scale turbulence on the CS is characterised via a gradient closure model, and the non-parallelism due to the axial variation and radial velocity of the mean flow is taken into account. By employing the matched asymptotic expansion and multi-scale techniques, a strongly nonlinear system is derived, which governs the envelope of the CS and its vorticity and temperature in the critical layer. Numerical solutions to the evolution system show that the theory captures the nonlinear amplitude attenuation and vorticity roll-up as observed in experiments. The large-distance asymptotic properties of the CS allow us to describe and predict its acoustic radiation on the basis of first principles. The CS is trapped within the jet, but its self-interaction generates a temporally and axially modulated mean-flow distortion, which acts as the emitter to radiate low-frequency sound waves, with the Reynolds stresses driving this mean-flow distortion being identified unambiguously to be the physical source in the present context. An equivalent source in the Lighthill type of acoustic analogy is also identified. For the present ring-mode CS in the fully developed region of a circular jet, the equivalent source can be determined before the acoustic field is, and the intensity of the radiated sound waves is found to be $O(\epsilon^3)$, where ϵ measures the magnitude of the CS. The directivity and spectrum of the acoustic far field are

† Email address for correspondence: x.wu@imperial.ac.uk

© The Author(s), 2022. Published by Cambridge University Press

https://doi.org/10.1017/jfm.2022.252 Published online by Cambridge University Press

calculated for representative parameters, and the predicted features resemble experimental measurements.

Key words: aeroacoustics, jet noise, shear-flow instability

1. Introduction

The present paper continues our efforts towards advancing high-Reynolds-number asymptotic approaches that describe, on the basis of first principles, acoustic radiation of nonlinearly evolving coherent structures (CS) on turbulent shear flows. Such a theory was presented for CS on a subsonic mixing layer in a recent paper (Zhang & Wu 2020, hereafter referred to as '[I]'), as a sequel to which the present work is to develop a corresponding theory for a circular jet. Since a detailed introduction to CS and aeroacoustics as well as a fairly comprehensive review of relevant previous studies can be found in [I], the literature survey in the following will focus on circular jets.

As one of the most significant contributors to overall aircraft noise, jet noise has been the focal point of aeroacoustics research for many decades, and a wealth of knowledge and data has been acquired about its characteristics as well as the mechanisms of its generation (Ffowcs Williams 1969, 1977; Goldstein 1984; Tam 1995). Jet noise has a broadband spectrum and consists of mixing noise (Mollo-Christensen, Kolpin & Martuccelli 1964; Seiner 1984), broadband shock-associated noise (Harper-Bourne & Fisher 1974; Tam 1991) and screech tones (Raman 1999). The latter two exist only in supersonic jets, while mixing noise is emitted in both the subsonic and supersonic regimes. Despite considerable progress in characterising and reducing jet noise, our understanding of jet noise generation remains incomplete for two related reasons: first, the physical sources of noise have not been identified unambiguously and modelled adequately, and second, the precise physical processes of sound generation have not all been described satisfactorily, both hindering accurate predictions. Further investigations of these two aspects are not only of fundamental scientific interest, but are also of technological relevance for effective reduction of noise, which is a pressing task given the continued expansion of the aviation industry and introduction of more stringent limits on the noise level.

In the mainstream approach of acoustic analogy, the compressible Navier–Stokes (N–S) equations are rearranged into a form such that linear wave-like operators appear on the left-hand side and the corresponding inhomogeneous terms are then interpreted as the 'apparent sources'. Different rearrangements of the N–S equations and combinations of the dependent variables (including nonlinear combinations) lead to a variety of analogies (Lighthill 1952; Phillips 1960; Lilley 1974; Goldstein 2001). The apparent source is therefore not unique. A generalised acoustic analogy was developed, which decomposes the total flow into a 'base flow' and 'residual components', with the former being allowed to be non-parallel in general, and the N–S equations being arranged such that only quadratic terms of the residual components, or the fluctuating stress tensor, appear as the apparent source (Goldstein 2003). This approach accounts for the interactions between the sound and the mean (base) flow, as does the Lilley–Goldstein analogy (Lilley 1974; Goldstein 2001), but it has the significant advantage that it allows two long-standing issues to be resolved: namely, the controversy over whether or not to include the instability modes (i.e. the causal versus bounded solutions) is settled (Goldstein & Leib 2005), and the critical-layer singularity can be removed (Goldstein & Leib 2008;

https://doi.org/10.1017/jfm.2022.252 Published online by Cambridge University Press

Goldstein, Sescu & Afsar 2012), both through the inclusion of non-parallelism. The apparent source of the quadratic form only is also more amendable to modelling than that of mixed linear and quadratic type. The far-field pressure spectrum can be expressed in terms of the two-point time-delayed correlation of the stress tensor, a statistical property that may be supplied using computational data for the near field of the flow. Applications of this generalised analogy indeed led to improved predictions of jet noise (Goldstein 2011; Afsar, Sescu & Leib 2019*a*; Afsar, Sescu & Sassanis 2019*b*). However, the acoustic analogy type of approach does not provide an unambiguous identification of the physical sources, as remarked by Goldstein (2003). By its very nature, it does not actually describe the true physical process of acoustic radiation, which involves near-field fluctuations changing their nature to acquire the character of sound waves in the far field.

Identification of the physical sources of noise is rather difficult because the great majority of unsteady fluctuations in the near field do not radiate sound, and specifically the most energetic ones are not necessarily the primary emitters. Goldstein (2005) proposed an approach of identifying the true source of an unbounded turbulent flow, in which suitable space–time filtering is introduced to define a nearly non-radiating but unsteady 'base flow', while the supposedly much smaller residual radiating components then satisfy the Euler equations linearised about the base state. The source terms in these equations are contributed primarily by the base flow and so may be considered as the true source. Sinayoko, Agarwal & Hu (2011) implemented filtering of this kind approximately (under the homentropic-flow assumption) to direct numerical simulations (DNS) data, and showed that it can separate the flow into radiating and non-radiating components, and that the 'true sources' are much different from, and several orders of magnitude smaller than, the usual apparent sources. However, the 'true sources' have not been used to (re)calculate the sound waves. This procedure is rather hard to implement in practice.

It is generally recognised that mixing is caused by vortical structures of large and small scales, which exhibit different features in evolution and radiation. In particular, in turbulent shear flows including circular jets, there exist large-scale organised motions that exhibit a high degree of spatial–temporal order. These motions are referred to as CS, a common type of which is 'roller' structures of spanwise vortices, such as 'Brown–Roshko rollers' in free shear layers (Roshko 1976). Similar roller structures on circular jets have been observed in experiments (Michalke & Freymuth 1966; Beavers & Wilson 1970; Peterson & Hama 1978; Zaman & Hussain 1980; Paschereit *et al.* 1992) and revealed by DNS (Grinstein, Oran & Boris 1987). Such CS on mixing layers and circular jets can be represented by Kelvin–Helmholtz (K–H) instability waves or wavepackets supported by the time-averaged mean flow (Crow & Champagne 1971; Liu 1974; Gaster, Kit & Wygnanski 1985; Suzuki & Colonius 2006), and their nonlinear development has been described by a nonlinear parabolised stability equation (PSE) approach (Cheung & Lele 2009) or nonlinear critical-layer theory (Wu & Zhuang 2016); see also Liu (1989) and references therein for earlier modelling efforts. Global resolvent analysis and bi-global stability analysis, both of which account for fully streamwise non-parallelism but are entirely linear, have also been carried out. The resulting solutions, the resolvent modes (Nicholas & Lele 2011; Schmidt *et al.* 2017) and damped global modes (Garnaud *et al.* 2013; Jeun, Nichols & Jovanović 2016), contain significant signatures of local K–H instability modes, which are of key interest; for reviews of these topics, the reader is referred to Jordan & Colonius (2013), Wu & Zhuang (2016), Cavalieri, Jordan & Lesshafft (2019) and [I]. CS not only contribute to the Reynolds stresses, drags and heat fluxes, but also control entrainment and mixing, and furthermore are a dominant source of mixing

https://doi.org/10.1017/jfm.2022.252 Published online by Cambridge University Press

noise (Crow & Champagne 1971; Bechert & Pfizenmaier 1975, 1977; Moore 1977; Hussain & Hasan 1985; Cavalieri *et al.* 2013; Suzuki 2013).

Based on extensive experimental data, Tam, Golebiowski & Seiner (1996) proposed a phenomenological two-source model, according to which jet noise consists of contributions from large-scale CS and fine-scale turbulence, and the spectrum of each obeys a fairly universal similarity relation, which was shown to be valid in a wide range of operation conditions, including hot jets (Viswanathan 2004; Tam 2019). Sound waves radiated by large-scale CS concentrate primarily in the conical region that makes relatively small angles to the downstream axial direction, while fine-scale turbulence emits noise that is more or less omnidirectional. Interestingly, the peak frequencies of the respective spectra are of the same order despite the fact that fine-scale turbulence occupies a higher frequency band. Narayanan, Barber & Polak (2002) pointed out that low-frequency sound sources are generally located in the downstream region, whilst those of high-frequency noise are close to the exhaust nozzle. The fluctuations in the near nozzle region and their role as noise source were investigated by Fontaine *et al.* (2015), Brès *et al.* (2018) and Bogey & Sabatini (2019). By combining experiments or large-eddy simulations (LES) with linear stability analysis, it was demonstrated that energetic fluctuations are in the frequency band of the inviscid K–H instability of the mean flow. These fluctuations presumably emit high-frequency sound waves directly through the Mach-wave radiation mechanism (see below). However, the dominant far-field noise concentrates in a much lower band, with its peak frequency being just about $1/10$ of the frequency of the most unstable mode. Nozzle exit conditions are known to influence the radiation. Fontaine *et al.* (2015) studied the effect of the thickness of turbulent nozzle boundary layer, and found that the radiated high-frequency sound in directions close to the jet axis scales on the momentum thickness for different nozzle sizes and exhaust conditions. Brès *et al.* (2018) and Bogey & Sabatini (2019) investigated how the nozzle-exit boundary-layer state – laminar, turbulent or transitional – influences the radiation, and observed that an initially laminar state results in louder high-frequency noise. The far-field acoustic energy was found to be carried by just a few modes with small azimuthal wavenumbers, of which the axisymmetric mode is dominant at the peak radiation angle and frequency.

As an effort to identify dominant sources of noise, much attention has also been given to possible causal relations between sound emission and spatial–temporal behaviours in the flow field. Strong emission has been observed to be associated with intermittent events, which may manifest as signal jittering (Juvé, Sunyach & Comte-Bellot 1980; Hileman *et al.* 2005; Cavalieri *et al.* 2010; Kearney-Fischer, Sinha & Samimy 2013) or spatial–temporal modulation of wavepackets (Crow & Champagne 1971). LES have been performed at fairly high Reynolds numbers to provide information about how the far-field noise correlates with near-field fluctuations either statistically (Bogey, Bailly & Juvé 2003; Bogey & Bailly 2007) or in the time–space domain (Cavalieri *et al.* 2011*b*; Brès *et al.* 2016), and the results confirm the importance of intermittency. Vortex pairing had long been considered as a major sound emission event (e.g. Kibens 1980), but this was later found to be the case only at low Reynolds numbers (Bridges & Hussain 1987, 1992). At high Reynolds numbers of practical interest, noise is generated primarily due to dynamic interactions and breakdown of CS (Bridges & Hussain 1987, 1992; Crawley *et al.* 2018). These findings suggest that nonlinear dynamics of CS must be considered.

A number of theoretical investigations have sought to elucidate the role of CS in noise generation. Taking the viewpoint that instability modes or wavepackets constitute a main source of mixing noise (Crow & Champagne 1971; Liu 1974), Ffowcs Williams & Kempton (1978) modelled the source terms in Lighthill's analogy in terms of a wavepacket

https://doi.org/10.1017/jfm.2022.252 Published online by Cambridge University Press

and then calculated the radiated sound wave. Sandham & Salgado (2008) and Wan *et al.* (2016) employed the linear PSE approach to predict the development of the axisymmetric (ring) and azimuthal modes with different frequencies, and the resulting near-field solution was used subsequently to evaluate the apparent source, which is of quadratic form, in the Lilley–Goldstein acoustic analogy. The results indicate that the far-field sound is predominantly axisymmetric and is contributed primarily by the difference frequency component generated by the quadratic interaction in the source. Cheung & Lele (2009) used the nonlinear PSE approach to predict the evolution and interaction of instability modes on a compressible mixing layer, and the acoustic far field is computed using the Lilley–Goldstein analogy. They concluded that acoustic radiation of nonlinearly evolving and interacting modes is enhanced in comparison with their linear counterparts. The effects of jittering or intermittency on radiation were assessed in the framework of acoustic analogy, with the jittering being introduced, on the phenomenological basis, to the phase and/or amplitude of the wavepacket representing CS in physical space (Ffowcs Williams & Kempton 1978; Cavalieri *et al.* 2010) or to the statistical measure of the source (Goldstein 1984; Cavalieri & Agarwal 2014). Jittering is found to cause stronger emission. Concurrently with these modelling efforts, extensive computational studies have been carried out. DNS of jet noise, which are restricted to very low Reynolds numbers, have identified clear wave-like signatures of CS in the near field of a turbulent jet (Freund 2001). Suponitsky, Sandham & Morfey (2010) simulated sound generation due to nonlinear interactions of CS as modelled by instability modes, while Baqui *et al.* (2015) used linearised Euler equations to calculate the sound wave generated by a modulated instability mode. On the other hand, the LES calculations of Fu *et al.* (2017) indicate that the radiation is weakened when coherent components are removed artificially.

While the studies mentioned above have provided useful data and insights, neither acoustic analogy nor pure numerical methodology probes into the true physical process of acoustic radiation. For broadband turbulence, the fundamental questions of what constitute physical sources and how they emit sound waves remain unsolved, and there is no first-principle approach or resolution on the horizon (Viswanathan 2010; Tam 2019). Progress has been made in developing first-principle theories for acoustic radiation of unstable wavepackets on laminar shear flows, and of CS on turbulent flows as well, with CS being treated as instability wavepackets; a review was recently published by Wu & Zhang (2019). The theoretical development in this direction was based on the asymptotic approach, first introduced by Crow (1970). Application of this methodology to supersonic shear flows has led to a first-principle description of Mach-wave radiation: unstable modes or CS, which propagate supersonically relative to the ambient fluid, emit directly highly directional sound waves (Tam & Burton 1984; Wu 2005), which can be expressed explicitly in terms of the unstable-wave/CS (Wu 2005). Alternatively, the Kirchhoff surface propagation technique was also used to extrapolate the near-field pressure to the far field, thereby predicting the sound field (Sinha *et al.* 2014).

In subsonic shear flows, the mechanism of acoustic radiation is rather more complex because instability modes propagate subsonically and so do not radiate any sound directly. However, when the spatial growth and decay of a mode are taken into account, the tail of its envelope spectrum contains small supersonic components, one of which radiates to the far field a sound wave with the same frequency as that of the instability mode, as was first shown by Tam & Morris (1980). Strictly speaking, the amplitude of the sound wave is exponentially small with respect to the ratio of the acoustic wavelength to the length scale of the envelope (Wu & Huerre 2009; Zhang & Wu 2020), but in practice it turns out to be significant in small angles to the downstream axial direction. The directivity

https://doi.org/10.1017/jfm.2022.252 Published online by Cambridge University Press

exhibits an exponential dependence on the cosine of the polar angle, a feature referred to as 'superdirectivity' (Crighton & Huerre 1990). Recently, one-way linear Euler (N–S) equations, which retain the non-parallel flow effect at leading order, were proposed, and this approach predicts simultaneously the linear development of CS and the acoustic field radiated due to non-parallelism induced modulation (Towne & Colonius 2015). The efficiency of radiation increases in the presence of jittering or strong modulation (Cavalieri *et al.* 2011*a*; Baqui *et al.* 2015), and hence is likely to be a viable noise-generating mechanism in subsonic jets as well (Tam *et al.* 2008; Tam 2019). This conclusion and the acoustic field expected by this mechanism are confirmed by experiments (Cavalieri *et al.* 2012).

In addition to Mach-wave radiation, which is a linear mechanism, a different and nonlinear mechanism appears to operate to emit noise with frequencies much lower than those of the instability modes. This was suggested by the experimental finding that when a jet is excited by two modes with different frequencies, strong sound is radiated at the difference frequency, generated by the nonlinear interaction of the two modes (Ronneberger & Ackermann 1979). A nonlinear radiation mechanism is also suggested by the noticeable feature that the dominant far-field noise concentrates in a spectral band with its peak-radiation frequency being just about $1/10$ of the frequency of the most unstable mode in the near nozzle region (Fontaine *et al.* 2015; Brès *et al.* 2018) and the spectral peak of hydrodynamics fluctuations within the entire jet flow. In the case of a laminar circular jet, this scenario of sound generation was studied by Sandham & Salgado (2008) using the Lilley–Goldstein analogy combined with the linear PSE approach, and by Suponitsky *et al.* (2010) using DNS. A first-principle asymptotic theory was presented by Wu & Huerre (2009), who showed that the nonlinear interaction between a pair of helical modes produces an azimuthally dependent mean-flow distortion (streaky flow), which emits low-frequency sound waves with the length and time scales comparable with those of the modal envelope. The nonlinear evolution and acoustic radiation of a two-dimensional wavepacket representing CS on a subsonic turbulent mixing layer were considered in [I]. By examining the far-field asymptote of the hydrodynamic fluctuations, the physical sound source is identified to be the breathing mean-flow distortion, generated by the nonlinear interactions of the CS or instability wavepacket. The mathematical equivalent sound source was derived. However, it cannot be predetermined completely before the sound field is calculated, indicating that the radiated sound waves act back on their source. Interestingly and counter-intuitively, the radiations to the upper and lower half-planes influence each other.

As was mentioned above, describing the nonlinear evolution of CS is an integrated part of analysing and predicting the radiation process. The mathematical theory for CS dynamics was developed by adopting the triple decomposition, which splits the instantaneous flow into the (Favre) time-averaged mean field, the large-scale quasi-periodic coherent part and small-scale random fluctuations. Among these, the coherent motion is treated as instability waves/wavepackets on the mean flow.

Experimental and theoretical studies indicate that CS are well represented by linear stability modes of the mean-flow profile, but significant deviation arises where their growth is diminished. Since the CS have acquired a significant amplitude there, the evolution enters a nonlinear stage (Paschereit, Wygnanski & Fiedler 1995; Cavalieri *et al.* 2013). A strongly nonlinear non-equilibrium critical-layer theory was developed by Wu & Zhuang (2016) to describe the nonlinear development of CS on an incompressible turbulent mixing layer. This work was extended in [I] to CS on a compressible but subsonic mixing layer. This theory can capture roll-up and amplitude saturation, including spatial–temporal modulation of CS.

https://doi.org/10.1017/jfm.2022.252 Published online by Cambridge University Press

The objective of the present paper is to present an asymptotic theory that describes the nonlinear development of CS on a subsonic circular jet and the physical process of such CS generating low-frequency noise. As the axial velocity profile of a circular jet has a generalised inflection point, there exist several unstable modes distinguished by their azimuthal wavenumbers $m \in \mathbb{Z}$, including the ring mode ($m = 0$) and helical modes ($m \neq 0$), which are similar to the two-dimensional and oblique modes in a planar flow, respectively. A laminar jet or a time-averaged turbulent jet can be divided into two regions in the axial direction: the near-nozzle region with an obvious potential core and the developed region. The hydrodynamics and the characteristics of radiation in these two regions are quite different, due to the fact that in the near-nozzle region, a thin shear layer develops from the nozzle lip, and its thickness δ^* is much smaller than its central position R_0^*, i.e. $\delta^*/R_0^* \ll 1$, whereas in the developed region, $\delta^*/R_0* = O(1)$ (Michalke 1965; Michalke & Fuchs 1975; Zaman & Hussain 1981). As R_0^* varies slowly compared with the fast growth of δ^*, it remains comparable with D^*, the exhaust nozzle diameter.

This paper will focus on nonlinear modulation and acoustic radiation of ring-mode CS in the well-developed region. The critical-layer dynamics turns out to be strong nonlinear, quite similar to that of two-dimensional subsonic CS on a planar shear layer considered in [I]. A unified theory for subsonic and incompressible ring-mode CS can be developed to capture the nonlinear phenomena observed in experiments, such as nonlinear saturation (Cohen & Wygnanski 1987; Corke, Shakib & Nagib 1991; Raman, Rice & Reshotko 1994; Paschereit *et al.* 1995; Samimy *et al.* 2007) and roll-up (Beavers & Wilson 1970; Paschereit *et al.* 1992).

The rest of the paper is organised as follows. In § 2, after separating CS from the instantaneous flow field via Favre phase averaging, we specify the asymptotic scalings pertinent to the nonlinear evolution and acoustic radiation of ring-mode CS. Three decks or layers, distinguished by their radial thicknesses, are analysed. The evolution–modulation system for the ring-mode CS is obtained by matching the solutions in the main shear flow and the critical layer. The acoustic field is determined by matching with the solution in the main shear flow. In § 3, the systems describing the evolution–modulation and radiation of the CS are converted to the frequency–wavenumber space and solved, and the parameters measuring the non-parallel mean-flow profile are defined. In § 4, we present the numerical calculations and results, which include the spatial–temporal dynamics of CS and their acoustic radiation characteristics. Finally, conclusions and discussions are given in § 5.

2. Formulation

2.1. *Flow decomposition and asymptotic scalings*

We consider ring-mode CS on a compressible axisymmetric circular jet, produced by an exhaust mean-flow velocity U_I^* and a coflow U_O^* with $U_I^* > U_O^*$, separated by a circular nozzle. The temperatures in these two streams are T_I^* and T_O^*, respectively. The flow is to be described using cylindrical coordinates (x, r, θ), with the corresponding velocity being denoted by $\boldsymbol{u} = (u, v, w)$. The axial and radial coordinates, x^* and r^*, and time t^* are non-dimensionalised by δ_0^* and δ_0^*/U_0^*, respectively, where the superscript * signifies a dimensional quantity, δ_0^* denotes the shear-layer thickness at a typical axial position, and U_0^* is a reference velocity. The velocity U^*, density ρ^*, temperature T^* and viscosity μ^* are normalised by

$$U_0^* = (U_I^* - U_O^*)/2, \quad \rho_0^* = \rho_I^*, \quad T_0^* = T_I^*, \quad \mu_0^* = \mu_I^*, \tag{2.1a–d}$$

https://doi.org/10.1017/jfm.2022.252 Published online by Cambridge University Press

respectively, while the non-dimensional pressure p is introduced by writing

$$p^* = p_0^* + \rho_0^* U_0^{*2} p. \tag{2.2}$$

The resulting dimensionless parameters, including the Mach number Ma, the Reynolds number Re and the Prandtl number Pr, are defined as

$$Ma = U_0^*/\sqrt{\gamma R_g^* T_0^*}, \quad Re = \rho_0^* U_0^* \delta_0^*/\mu_0^*, \quad Pr = \mu_0^* C_p^*/k_0^*, \tag{2.3a–c}$$

where R_g^* is the universal gas constant, k_0^* is thermal conductivity, and $\gamma = C_p/C_v$ with C_p and C_v being the constant-pressure and constant-volume specific heat capacities, respectively. The Mach number of the exhaust flow, Ma_I, is for convenience defined as

$$Ma_I = \frac{2U_I^*}{U_I^* - U_O^*} Ma \overset{\text{def.}}{=\!=} \bar{U}_{-} Ma. \tag{2.4}$$

As in the planar cases (Wu & Zhuang 2016; [I]), we adopt the triple decomposition (Hussain & Reynolds 1972)

$$(\boldsymbol{u}, T, p, \rho) = (\bar{\boldsymbol{U}}, \bar{T}, \bar{P}, \bar{\rho}) + (\tilde{\boldsymbol{u}}, \tilde{T}, \tilde{p}, \tilde{\rho}) + (\boldsymbol{u}', T', p', \rho'); \tag{2.5}$$

that is, the instantaneous field $(\boldsymbol{u}, T, p, \rho)$ is composed of the mean flow $(\bar{\boldsymbol{U}}, \bar{T}, \bar{P}, \bar{\rho})$, the quasi-periodic coherent motion $(\tilde{\boldsymbol{u}}, \tilde{T}, \tilde{p}, \tilde{\rho})$, and small-scale turbulence $(\boldsymbol{u}', T', p', \rho')$. The CS signature $\tilde{f}$ is obtained by $\tilde{f} \equiv \langle f \rangle - \bar{f}$, where the angle braces denote the (Favre) phase-averaging, and the over-bar indicates (Favre) time-averaging; see [I] for details.

The governing equations, together with the closure models for the time-averaged Reynolds stresses $\bar{\tau}_{ij}$ and the coherent Reynolds stresses $\tilde{\tau}_{ij}$, are the same as those in [I] once the operator $\partial_y \bullet$ is replaced by $r^{-1}\partial_r(r\bullet)$. Definitions for the parameters, such as Pr_T, $\widetilde{Pr}_T$, R_T, $\tilde{R}_T$, $\tilde{\mu}_t$, could be also found in (2.19)–(2.22) and (2.30)–(2.33) of [I]. There are also the time delays $\hat{\tau}_1$ and $\hat{\tau}_2$, introduced in the closure models, between the coherent Reynolds stresses and the strain rates of CS.

The turbulent Reynolds and Prandtl numbers, R_T and $Pr_T = O(1)$, are introduced in the Reynolds-stress model for $\overline{u_i' u_j'}$, while the coherent Reynolds and Prandtl numbers, $\tilde{R}_T$ and $\widetilde{Pr}_T = O(1)$, arise through the coherent-Reynolds-stress model for $\langle u_i' u_j' \rangle - \overline{u_i' u_j'}$. It is assumed that $Re \gg R_T \gg 1$, which is reasonable since the eddy viscosities are much greater than the molecular viscosity (Wu & Zhuang 2016; [I]). The axial development of the mean flow is described by the slow variable

$$\tilde{x} = x/R_T. \tag{2.6}$$

The radial velocity scales as $R_T^{-1}\bar{V}$, with $\bar{V} = O(1)$, and the mean flow can be written as $(\bar{U}(\tilde{x}, r), R_T^{-1}\bar{V}(\tilde{x}, r), \bar{T}(\tilde{x}, r), \bar{P}, \bar{\rho}(\tilde{x}, r))$. In this paper, we consider the full developed region of the jet, where the shear-layer thickness is comparable with the nozzle diameter D^*, i.e. $\delta_0^* = O(D^*)$, and the shear flow occupies the radial region where $r = O(1)$.

The dynamics of a ring-mode CS is similar to that of a two-dimensional instability mode considered in [I]. The region where the mode is nearly neutral is of special importance because the CS has acquired its maximum magnitude there and thus is prone to nonlinear effects in the critical layer (Wu 2019). On a subsonic jet, the mean-flow temperature profile usually has a moderate radial gradient. By treating this gradient as a small quantity such that the major nonlinearity is associated with both the simple-pole singularity of

https://doi.org/10.1017/jfm.2022.252 Published online by Cambridge University Press

the temperature disturbance and the logarithm singularity of the second term in the outer expansion of the axial velocity, the resulting critical-layer dynamics is strongly nonlinear, as explained in Sparks & Wu (2008) and [I], and furthermore weakly nonlinear dynamics can be recovered as a limiting case. Let $\tilde{q}$ represent any of the velocity, temperature, pressure and density of the CS. Then in the main part of the flow, a ring-mode CS can, at leading order, be represented by a modulated travelling wave

$$\tilde{q} = \epsilon A^{\dagger}(\tau, \bar{x})\, \hat{q}(r)\, \mathrm{e}^{\mathrm{i}\alpha\zeta} + \text{c.c.}, \tag{2.7}$$

where $\zeta = x - ct$, with $\alpha = O(1)$, and $c = O(1)$ are the wavenumber and phase speed of the locally neutral mode, respectively, $\epsilon \ll 1$ is a measure of its magnitude, and $\hat{q}(r)$ characterises its radial distribution; the spatial–temporal modulation is described by the amplitude function $A^{\dagger}$ of the slow temporal and spatial variables τ and $\bar{x}$, defined as

$$\tau = \epsilon^{1/2} t, \quad \bar{x} = \epsilon^{1/2} c^{-1}(x - R_T \tilde{x}_N), \tag{2.8a,b}$$

for modulation taking place in the non-equilibrium nonlinear critical layer, where $\tilde{x}_N$ denotes the axial position where the mode becomes neutral. CS of such a wavepacket form consist of sideband spectral components adjacent to the fundamental wave, which are encapsulated in the envelope $A^{\dagger}$. The spatial–temporal modulation of the latter is crucial in the acoustic radiation, as will become clear later. With a narrow-band spectrum (centred at the frequency of the locally neutral mode), this wavepacket model represents of course only large-scale CS. A wavepacket will typically be taken to be a superposition of time-periodic disturbances (see § 3.2) and is in general quasi-periodic. Such a wavepacket represents fairly well CS generated by harmonic excitation. In an unforced jet, CS are excited by stochastic disturbances in the turbulent boundary layer on the nozzle wall and can also be educed (Zaman & Hussain 1984), and the dominant CS, whose frequencies are close to that of the preferred mode, may also be represented by wavepackets, albeit with a somewhat broader sideband.

In order to include viscosity and non-parallelism along with nonlinear and non-equilibrium effects at the leading order in the dynamical system, the parameters Re, $\tilde{R}_T$ and R_T are scaled as (Wu & Zhuang 2016; [I])

$$Re^{-1} = \bar{\lambda}\epsilon^{3/2}, \quad \tilde{R}_T^{-1} = \tilde{\lambda}\epsilon^{3/2}, \quad R_T^{-1} = \sigma\epsilon/c, \tag{2.9a–c}$$

where $\bar{\lambda}, \tilde{\lambda} = O(1)$ are Haberman (1972) parameters, and $\sigma = O(1)$. It follows from (2.6) and (2.8*a*,*b*) that $\tilde{x}$ and $\bar{x}$ are related via $\tilde{x} = \tilde{x}_N + \epsilon^{1/2}\sigma\bar{x}$.

The self-interaction of CS of strongly nonlinear nature takes place in the critical layer centred at r_c, where $\bar{U}(r_c) = c$. For a subsonic mode, the critical level r_c is located at the generalised inflection point, where $(\partial/\partial r)\bar{\rho}(\partial\bar{U}/(r\,\partial r)) = 0$. The dominant nonlinearity, driven by $\tilde{v}\partial_r\bullet$ according to scaling analysis, is required to balance the non-equilibrium effect, which suggests the appropriate transverse variable

$$Y = (r - r_c)/\epsilon^{1/2}. \tag{2.10}$$

It is worth pointing out that in the developed region of the jet, $r_c = O(1)$. In the near-nozzle region, the jet consists of a potential core and a thin shear layer developing along the lip line, so $\delta_0^* \ll D^*$ while the critical level is located at $r^* \approx D^*/2$. It follows that $r_c \gg 1$. The size of r_c^{-1} thus characterises different axial regions as δ_0^*/D^* does.

https://doi.org/10.1017/jfm.2022.252 Published online by Cambridge University Press

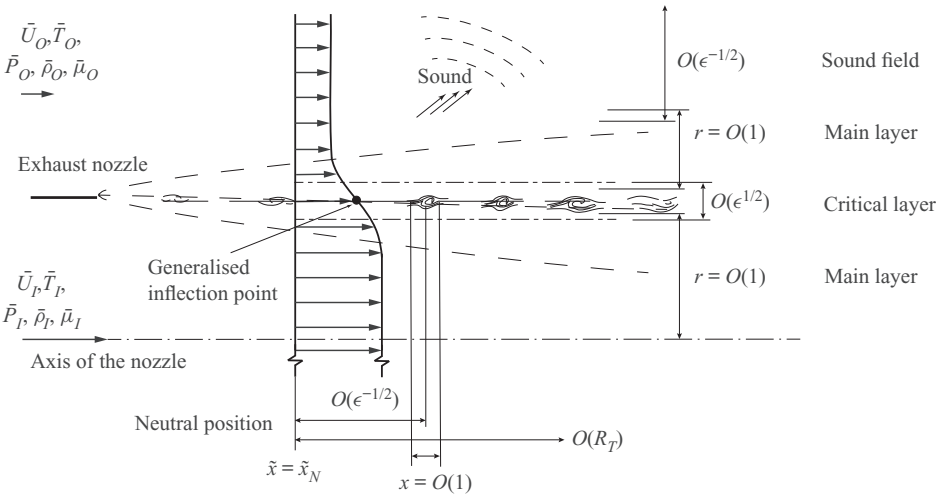


Figure 1. Asymptotic structure of, and the scalings in, the axial and radial directions.

As will be shown, while the physical acoustic source is located in the main flow and the critical layer, the fluctuations acquire the character of sound waves in an outer acoustic region. Its radial extent is comparable with the axial length scale of the wavepacket envelope, so we introduce the acoustic transverse variable

$$\bar{r} = \epsilon^{1/2} c^{-1} r. \tag{2.11}$$

The overall asymptotic structure of the flow and the relevant asymptotic scalings are illustrated in figure 1. The three layers in the radial direction will be analysed in order to derive the nonlinear evolution system of the CS, and to determine the emitted sound waves. The ensuing analysis may appear rather complex, but the major steps and outcomes can be understood without going through all the details, and they are highlighted as follows. The main jet flow is considered first in § 2.2. The fundamental component of the CS appears at leading order as a nearly neutral instability mode governed by an eigenvalue problem. At the next order, an inhomogeneous Rayleigh equation arises, and its solvability condition leads to an 'embryo amplitude equation' (2.28), which contains a jump. The unsteady mean-flow distortion, induced by interactions in the main flow as well as in the critical layer, is analysed in § 2.3. The key outcome is (2.36), in which the forcing terms represent the physical sources in the main shear flow. The solution, given by (2.38), allows for a jump across the critical layer. The latter is considered in § 2.4 to derive the equations for the temperature and vorticity disturbance, (2.47) and (2.48), and the jump in the fundamental component is deduced and combined with (2.28) to obtain the amplitude equation (2.51). The resulting closed system, (2.47)–(2.48) with (2.51), governs the nonlinear development of the CS. Further analysis at a higher order determines the jump in the mean-flow distortion, (2.56), which is contributed by nonlinear interactions in the critical layer and represents another physical source of sound. The radial velocity decays in inverse proportion to the radial distance, indicating that the breathing mean flow acts an emitter with an equivalent source (2.57), which can be expressed in terms of the physical sources.

https://doi.org/10.1017/jfm.2022.252 Published online by Cambridge University Press

2.2. *Disturbances in main shear flow and their far-field asymptote*

Let $\tilde{q}$ represent any of $\tilde{u}$, $\tilde{v}$, $\tilde{T}$, $\tilde{p}$ and $\tilde{\rho}$, which are all quantities to describe the CS. In the main part of the jet, $\tilde{q}$ is expanded as an asymptotic series

$$\tilde{q}(\tau,\bar{x},r,\zeta,\theta)=\epsilon A^{\dagger}(\tau,\bar{x})\,\hat{q}_0(r)\,\mathrm{e}^{\mathrm{i}\alpha\zeta}+\epsilon^{3/2}\sum_{n=1}^{\infty}\hat{q}_1^{\langle n\rangle}(\tau,\bar{x},r)\,\mathrm{e}^{\mathrm{i}n\alpha\zeta}+\text{c.c.}+\cdots+\tilde{q}_M, \tag{2.12}$$

where $\tilde{q}_M$ stands for the slowly modulated mean-flow distortion, generated by nonlinear interactions of CS; it will be analysed in § 2.3. Inserting (2.12) into the CS equations (see [I]) at $O(\epsilon)$, we obtain the eigenvalue problem consisting of the homogeneous compressible Rayleigh equation for pressure $\hat{p}_0$ and the boundary condition

$$\mathcal{L}_R^{\langle 1\rangle}\hat{p}_0=0,\quad \hat{p}_0 \text{ is finite as } r\to 0,\quad \hat{p}_0\to 0 \text{ as } r\to\infty, \tag{2.13}$$

where the Rayleigh operator is defined in cylindrical polar coordinates as

$$\mathcal{L}_R^{\langle n\rangle}\equiv\frac{\partial^2}{\partial r^2}+\left(\frac{1}{r}+\frac{\bar{T}'}{\bar{T}}-\frac{2\bar{U}'}{\bar{U}-c}\right)\frac{\partial}{\partial r}+(n\alpha)^2\left[\frac{Ma^2(\bar{U}-c)^2}{\bar{T}}-1\right], \tag{2.14}$$

with the prime here denoting differentiation with respect to r. The eigenvalue problem (2.13) determines the wavenumber α. As usual, non-parallelism is negligible when considering eigenfunction in the main part of the jet, but will appear at leading order in the critical layer, and moreover control the modulation.

The solution to (2.13) behaves as

$$\hat{p}_0\to\frac{\mathscr{P}_{0,\infty}}{\sqrt{r}}\exp\left[-\alpha r\sqrt{1-Ma^2(\bar{U}_+-c)^2/\bar{T}_+}\right]\quad \text{as } r\to\infty, \tag{2.15}$$

where $\mathscr{P}_{0,\infty}$ is a constant, and $\bar{U}_+=2U_O^*/(U_I^*-U_O^*)$ and $\bar{T}_+=\beta_T=T_O^*/T_I^*$ are the mean-flow streamwise velocity and temperature of the coflow. When $r\to 0$, $\hat{p}_0$ must satisfy the regularity requirement in the form of a zero-order Bessel function, namely,

$$\hat{p}_0\to\mathscr{P}_{0,0}\left\{1+[1-Ma^2(\bar{U}_a-c)^2/\bar{T}_a]\frac{\alpha^2}{4}\,r^2+\cdots\right\}\quad \text{as } r\to 0, \tag{2.16}$$

where $\mathscr{P}_{0,0}$ is another constant, which is, together with $\mathscr{P}_{0,\infty}$, determined by solving (2.13) globally; $\bar{U}_a$ and $\bar{T}_a$ stand, respectively, for the mean-flow axial velocity and temperature on the axis.

A ring-mode CS is an inviscid instability mode associated with the generalised inflection point, where

$$\iota_0=\bar{T}_c'/\bar{T}_c-\bar{U}_c''/\bar{U}_c'+1/r_c=0; \tag{2.17}$$

here, the subscript 'c' denotes the value at the critical level r_c, or at $y\equiv r-r_c=0$. Near the critical level, the asymptotic solution to (2.13) for $\hat{p}_0$ (cf. Wu 2005) is found as

$$\hat{p}_0=\frac{\bar{U}_c'}{\bar{T}_c}\left[\pi_1(\alpha;y)+\frac{\alpha^2}{3}\left(b_1+\frac{\bar{U}_c''}{\bar{U}_c'}\right)\pi_2(\alpha;y)\right], \tag{2.18}$$

https://doi.org/10.1017/jfm.2022.252 Published online by Cambridge University Press

where

$$\left.\begin{gathered}\pi_1(\alpha;y)=1-\tfrac{1}{2}\alpha^2y^2+\tfrac{1}{4}\alpha^2\left(\iota_1-\tfrac{1}{2}\alpha^2\right)y^4+O(y^5),\quad \pi_2(\alpha;y)=y^3+O(y^5),\\ \iota_1=\frac{\bar{T}_c''}{\bar{T}_c}-\frac{2\bar{U}_c'''}{3\bar{U}_c'}-\frac{\bar{T}_c'^2}{\bar{T}_c^2}+\frac{\bar{U}_c''^2}{2\bar{U}_c'^2}-\frac{1}{r_c^2}-\frac{Ma^2\bar{U}_c'^2}{\bar{T}_c}.\end{gathered}\right\}\tag{2.19}$$

At $O(\epsilon^{3/2})$, we obtain the inhomogeneous Rayleigh equation for $\hat{p}_1^{\langle1\rangle}$:

$$\begin{aligned}\mathcal{L}_R^{\langle1\rangle}\hat{p}_1^{\langle1\rangle}(\tau,\bar{x},r)=&-\frac{2\mathrm{i}}{\alpha c}(\mathcal{G}_{11}\hat{p}_0'+\alpha^2\mathcal{G}_{12}\hat{p}_0)\frac{\partial A^\dagger}{\partial\bar{x}}+\frac{2\mathrm{i}}{\alpha}(\mathcal{G}_{21}\hat{p}_0'+\alpha^2\mathcal{G}_{22}\hat{p}_0)\mathcal{D}_0A^\dagger\\&-(\mathcal{G}_{01}\hat{p}_0'+\alpha^2\mathcal{G}_{02}\hat{p}_0)\bar{x}A^\dagger,\end{aligned}\tag{2.20}$$

which is subject to the boundary conditions $\hat{p}_1^{\langle1\rangle}\to\mathscr{P}_1^{\langle1\rangle}(\tau,\bar{x})$ as $r\to0$, and $\hat{p}_1^{\langle1\rangle}\to0$ as $r\to\infty$, where $\mathcal{G}_{ij}$ is given in (3.36) of [I]. Note that $\bar{U}_1$ and $\bar{T}_1$ appear in $\mathcal{G}_{01}$ and $\mathcal{G}_{02}$, and they stand for the derivatives of $\bar{U}$ and $\bar{T}$ with respect to the axial variable $\tilde{x}$ defined in (2.6), namely,

$$(\bar{U}_n,\bar{T}_n)=\sigma^n\left(\frac{\partial^n\bar{U}}{\partial\tilde{x}^n},\frac{\partial^n\bar{T}}{\partial\tilde{x}^n}\right)\bigg|_{\tilde{x}=\tilde{x}_N},\quad n\in\mathbb{N}^+.\tag{2.21}$$

These quantities characterise the variation of the mean-flow profile.

Using the parameter variation technique, we can write the solution for $\hat{p}_1^{\langle1\rangle}$ as

$$\hat{p}_1^{\langle1\rangle}=C_{r1}^{\langle1\rangle}(\tau,\bar{x})\,\hat{p}_0+C_{r2}^{\langle1\rangle\pm}(\tau,\bar{x})\,\hat{p}_{00}-\frac{2\mathrm{i}}{\alpha c}K_{r1}\frac{\partial A^\dagger}{\partial\bar{x}}+\frac{2\mathrm{i}}{\alpha}K_{r2}\mathcal{D}_0A^\dagger-K_{r0}\bar{x}A^\dagger,\tag{2.22}$$

in which

$$\left.\begin{aligned}\hat{p}_{00}(r)&=r_c\hat{p}_0\int_{r_c}^{r}\frac{(\bar{U}-c)^2}{r^\star\bar{T}\hat{p}_0^2}\,\mathrm{d}\hat{r}^\star,\\K_{ri}(r)&=r_c\hat{p}_0\int_0^{r}\frac{(\bar{U}-c)^2}{r^\star\bar{T}\hat{p}_0^2}\tilde{J}_{ri}(r^\star)\,\mathrm{d}r^\star\quad(i=0,1,2),\\\tilde{J}_{ri}(r)&=\frac{1}{r_c}\fint_0^{r}\frac{r^\star\bar{T}}{(\bar{U}-c)^2}(\mathcal{G}_{i1}\hat{p}_0'\hat{p}_0+\alpha^2\mathcal{G}_{i2}\hat{p}_0^2)\mathrm{d}r^\star\quad(i=0,1,2),\end{aligned}\right\}\tag{2.23}$$

with the notation, '$\fint$', denoting the Hadamard finite part if the integration interval contains the critical level r_c.

The boundary conditions for $\hat{p}_1^{\langle1\rangle}$, as was stated before, is satisfied by setting

$$C_{r2}^{\langle1\rangle-}=0,\quad C_{r2}^{\langle1\rangle+}=\frac{2\mathrm{i}}{\alpha c}J_{r1}\frac{\partial A^\dagger}{\partial\bar{x}}-\frac{2\mathrm{i}}{\alpha}J_{r2}\mathcal{D}_0A^\dagger+J_{r0}\bar{x}A^\dagger,\tag{2.24a,b}$$

where we have put

$$J_{ri}=\tilde{J}_{ri}(\infty)=\frac{1}{r_c}\fint_0^{\infty}\frac{r\bar{T}}{(\bar{U}-c)^2}(\mathcal{G}_{i1}\hat{p}_0'\hat{p}_0+\alpha^2\mathcal{G}_{i2}\hat{p}_0^2)\mathrm{d}r\quad(i=0,1,2).\tag{2.25}$$

https://doi.org/10.1017/jfm.2022.252 Published online by Cambridge University Press

Near $y = 0$, the asymptotic solution for $\hat{p}_1^{\langle 1\rangle}$ is found as

$$\hat{p}_1^{\langle 1\rangle} = d_1^{\langle 1\rangle}(\tau,\bar{x})\left[\pi_1(\alpha;y) + \frac{\alpha^2}{3}\,\iota_0 \ln|y|\,\pi_2(\alpha;y)\right] + d_2^{\langle 1\rangle\pm}(\tau,\bar{x})\,\pi_2(\alpha;y)$$
$$+ \frac{\mathrm{i}\alpha}{\bar{T}_c}\left[\left(\frac{\partial}{\partial\tau} + \frac{\partial}{\partial\bar{x}}\right)A^\dagger + \mathrm{i}\alpha\bar{U}_{1,c}\bar{x}A^\dagger\right]\left[y - \left(b_1 + \frac{\bar{U}_c''}{\bar{U}_c'}\right)y^2 + \frac{1}{3}jy^3\ln|y|\right]$$
$$+ \frac{\mathrm{i}\alpha\bar{U}_c'}{c\bar{T}_c}\frac{\partial A^\dagger}{\partial\bar{x}}\,y^2 + \frac{\alpha^2\bar{U}_c'}{3\bar{T}_c}\,j_1\bar{x}A^\dagger y^3\ln|y| + O(y^4\ln|y|), \tag{2.26}$$

where

$$\left.\begin{aligned} j &= \bar{T}_c''/\bar{T}_c - \bar{U}_c'''/\bar{U}_c' - (\bar{T}_c'/\bar{T}_c)^2 + (\bar{U}_c''/\bar{U}_c')^2 - 1/r_c^2,\\ j_1 &= (\bar{T}_c'/\bar{T}_c)(\bar{T}_{1,c}'/\bar{T}_c' - \bar{T}_{1,c}/\bar{T}_c) - (\bar{U}_c''/\bar{U}_c')(\bar{U}_{1,c}''/\bar{U}_c'' - \bar{U}_{1,c}'/\bar{U}_c').\end{aligned}\right\} \tag{2.27}$$

For the inhomogeneous equation (2.20) to admit a solution satisfying the boundary condition, a solvability condition must be introduced as

$$-\frac{3}{\bar{U}_c'}(d_2^{\langle 1\rangle+} - d_2^{\langle 1\rangle-}) = \frac{2\mathrm{i}}{\alpha}J_{r2}\frac{\partial A^\dagger}{\partial\tau} - \frac{2\mathrm{i}}{\alpha}\left(\frac{J_{r1}}{c} - J_{r2}\right)\frac{\partial A^\dagger}{\partial\bar{x}} - J_{r0}\bar{x}A^\dagger. \tag{2.28}$$

This solvability condition can be obtained by multiplying (2.20) by $[r\bar{T}(\bar{U}-c)^{-2}]$, integrating by parts with respect to r from 0 to ∞, and using the asymptote of $\hat{p}_1^{\langle 1\rangle}$ near the critical level. According to Sparks & Wu (2008) and [I], the difference $(d_2^{\langle 1\rangle+} - d_2^{\langle 1\rangle-})$ is related to the jump in the streamwise (axial) velocity $\hat{u}_1^{\langle 1\rangle}$ across the critical layer,

$$\hat{u}_1^{\langle 1\rangle}(y = r_c^+) - \hat{u}_1^{\langle 1\rangle}(y = r_c^-) = -\frac{3\bar{T}_c}{\alpha^2\bar{U}_c'}(d_2^{\langle 1\rangle+} - d_2^{\langle 1\rangle-}), \tag{2.29}$$

which is to be found by matching with the solution within the critical layer.

Harmonics at this order, $\hat{p}_1^{\langle n\rangle}$ $(n \geqslant 2)$, are governed by equations

$$\mathcal{L}_R^{\langle n\rangle}\hat{p}_1^{\langle n\rangle} = 0, \tag{2.30}$$

subject to $\hat{p}_1^{\langle n\rangle} \to \mathscr{P}_1^{\langle n\rangle}(\tau,\bar{x})$ as $r \to 0$ and $\hat{p}_1^{\langle n\rangle} \to 0$ as $r \to \infty$. These equations do not form homogeneous problems since the jump conditions across the critical level, $d_1^{\langle n\rangle+} - d_1^{\langle n\rangle-}$, are not zero in general. When $r \to \infty$, for $n \neq 0$ the pressure of the harmonics behave as

$$\hat{p}_1^{\langle n\rangle} \to \frac{\mathscr{P}_{1,\infty}^{\langle n\rangle}(\tau,\bar{x})}{\sqrt{r}}\exp\left[-n\alpha r\sqrt{1 - Ma^2(\bar{U}_+ - c)^2/\bar{T}_+}\right], \tag{2.31}$$

which is, similar to (2.15), exponentially small for the present subsonic case and also for *subsonic-mode* CS on a supersonic jet. Thus the fundamental ring mode and its harmonics are trapped in the jet, incapable of emitting substantial sound waves directly. They could produce sound waves of exponentially small intensity from the spectral tails of their amplitudes when the spatial modulation of the latter is taken into account (Tam & Morris 1980; Crighton & Huerre 1990).

https://doi.org/10.1017/jfm.2022.252 Published online by Cambridge University Press

2.3. *Analysis of the mean-flow distortion and its role as an emitter*

It is pointed out in [I] that two-dimensional CS on a planar mixing layer radiate sound indirectly by producing a mean-flow distortion that varies slowly in time and in the streamwise direction. Here we will analyse the mean-flow distortion caused by modulated CS on a circular jet to identify the physical sound source as well as to describe the precise physical process of radiation.

The mean-flow distortion caused by the nonlinear interactions is part of the CS and is modulated on the time and length scales of the wave envelope, and thus consists of components whose frequencies and wavenumbers are considerably smaller than those of the fundamental mode. Although a large $O(\epsilon^{3/2})$ mean-flow distortion is generated by the nonlinear interaction of CS in the critical layer, it is trapped within the critical layer. This differs from the case of pairs of helical modes considered by Wu & Huerre (2009). It also indicates an important feature that the primary mean-flow distortion, which contributes to the dominant nonlinear effects on the dynamics of the CS, does not radiate. Instead, sound waves are radiated by less energetic components that are insignificant for the near-field dynamics. The interactions in the main jet and in the critical layer drive a subdominant $O(\epsilon^2)$ mean-flow distortion, the solution for which has the expression

$$\tilde{q}_M = \epsilon^2(u_M, \epsilon^{1/2}v_M, T_M, p_M, \rho_M) + \cdots. \tag{2.32}$$

Substituting (2.12) with (2.32) into the coherent-structure equations, we obtain

$$\begin{cases} \dfrac{1}{c}\dfrac{\partial u_M}{\partial \bar{x}} + \dfrac{\partial v_M}{\partial r} + \dfrac{v_M}{r} + \bar{T}\mathcal{D}_1\rho_M - \dfrac{\bar{T}'}{\bar{T}}v_M = f_c, & (2.33a)\\ \mathcal{D}_1 u_M + \bar{U}'v_M = -\dfrac{\bar{T}}{c}\dfrac{\partial p_M}{\partial \bar{x}} + f_x, & (2.33b)\\ 0 = -\bar{T}\dfrac{\partial p_M}{\partial r} + f_r, & (2.33c)\\ \mathcal{D}_1 T_M + \bar{T}'v_M = (\gamma-1)Ma^2\bar{T}\,\mathcal{D}_1 p_M + f_T, & (2.33d)\\ T_M/\bar{T} + \bar{T}\rho_M = \gamma Ma^2 p_M - f_s, & (2.33e) \end{cases}$$

where the expressions for Reynolds stresses f_c, f_x, f_r, f_T and f_s, which represent the nonlinear forcing in the main jet flow, follow from those in [I] provided that $\partial_y\bullet$ is replaced by $r^{-1}\partial_r(r\bullet)$ in the continuity equation. Here we have

$$f_r = 2|A^\dagger|^2\bar{T}(r\hat{v}_0^2/\bar{T})'/r, \tag{2.34}$$

for which (2.33c) is integrated to give

$$\begin{aligned} p_M(\tau,\bar{x},r) &= 2|A^\dagger|^2(\tau,\bar{x})\left[\frac{\hat{v}_0^2(r)}{\bar{T}(r)} + \int_\infty^r \frac{\hat{v}_0^2(r^\star)}{r^\star\bar{T}(r^\star)}\,\mathrm{d}r^\star\right] \\ &\overset{\text{def.}}{=\!=} 2|A^\dagger|^2(\tau,\bar{x})\left[\frac{\hat{v}_0^2(r)}{\bar{T}(r)} + p_{Mr}(r)\right]. \end{aligned} \tag{2.35}$$

Eliminating ρ_M, u_M and T_M among (2.33a)–(2.33e), we obtain

$$\left(\frac{\partial}{\partial\tau} + \frac{\bar{U}}{c}\frac{\partial}{\partial\bar{x}}\right)\left(\frac{\partial v_M}{\partial r} + \frac{v_M}{r}\right) - \frac{\bar{U}'}{c}\frac{\partial v_M}{\partial\bar{x}} = -\mathcal{S}_R(\tau,\bar{x},r), \tag{2.36}$$

https://doi.org/10.1017/jfm.2022.252 Published online by Cambridge University Press

where $\mathcal{S}_R$ has the same expression as that in the planar case, namely (cf. (5.6) in [I]),

$$\mathcal{S}_R = -\frac{\bar{T}}{c^2}\frac{\partial^2 p_M}{\partial \bar{x}^2} + \frac{1}{c}\frac{\partial f_x}{\partial \bar{x}} - \mathcal{D}_1\left(\bar{T} f_c + \frac{f_T}{\bar{T}}\right) + \mathcal{D}_1^2(Ma^2 p_M - f_s). \tag{2.37}$$

Clearly, (2.36) reduces, as expected, to the planar limit by substituting $r = r_c + y$ with $r_c \gg 1$.

Equation (2.36) can be solved in the frequency–wavenumber space, in which the corresponding quantities are signified by a wide-hat $\widehat{\bullet}$. The solution to (2.36) is found as

$$\widehat{v_M}(\omega, \kappa, r) = \mathrm{i}(\bar{U}\kappa/c - \omega)\left[\frac{r_c}{r}\widehat{a_M^{\pm}}(\omega, \kappa) + \frac{1}{r}\int_{\infty(0)}^{r} \frac{r^\star \hat{\mathcal{S}}_R(\omega, \kappa, r)}{(\bar{U}\kappa/c - \omega)^2}\,\mathrm{d}r^\star\right], \tag{2.38}$$

where $\widehat{a_M^{\pm}}(\omega, \kappa)$ are integration 'constants' whose values are allowed to differ above and below the critical level r_c because there exists a jump across r_c, and also the integration is from ∞ and 0, respectively; a factor r_c also appears in (2.38) to render a form of $\widehat{a_M^{\pm}}(\omega, \kappa)$ similar to that in [I]. It is of interest to write the complementary solution of the inhomogeneous differential equation (2.36) in the physical space as

$$v_{M,c} = \frac{r_c}{r}\left(\frac{\partial}{\partial \tau} + \frac{\bar{U}}{c}\frac{\partial}{\partial \bar{x}}\right) a_M^{\pm}(\tau, \bar{x}). \tag{2.39}$$

Later, a_M^+ will be found to represent the equivalent sound source mathematically, as (2.60) would indicate. Due to the symmetric condition on the axis, $v_M(r = 0) = 0$ has to be satisfied, thus we have $a_M^-(\tau, \bar{x}) \equiv 0$. There exists a jump in $\widehat{v_M}$ across the critical layer; that is, as $r \to r_c^{\pm}$,

$$\widehat{v_M}(r_c^+) - \widehat{v_M}(r_c^-) = \mathrm{i}(\kappa - \omega)(\widehat{a_M^+} - \widehat{a_M^-} + \hat{\mathcal{I}}_R) \tag{2.40}$$

with

$$\hat{\mathcal{I}}_R(\omega, \kappa) = \frac{1}{r_c}\int_0^{\infty} \frac{r\,\hat{\mathcal{S}}_R(\omega, \kappa)}{(\bar{U}\kappa/c - \omega)^2}\,\mathrm{d}r, \tag{2.41}$$

which leads us to find this jump by matching with the critical-layer solution and further to determine $\widehat{a_M^+}$ or a_M^+.

2.4. *Critical-layer analysis and jump conditions*

In order to resolve the singularities of the linear inviscid outer expansions, we now consider the disturbance in the critical layer, which surrounds the the generalised inflection point satisfying (2.17). The analysis is to be performed by introducing the inner variable Y, defined by (2.10). The inner expansion in the critical layer proceeds in the form

$$\tilde{q}(\zeta, \tau, \bar{x}, Y) = \epsilon\,\tilde{q}_0(\zeta, \tau, \bar{x}, Y) + \epsilon^{3/2}\ln\epsilon\,\tilde{q}_{1L}(\zeta, \tau, \bar{x}, Y) + \epsilon^{3/2}\tilde{q}_1(\zeta, \tau, \bar{x}, Y) + \cdots, \tag{2.42}$$

where $\tilde{q}$ also represents the variables of CS, $\tilde{u}$, $\tilde{v}$, $\tilde{T}$, $\tilde{p}$ and $\tilde{\rho}$.

https://doi.org/10.1017/jfm.2022.252 Published online by Cambridge University Press

2.4.1. *Jump in the fundamental and nonlinear evolution equations*

The main purpose of the ensuing analysis in this subsection is to determine the jumps $(d_2^{\langle 1\rangle +} - d_2^{\langle 1\rangle -})$ and $(\widehat{a_M^+} - \widehat{a_M^-})$, which are required in order to predict the nonlinear dynamics and acoustic radiation of the CS.

Compared to planar mixing layers, there is an additional parameter, the ratio of the shear-layer thickness to its central position, which characterises the circularity of the flow. An estimate of the contribution from the nonlinear interaction associated with the temperature field within the critical layer requires $\bar{T}_c'$, the mean temperature gradient of the critical level, to be $O(\epsilon^{1/2})$, as has been explained by Sparks & Wu (2008) and [I], hence we scale this parameter as

$$\bar{T}_c' = \bar{T}_{cM}'\epsilon^{1/2} \quad \text{with } \bar{T}_{cM}' = O(1). \tag{2.43}$$

The reason for this scaling is only to keep the dynamical system strongly nonlinear. In what follows, we will use $\bar{T}_{cM}'$ in the energy equation but $\bar{T}_c'$ in other equations.

Substituting the expansions (2.42) and the mean-flow quantities into the CS equations, we can obtain the expected inner solutions at the first three orders. The steps are quite similar to those in [I], so the detailed derivations are relegated to Appendix A. What should be noted is that the operator ∂_Y in the continuity equation is expressed as

$$\frac{\partial \bullet}{\partial Y} \to \frac{\partial[(r_c + \epsilon^{1/2}Y)\bullet]}{(r_c + \epsilon^{1/2}Y)\partial Y} = \frac{\partial \bullet}{\partial Y} + \epsilon^{1/2}\frac{\bullet}{r_c} - \epsilon\frac{Y\bullet}{r_c^2} + O(\epsilon^{3/2}). \tag{2.44}$$

With this relation, $\tilde{v}_0$, $\tilde{p}_0$, $\tilde{T}_0$, $\tilde{u}_0$, $\tilde{p}_1$ and $\tilde{p}_2$ have the same expressions as those in [I], and others can be found after substituting (2.44) into the continuity equation. After introducing the critical-layer temperature

$$T^\dagger = \tilde{T}_0 - [\bar{T}_c''/\bar{U}_c' + (\gamma - 1)Ma^2\bar{U}_c'](A^\dagger \mathrm{e}^{\mathrm{i}\alpha\zeta} + \mathrm{c.c.}) \tag{2.45}$$

and vorticity

$$Q^\dagger = \frac{\partial \tilde{u}_1}{\partial Y} - \left[\left(\alpha^2 + \frac{Ma^2\bar{U}_c'^2}{\bar{T}_c} - \frac{\bar{T}_c'}{\bar{T}_c}b_1 - j\right)A^\dagger \mathrm{e}^{\mathrm{i}\alpha\zeta} + \mathrm{c.c.}\right], \tag{2.46}$$

we obtain their governing equations,

$$\mathcal{L}_{N,1}^\dagger T^\dagger = \left[\mathrm{i}\alpha\bar{T}_{cM}' - \frac{\bar{T}_c''}{\bar{U}_c'}\mathcal{D}_0 + \frac{\mathrm{i}\alpha}{\bar{U}_c'}\left(\bar{U}_c'\bar{T}_{1,c}' - \bar{U}_{1,c}\bar{T}_c''\right)\bar{x}\right]A^\dagger \mathrm{e}^{\mathrm{i}\alpha\zeta} + \mathrm{c.c.}, \tag{2.47}$$

$$\begin{aligned}\mathcal{L}_{N,2}^\dagger Q^\dagger = {} & -\bar{\lambda}\bar{U}_c'\left(\frac{\mu_c}{Pr} - \bar{T}_c\mu_c'\right)\frac{\partial^2 T^\dagger}{\partial Y^2} - \frac{\tilde{\lambda}\bar{U}_c'\tilde{\mu}_{t,c}}{Pr_T}\frac{\partial^2 T^\dagger(t-\hat{\tau}_1)}{\partial Y^2} \\ & - \frac{\bar{U}_c'}{\bar{T}_c}(\mathrm{i}\alpha A^\dagger \mathrm{e}^{\mathrm{i}\alpha\zeta} + \mathrm{c.c.} - \bar{U}_{1,c}/\bar{U}_c' - \sigma\bar{V}_c/c)\frac{\partial T^\dagger}{\partial Y} \\ & + j\left(\frac{\partial}{\partial\tau} + \frac{\partial}{\partial\bar{x}}\right)A^\dagger \mathrm{e}^{\mathrm{i}\alpha\zeta} + \mathrm{c.c.} + \left(j\bar{U}_{1,c} - \bar{U}_c'j_1\right)\bar{x}(\mathrm{i}\alpha A^\dagger \mathrm{e}^{\mathrm{i}\alpha\zeta} + \mathrm{c.c.}),\end{aligned} \tag{2.48}$$

where the expressions for j and j_1 are given by (2.27), and the operators are defined as

$$\begin{aligned}\mathcal{L}_{N,i}^\dagger \bullet \equiv {} & \left[\frac{\partial}{\partial\tau} + \frac{\partial}{\partial\bar{x}} + (\bar{U}_c'Y + \bar{U}_{1,c}\bar{x})\frac{\partial}{\partial\zeta} - (\mathrm{i}\alpha A^\dagger \mathrm{e}^{\mathrm{i}\alpha\zeta} + \mathrm{c.c.} - c^{-1}\sigma\bar{V}_c)\frac{\partial}{\partial Y}\right]\bullet \\ & - \frac{1}{\alpha^2\bar{U}_c'^2}\left[\bar{\lambda}_i\frac{\partial^2 \bullet}{\partial Y^2} + \tilde{\lambda}_i\frac{\partial^2 \bullet(t-\hat{\tau}_i)}{\partial Y^2}\right] \quad (i = 1, 2),\end{aligned} \tag{2.49}$$

https://doi.org/10.1017/jfm.2022.252 Published online by Cambridge University Press

which are *strongly* nonlinear since the unknown amplitude function $A^\dagger$ appears herein; $\bar{V}_c$ is the scaled radial velocity of the mean flow at the critical level; $\bar{\lambda}_i$ and $\tilde{\lambda}_i$ $(i = 1, 2)$ represent the rescaled molecular and eddy viscosities, respectively.

In the limit of $Y \to \pm\infty$, $T^\dagger$ in (2.47) and $Q^\dagger$ in (2.48) can be matched respectively with the outer expansions of $\hat{T}_0 + \epsilon^{1/2}\hat{T}_1^{\langle 1\rangle}$ and $\partial_r \hat{u}_1^{\langle 1\rangle}$ near $r = r_c^{\pm}$, which can be derived easily using (2.18) and (2.26).

The jump $(d_2^{\langle 1\rangle +} - d_2^{\langle 1\rangle -})$ for the fundamental component is determined by matching the outer and inner solutions, $\epsilon^{3/2}\hat{u}_1$ and $\epsilon^{3/2}\tilde{u}_1$, which gives

$$\tilde{u}_1(Y \to \infty) - \tilde{u}_1(Y \to -\infty) = \hat{u}_1(r = r_c^+) - \hat{u}_1(r = r_c^-). \tag{2.50}$$

The harmonics in the inner solution are selected by integrating $Q^\dagger\, \mathrm{e}^{-\mathrm{i}n\alpha\zeta}$ with respect to ζ over one axial wavelength $2\pi/\alpha$. Integrating the resulting expression further with respect to Y yields the jumps $(d_2^{\langle n\rangle +} - d_2^{\langle n\rangle -})$ $(n = 1, 2, \ldots)$. As is indicated above, of all harmonic components, only the jump in the fundamental mode (including its sideband components) is required to balance the outer solution. The jump with $n = 1$ is just the left-hand side of (2.50), which is inserted along with (2.29) into (2.28), leading to the evolution equation for the amplitude $A^\dagger$:

$$\frac{\alpha}{2\pi}\int_{-\infty}^{\infty}\int_0^{2\pi/\alpha} Q^\dagger\, \mathrm{e}^{-\mathrm{i}\alpha\zeta}\,\mathrm{d}\zeta\,\mathrm{d}Y = \frac{\bar{T}_c}{\alpha^2}\left[\frac{2\mathrm{i}}{\alpha}J_{r2}\frac{\partial A^\dagger}{\partial \tau} - \frac{2\mathrm{i}}{\alpha}\left(\frac{J_{r1}}{c} - J_{r2}\right)\frac{\partial A^\dagger}{\partial \bar{x}} - J_{r0}\bar{x}A^\dagger\right]. \tag{2.51}$$

The evolution–modulation system thus consists of the coupled amplitude equation (2.51), temperature equation (2.47) and vorticity equation (2.48). When the limit $r_c^{-1} \to 0$ is taken, these three equations reduce to those in the planar case in [I], as expected.

2.4.2. *Jump in the mean-flow distortion: acoustic source from the critical layer*

Now we turn to consider the solutions for the mean-flow distortion and its jump, which are relevant for analysing the acoustic radiation. The dominant mean-flow distortion has axial and radial velocities, contained in $\epsilon^{3/2}\tilde{u}_1$ and $\epsilon^2\tilde{v}_2$, respectively, but unlike the fundamental, the mean-flow (i.e. ζ-independent) component in $\tilde{u}_1$ is confined within the critical layer since its jump, i.e. the integration $\int_{-\infty}^{\infty}\int_0^{2\pi/\alpha} Q^\dagger\,\mathrm{d}\zeta\,\mathrm{d}Y = 0$. The continuity and energy equations at $O(\epsilon^{3/2})$ are combined to give the equation

$$\bar{T}_c\frac{\partial \tilde{v}_2^{\langle 0\rangle}}{\partial Y} = \frac{\bar{\lambda}\bar{T}_c\mu_c}{Pr}\frac{\partial^2}{\partial Y^2}\tilde{T}_0^{\langle 0\rangle} + \frac{\tilde{\lambda}\bar{T}_c\tilde{\mu}_{t,c}}{\widetilde{Pr}_T}\frac{\partial^2}{\partial Y^2}\tilde{T}_0^{\langle 0\rangle}(t - \hat{\tau}_1); \tag{2.52}$$

here and in the following, the superscript '$\langle 0\rangle$' denotes the quantities without dependence on ζ, i.e. the components of the mean-flow distortion. The jump of $\tilde{v}_2^{\langle 0\rangle}$ across the critical layer is identically zero since the integration of (2.52) with respect to Y from $-\infty$ to ∞ vanishes. What is responsible for acoustic emission is the subdominant mean-flow distortion, which has smaller $O(\epsilon^2\tilde{u}_2)$ and $O(\epsilon^{5/2}\tilde{v}_3)$ axial and radial

https://doi.org/10.1017/jfm.2022.252 Published online by Cambridge University Press

velocities, respectively. Matching $\tilde{v}_3$ with the outer inviscid solution requires

$$v_M(r = r_c^+) - v_M(r = r_c^-) = \tilde{v}_3^{\langle 0\rangle}(Y \to \infty) - \tilde{v}_3^{\langle 0\rangle}(Y \to -\infty). \tag{2.53}$$

From the $O(\epsilon^2)$ terms of the continuity equation, we obtain,

$$\frac{\partial \tilde{u}_1^{\langle 0\rangle}}{c\partial \bar{x}} + \frac{\partial \tilde{v}_3^{\langle 0\rangle}}{\partial Y} + \frac{\tilde{v}_2^{\langle 0\rangle}}{r_c} = \frac{\bar{\lambda}\mu_c}{Pr}\frac{\partial^2 \tilde{T}_1^{\langle 0\rangle}}{\partial Y^2} + \frac{\tilde{\lambda}\tilde{\mu}_{t,c}}{\widetilde{Pr}_T}\frac{\partial^2 \tilde{T}_1^{\langle 0\rangle}(t-\hat{\tau}_1)}{\partial Y^2} - \frac{\bar{T}_{1,c}\bar{x}}{\bar{T}_c^2}\mathcal{L}_N^{\dagger}\tilde{T}_0^{\langle 0\rangle} - \frac{\bar{\lambda}}{Pr}\left(\mu_c' + \mu_c\frac{\bar{T}_{1,c}\bar{x}}{\bar{T}_c}\right)\frac{\partial^2 \tilde{T}_0^{\langle 0\rangle}}{\partial Y^2} - \frac{\tilde{\lambda}\bar{T}_{1,c}\bar{x}}{\widetilde{Pr}_T\bar{T}_c}\tilde{\mu}_{t,c}\frac{\partial^2 \tilde{T}_0^{\langle 0\rangle}(t-\hat{\tau}_1)}{\partial Y^2}. \tag{2.54}$$

Due to the fact that $\partial_Y \tilde{T}_1 \to 0$ as $Y \to \pm\infty$, there is no need to derive the equation for $\tilde{T}_1$. Integrating (2.54) with respect to Y, we obtain the jump,

$$\tilde{v}_3^{\langle 0\rangle}(Y \to \infty) - \tilde{v}_3^{\langle 0\rangle}(Y \to -\infty) = -\int_{-\infty}^{\infty}\frac{\partial \tilde{u}_1^{\langle 0\rangle}(\tau, \bar{x}, Y)}{c\partial \bar{x}}\,\mathrm{d}Y - \int_{-\infty}^{\infty}\frac{\tilde{v}_2^{\langle 0\rangle}(\tau, \bar{x}, Y)}{r_c}\,\mathrm{d}Y. \tag{2.55}$$

Here, the first term on the right-hand side is the same as that in [I], and the second term is found to be zero by integrating (2.52) twice with respect to Y. The jump of v_M across the critical layer is contributed only from the axial velocity, consistent with that in [I]. This jump is measured by

$$\mathcal{U} = \left(\frac{\partial}{\partial \tau} + \frac{\partial}{\partial \bar{x}}\right)\int_{-\infty}^{\infty}\tilde{u}_1^{\langle 0\rangle}(\tau, \bar{x}, Y)\,\mathrm{d}Y. \tag{2.56}$$

This result shows that while the dominant mean-flow distortion $\tilde{u}_1^{\langle 0\rangle}$ is confined within the critical layer, its spatial–temporal variation contributes to the generation in the main jet of a subdominant mean-flow distortion v_M, which emits sound waves. Thus $\mathcal{U}$ forms an important part of the source. It worth noting that $\mathcal{U}$ is driven ultimately by the quadratic interaction of the CS through the nonlinear terms on the right-hand side of (2.48), as well as in the operators defined by (2.49), and one may thus be tempted to view those nonlinear terms as an acoustic source, but the 'mapping' from them to $\mathcal{U}$ is a strongly nonlinear and viscous process, which cannot be accounted for by linear inviscid acoustic analogy operators.

Fourier transforming (2.55) and inserting the resulting relation into (2.53) and (2.40), we arrive at the expression for $\widehat{a_M^+}$:

$$\widehat{a_M^+}(\omega, \kappa) = \frac{\mathrm{i}\kappa\,\hat{\mathcal{U}}(\omega, \kappa)}{c(\kappa - \omega)^2} + \hat{\mathcal{I}}_R(\omega, \kappa), \tag{2.57}$$

which will be recognised as the mathematically equivalent low-frequency sound source.

2.5. *Acoustic radiation on the basis of first principles*

Unlike the fundamental and its harmonics which decay exponentially in the radial direction, the mean-flow distortion decays algebraically, as (2.38) indicates. The governing equations (2.33) (and (2.36)), which are essentially long-wavelength Euler (and Rayleigh) equations, become invalid in the far field where $r = O(\epsilon^{-1/2})$. It follows from expansion

https://doi.org/10.1017/jfm.2022.252 Published online by Cambridge University Press

(2.32) and the solution (2.38) for v_M in the main jet flow that in the far field, the spatially and temporally modulated mean flow scales as $\epsilon^3(\tilde{U}, \tilde{V}, \tilde{T}, \tilde{P})$. Here the flow quantities are functions of τ, $\bar{x}$ and the radial variable $\bar{r}$ defined by (2.11). The governing equations become

$$\begin{cases} \dfrac{\bar{T}_+}{c}\left(\dfrac{\partial \tilde{U}}{\partial \bar{x}} + \dfrac{\partial \tilde{V}}{\partial \bar{r}} + \dfrac{\tilde{V}}{\bar{r}}\right) = \mathcal{D}_+(\tilde{T} - \gamma Ma^2 \bar{T}_+ \tilde{P}), & (2.58a) \\ \mathcal{D}_+(\tilde{U}, \tilde{V}) = -\dfrac{\bar{T}_+}{c}\left(\dfrac{\partial}{\partial \bar{x}}, \dfrac{\partial}{\partial \bar{r}}\right)\tilde{P}, & (2.58b) \\ \mathcal{D}_+ \tilde{T} = (\gamma - 1)\, Ma^2 \bar{T}_+ \mathcal{D}_+ \tilde{P}, & (2.58c) \end{cases}$$

in which we have introduced the operator $\mathcal{D}_+ \equiv \partial_\tau + (\bar{U}_+/c)\partial_{\bar{x}}$. Elimination of $\tilde{U}$, $\tilde{V}$ and $\tilde{T}$ leads to the two-dimensional convected wave equation for $\tilde{P}$,

$$Ma^2 \mathcal{D}_+^2 \tilde{P} = \frac{\bar{T}_+}{c^2}\left(\frac{\partial^2}{\partial \bar{x}^2} + \frac{\partial^2}{\partial \bar{r}^2} + \frac{\partial}{\bar{r}\,\partial \bar{r}}\right)\tilde{P}, \tag{2.59}$$

indicating that the unsteady 'mean-flow' distortion has now acquired the character of sound. Equation (2.59) is subject to the Neumann boundary condition

$$\frac{\partial \tilde{P}}{\partial \bar{r}} \to -\frac{r_c}{\bar{r}\bar{T}_+}\mathcal{D}_+^2\, a_M^+(\tau, \bar{x}) \quad \text{as } \bar{r} \to 0, \tag{2.60}$$

which is obtained by matching with the main shear layer, $\tilde{V}(\bar{r} \to 0^+) = v_M(r \to \infty)$. It transpires that $a_M^+(\tau, \bar{x})$ indeed plays the role of the equivalent acoustic source of the low-frequency sound. Interestingly, the equivalent sound source is determined beforehand, unlike the planar case, where the equivalent source has to be obtained simultaneously with the acoustic field as part of the solution.

We solve the wave equation (2.58) in the frequency–wavenumber space, which becomes

$$\begin{cases} \left[\dfrac{\partial^2}{\partial \bar{r}^2} + \dfrac{\partial}{\bar{r}\,\partial \bar{r}} + \mathscr{K}_+^2(\omega, \kappa)\right]\hat{P}(\omega, \kappa, \bar{r}) = 0, & (2.61a) \\ \left.\dfrac{\partial \hat{P}}{\partial \bar{r}}\right|_{\bar{r}\to 0} = \dfrac{r_c}{c^2 \bar{T}_+ \bar{r}}(\bar{U}_+\kappa - c\,\omega)^2 \widehat{a_M^+}(\omega, \kappa), & (2.61b) \end{cases}$$

with

$$\mathscr{K}_+(\omega, \kappa) = \sqrt{Ma^2(\bar{U}_+\kappa - c\,\omega)^2/\bar{T}_+ - \kappa^2}. \tag{2.62}$$

The solution can be worked out as

$$\hat{P}(\omega, \kappa, \bar{r}) = -\hat{\mathcal{E}}_0(\omega, \kappa)\, \widehat{a_M^+}(\omega, \kappa)\, \mathrm{H}_0^{(1)}(\mathscr{K}_+ \bar{r}), \tag{2.63}$$

where $\mathrm{H}_0^{(1)}$ is the zeroth-order Hankel function of the first kind, and $\hat{\mathcal{E}}_0(\omega, \kappa)$ is determined by the boundary condition as

$$\hat{\mathcal{E}}_0(\omega, \kappa) = \frac{\mathrm{i}\pi r_c}{2c^2 \bar{T}_+}(\bar{U}_+\kappa - c\,\omega)^2. \tag{2.64}$$

As (2.57) and (2.41) indicate, the direct physical sources correspond to $\hat{\mathcal{S}}_R$ and $\mathcal{U}$. The first of these represents the usual Reynolds stresses generated by nonlinear interactions of

https://doi.org/10.1017/jfm.2022.252 Published online by Cambridge University Press

CS in the main jet flow, and acts as an inhomogeneous term of a linear equation (2.36). The second, $\mathcal{U}$, is driven by Reynolds stresses associated with the nonlinear interactions of CS in the critical layer, but its generation is a strongly nonlinear and viscous process as is indicated by (2.47) and (2.48). As a conclusion to be emphasised again, it is the slowly spatial–temporal undulation of the (subdominant) mean-flow distortion generated by the nonlinear interactions of the CS that emits sound waves.

The acoustic field pressure is $\epsilon^3\,\tilde{P}(\tau,\bar{x},\bar{r})$, with $\tilde{P}(\tau,\bar{x},\bar{r})$ being given by the inverse Fourier transform as

$$\tilde{P}(\tau,\bar{x},\bar{r}) = -\frac{1}{4\pi^2}\int_{-\infty}^{\infty} \mathrm{e}^{-\mathrm{i}\omega\tau}\,\mathrm{d}\omega \int_{-\infty}^{\infty} \hat{\mathcal{E}}_0(\omega,\kappa)\,\widehat{a_M^+}(\omega,\kappa)\,\mathrm{H}_0^{(1)}(\mathscr{K}_+\bar{r})\,\mathrm{e}^{\mathrm{i}\kappa\bar{x}}\,\mathrm{d}\kappa. \tag{2.65}$$

Of primary interest is the acoustics in the far field, which we now analyse by introducing a pair of variables $(\bar{R},\bar{\varphi})$ with

$$\bar{R} = \sqrt{\bar{x}^2+\bar{r}^2}, \quad \tan\bar{\varphi} = \bar{r}/\bar{x} \quad (0\leqslant\bar{\varphi}\leqslant\pi). \tag{2.66}$$

The acoustic pressure could be approximated asymptotically by the stationary-phase method. Note first that as $\bar{R}\to\infty$,

$$\mathrm{H}_0^{(1)}(\mathscr{K}_+\bar{r}) = \mathrm{H}_0^{(1)}\left(\mathscr{K}_+\bar{R}\sin\bar{\varphi}\right) \to \sqrt{2/\left(\pi\mathscr{K}_+\bar{R}\sin\bar{\varphi}\right)}\exp\left[\mathrm{i}\left(\mathscr{K}_+\bar{R}\sin\bar{\varphi}-\pi/4\right)\right]. \tag{2.67}$$

In the inner integral of (2.65), the phase equation is introduced by

$$\phi(\omega,\kappa,\bar{\varphi}) = \left(\mathscr{K}_+\bar{r}+\kappa\bar{x}\right)/\bar{R} = \mathscr{K}_+\sin\bar{\varphi}+\kappa\cos\bar{\varphi}, \tag{2.68}$$

which has a stationary point κ_s satisfying $\partial_\kappa\phi(\omega,\kappa,\bar{\varphi})=0$ at

$$\begin{aligned}\kappa = \kappa_s(\omega,\bar{\varphi}) &= \left[\frac{\mathrm{sgn}(\omega)\,\bar{T}_+\cos\bar{\varphi}}{\sqrt{\bar{T}_+ - Ma^2\bar{U}_+^2\sin^2\bar{\varphi}}} - Ma\,\bar{U}_+\right]\frac{Ma\,c\,\omega}{\bar{T}_+ - Ma^2\bar{U}_+^2}\\ &= \left[\frac{\mathrm{sgn}(\omega)\cos\bar{\varphi}}{\sqrt{1-Ma_+^2\sin^2\bar{\varphi}}} - Ma_+\right]\frac{Ma_+\,c\,\omega}{\bar{U}_+(1-Ma_+^2)},\end{aligned} \tag{2.69}$$

where $Ma_+ = \bar{U}_+\bar{T}_+^{-1/2}Ma = (\beta_U\beta_T^{-1/2})Ma_I < 1$ in the subsonic regime, with $\beta_U = U_O^*/U_I^*$. It can be verified that the condition $Ma^2(\bar{U}_+\kappa_s - c\,\omega)^2/\bar{T}_+ - \kappa_s^2 > 0$, which leads to a wave form, is always satisfied. If the jet is without a coflow, namely $\bar{U}_+=0$, then (2.69) simplifies to a form similar to (3.49) of Wu & Huerre (2009).

The far-field pressure in the region $\bar{R}\gg 1$ is given by

$$\begin{aligned}\tilde{P} \sim -\frac{1}{2\pi^2\bar{R}}\int_{-\infty}^{\infty} &\frac{\exp(\mathrm{sgn}[\partial_{\kappa\kappa}^2\phi''_{\kappa\kappa}(\omega,\kappa_s,\bar{\varphi})]\,\mathrm{i}\pi/4-\mathrm{i}\pi/4)\,\hat{\mathcal{E}}_0(\omega,\kappa_s)\,\widehat{a_M^+}(\omega,\kappa_s)}{\sqrt{|\partial_{\kappa\kappa}^2\phi(\omega,\kappa_s,\bar{\varphi})|\,\mathscr{K}_+(\omega,\kappa_s)\sin\bar{\varphi}}}\\ &\times\exp(\mathrm{i}\phi(\omega,\kappa_s,\bar{\varphi})\,\bar{R}-\mathrm{i}\omega\tau)\,\mathrm{d}\omega,\end{aligned} \tag{2.70}$$

where

$$\partial_{\kappa\kappa}^2\phi(\omega,\kappa_s,\bar{\varphi}) = \frac{(Ma^2\bar{U}_+^2-\bar{T}_+)\sin\bar{\varphi}}{\sqrt{\bar{T}_+Ma^2(\bar{U}_+\kappa-c\,\omega)^2-\bar{T}_+^2\kappa_s^2}} + \frac{Ma^2\bar{U}_+(\bar{U}_+\kappa-c\,\omega)-\bar{T}_+\kappa_s}{Ma^2(\bar{U}_+\kappa-c\,\omega)^2-\bar{T}_+\kappa_s^2}\cos\bar{\varphi}. \tag{2.71}$$

https://doi.org/10.1017/jfm.2022.252 Published online by Cambridge University Press

It is found that $\kappa_s^{-2}\,\hat{\mathcal{E}}_0(\omega,\kappa_s)$ and $\mathscr{K}_+(\omega,\kappa_s)\,\partial^2_{\kappa\kappa}\phi(\omega,\kappa_s,\bar{\varphi})$ are functions only of the radiating angle $\bar{\varphi}$, so we could introduce

$$\mathscr{D}_p(\bar{\varphi}) = r_c\left|\mathscr{K}_+(\omega,\kappa_s)\,\partial^2_{\kappa\kappa}\phi(\omega,\kappa_s,\bar{\varphi})\sin\bar{\varphi}\right|^{-1/2}\kappa_s^{-2}\,\hat{\mathcal{E}}_0(\omega,\kappa_s), \tag{2.72}$$

$$\mathscr{S}(\omega,\bar{\varphi}) = \kappa_s^2\,\widehat{a^+_M}(\omega,\kappa_s) = \kappa_s^2\left[\frac{\mathrm{i}\kappa\,\hat{\mathcal{U}}(\omega,\kappa_s)}{c(\kappa_s-\omega)^2} + \frac{1}{r_c}\int_0^\infty \frac{r\,\hat{\mathcal{S}}_R(\omega,\kappa_s,r)}{(\bar{U}\kappa_s/c-\omega)^2}\,\mathrm{d}r\right]. \tag{2.73}$$

The quantity $\kappa_s^2\mathscr{D}_p$ may be interpreted as the 'refraction coefficient' of the mean flow (cf. Wu & Huerre 2009) since it is independent of the evolution and modulation of CS, with the latter effects being encapsulated in $\widehat{a^+_M}(\omega,\kappa_s)$.

In terms of $\mathscr{D}_p(\bar{\varphi})$ and $\mathscr{S}(\omega,\bar{\varphi})$, the solution (2.70) can be written as

$$\begin{aligned}\tilde{P}(\tau,\bar{R},\bar{\varphi}) \sim \frac{\mathscr{D}_p(\bar{\varphi})}{2\pi^2\bar{R}}\int_{-\infty}^{\infty} &\exp(\mathrm{sgn}[\partial^2_{\kappa\kappa}\phi(\omega,\kappa_s,\bar{\varphi})]\,\mathrm{i}\pi/4-\mathrm{i}\pi/4)\,\mathscr{S}(\omega,\bar{\varphi})\\ &\times\exp(\mathrm{i}\phi(\omega,\kappa_s,\bar{\varphi})\bar{R}-\mathrm{i}\omega\tau)\,\mathrm{d}\omega.\end{aligned} \tag{2.74}$$

The intensity of the overall acoustic pressure measured by the root-mean-square value is found by using Parseval's theorem as

$$\tilde{P}_{rms}(\bar{R},\bar{\varphi}) = \sqrt{\overline{\tilde{P}^{+2}}} = \frac{\mathscr{D}(\bar{\varphi})}{4\pi^3\bar{R}}, \tag{2.75}$$

where $\mathscr{D}(\bar{\varphi})$ is the directivity function that is a superposition of the corresponding spectrum function $\mathscr{S}(\omega,\bar{\varphi})$:

$$\mathscr{D}(\bar{\varphi}) = \left|\mathscr{D}_p(\bar{\varphi})\right|\sqrt{\int_{-\infty}^{\infty}|\mathscr{S}(\omega,\bar{\varphi})|^2\,\mathrm{d}\omega}. \tag{2.76}$$

3. Governing systems

3.1. *Coupled equations for dynamics*

The remaining tasks of the present paper are to solve the evolution–modulation system of the CS and to calculate the sound waves radiated to the far field.

As in [I], the dynamical system consists of three coupled equations, (2.51), (2.47) and (2.48), together with the corresponding upstream-boundary conditions. For numerical calculations, rescaled variables $\tilde{A}$, $\tilde{T}$ and $\tilde{Q}$ are introduced as

$$\tilde{A} = \alpha^2\bar{U}_c'A^\dagger,\quad \tilde{T} = T^\dagger,\quad \tilde{Q} = -\alpha^2\bar{U}_c'Q^\dagger/j \overset{\text{def.}}{=\!=} Q^\dagger/p_Q, \tag{3.1a–c}$$

https://doi.org/10.1017/jfm.2022.252 Published online by Cambridge University Press

in order to simplify the coefficients in the operators. The coupled equations then become

$$\begin{cases} \dfrac{1}{2\pi}\displaystyle\int_{-\infty}^{\infty}\int_{0}^{2\pi} \tilde{Q}\,\mathrm{e}^{-\mathrm{i}\bar{\xi}}\,\mathrm{d}\bar{\xi}\,\mathrm{d}\bar{\eta} = \mathrm{i}\Lambda_1\dfrac{\partial\tilde{A}}{\partial\tau} + \mathrm{i}\Lambda_2\dfrac{\partial\tilde{A}}{\partial\bar{x}} + \Lambda_0\bar{x}\tilde{A}, & (3.2a)\\ \mathcal{L}_{N,1}\tilde{T} = -\left[\left(p_1\dfrac{\partial}{\partial\tau} + p_1\dfrac{\partial}{\partial\bar{x}} - \mathrm{i}p_2 - \mathrm{i}\chi_1\bar{x}\right)\tilde{A}\,\mathrm{e}^{\mathrm{i}\bar{\xi}} + \mathrm{c.c.}\right], & (3.2b)\\ \mathcal{L}_{N,2}\tilde{Q} = -p_3\left[\bar{\lambda}_3\dfrac{\partial^2\tilde{T}}{\partial\bar{\eta}^2} + \tilde{\lambda}_3\dfrac{\partial^2\tilde{T}(t-\hat{\tau}_1)}{\partial\bar{\eta}^2} + \left(\mathrm{i}\tilde{A}\,\mathrm{e}^{\mathrm{i}\bar{\xi}} + \mathrm{c.c.} - \chi\right)\dfrac{\partial\tilde{T}}{\partial\bar{\eta}}\right] \\ \qquad\qquad -\left[\left(\dfrac{\partial}{\partial\tau} + \dfrac{\partial}{\partial\bar{x}} - \mathrm{i}\chi_2\bar{x}\right)\tilde{A}\,\mathrm{e}^{\mathrm{i}\bar{\xi}} + \mathrm{c.c.}\right], & (3.2c) \end{cases}$$

where we have renormalised the axial and local transverse coordinates,

$$\bar{\xi} = \alpha\zeta, \quad \bar{\eta} = \alpha(\bar{U}_c' Y + \bar{U}_{1,c}\bar{x}), \tag{3.3a,b}$$

and the strongly nonlinear operators now read

$$\mathcal{L}_{N,i}\bullet \equiv \left[\frac{\partial}{\partial\tau} + \frac{\partial}{\partial\bar{x}} + \bar{\eta}\frac{\partial}{\partial\bar{\xi}} - (\mathrm{i}\tilde{A}\,\mathrm{e}^{\mathrm{i}\bar{\xi}} + \mathrm{c.c.} - \chi)\frac{\partial}{\partial\bar{\eta}} - \bar{\lambda}_i\frac{\partial^2}{\partial\bar{\eta}^2}\right]\bullet - \tilde{\lambda}_i\frac{\partial^2\bullet(t-\hat{\tau}_i)}{\partial\bar{\eta}^2} \tag{3.4}$$

for $i = 1, 2$. The parameters in the system are

$$\left.\begin{gathered} \chi = \alpha c^{-1}(c\bar{U}_{1,c} + \sigma\bar{U}_c'\bar{V}_c), \\ \chi_1 = (\bar{U}_c'\bar{T}_{1,c}' - \bar{U}_{1,c}\bar{T}_c'')/(\alpha\bar{U}_c'^2), \quad \chi_2 = (j\bar{U}_{1,c} - \bar{U}_c' j_1)/(\alpha\bar{U}_c' p_Q); \\ p_1 = \bar{T}_c''/(\alpha\bar{U}_c'^2), \quad p_2 = \bar{T}_{cM}'/(\alpha\bar{U}_c'), \quad p_3 = \bar{U}_c'/(\bar{T}_c p_Q); \\ [\Lambda_0, \Lambda_1, \Lambda_2] = -\mathrm{sgn}(\bar{U}_c')\,\bar{T}_c(\alpha^4 p_Q)^{-1}[\alpha J_{r0}, -2J_{r2}, 2(J_{r1}/c - J_{r2})]; \\ \bar{\lambda}_1 = \bar{\lambda}\bar{T}_c\mu_c(\alpha\bar{U}_c')^2/Pr, \quad \bar{\lambda}_2 = \bar{\lambda}\bar{T}_c\mu_c(\alpha\bar{U}_c')^2, \quad \bar{\lambda}_3 = \bar{\lambda}\bar{T}_c(\mu_c/Pr - \mu_c'\bar{T}_c)(\alpha\bar{U}_c')^2; \\ \tilde{\lambda}_1 = \tilde{\lambda}\bar{T}_c\tilde{\mu}_{t,c}(\alpha\bar{U}_c')^2/\widetilde{Pr}_T, \quad \tilde{\lambda}_2 = \tilde{\lambda}\bar{T}_c\tilde{\mu}_{t,c}(\alpha\bar{U}_c')^2, \quad \tilde{\lambda}_3 = \tilde{\lambda}\bar{T}_c\tilde{\mu}_{t,c}(\alpha\bar{U}_c')^2/\widetilde{Pr}_T. \end{gathered}\right\} \tag{3.5}$$

The present system for the ring-mode CS on a circular jet is formally the same as the planer case in [I], which means that the upstream-boundary conditions could be borrowed from § 4 in [I]. A minor difference is that χ_2 in the planar case turns out to be zero (see (6.33) in [I]) due to the self-similarity of the mean-flow profile, but in a circular jet, this parameter is non-zero in general.

In the limit $r_c \to \infty$, J_{ri} $(i = 0, 1, 2)$ and χ_2 reduce to those in [I] as expected, and can further simplify to those for a laminar mixing layer (Sparks & Wu 2008) when the parameters representing the effect of fine-scale turbulence and non-parallelism are set to zero. It is also worth pointing out that the present dynamical system can be applied also to *subsonic* ring/planar mode CS on a supersonic jet/mixing layer. Moreover, the analysis of the low-frequency acoustic radiation can be extended accordingly. We note that the jump (2.56) and the governing equations (2.33*a*)–(2.33*e*) remain valid. A complication is that an 'envelope critical level' arises, where $\bar{U} = c\omega/\kappa$ and the solution becomes singular. The singularity could be removed by reintroducing the non-parallelism of the mean flow. The result will be reported in another paper.

https://doi.org/10.1017/jfm.2022.252 Published online by Cambridge University Press

3.2. *Fourier decomposition and sideband instability*

A modulated wavepacket may be represented by a disturbance consisting of two or more instability modes with slightly different frequencies, e.g. ω_0 and ω_1, which differ by $O(\epsilon^{1/2})$, i.e. $|\omega_0 - \omega_1| = \omega_\nu = \epsilon^{1/2}\Delta$, with $\Delta = O(1)$ being the scaled frequency difference. The corresponding wavenumbers, α and α_1, differ by $O(\epsilon^{1/2})$ also, i.e. $|\alpha - \alpha_1| = O(\epsilon^{1/2})$, so the two waves are in the 'sideband' of each other. More generally, a wavepacket may consist of a discrete set, or a continuum, of sideband modes.

For the case of discrete sideband, the amplitude $\tilde{A}$ is expanded as a Fourier series:

$$\tilde{A} = A(\tau, \bar{x})\,\mathrm{e}^{-\mathrm{i}S_0\tau} = \sum_{L=-\infty}^{\infty} A^{(L)}(\bar{x})\exp(-\mathrm{i}L\Delta\tau - \mathrm{i}S_0\tau), \tag{3.6}$$

where $\epsilon^{1/2}S_0$ measures the deviation of the central frequency ω_0 of the CS from that of the neutral mode, namely $\omega_0 = \alpha c + \epsilon^{1/2}S_0$, in which α and c are the wavenumber and phase speed of the neutral mode, respectively. A double Fourier decomposition is necessary for temperature $\tilde{T}$ and vorticity $\tilde{Q}$, namely,

$$\begin{aligned}\left[\tilde{T}, \tilde{Q}\right] &= \sum_{n=-\infty}^{\infty} [T_n(\tau, \bar{x}, \eta), Q_n(\tau, \bar{x}, \eta)]\exp(\mathrm{i}n(\bar{\zeta} - S_0\tau)) \\ &= \sum_{n=-\infty}^{\infty}\sum_{L=-\infty}^{\infty}\left[T_n^{(L)}(\bar{x}, \eta), Q_n^{(L)}(\bar{x}, \eta)\right]\exp(-\mathrm{i}L\Delta\tau + \mathrm{i}n(\bar{\zeta} - S_0\tau)), \end{aligned} \tag{3.7a,b}$$

with $\eta = \bar{\eta} - S_0$. The reality condition demands that $T_{-n} = T_n^*$, $T_{-n}^{(L)} = T_n^{(-L)*}$, and similarly for Q_n and $Q_n^{(L)}$.

The disturbance upstream is exponentially small so the nonlinearity is quite weak. Omitting the nonlinear terms, the equation is reduced to

$$\frac{\partial\tilde{A}}{\partial\bar{x}} + \frac{1}{c_g}\frac{\partial\tilde{A}}{\partial\tau} = \sigma_s\bar{x}\tilde{A}, \tag{3.8}$$

where c_g is the group velocity,

$$c_g = (\pi + \mathrm{i}\Lambda_2)/(\pi + \mathrm{i}\Lambda_1), \tag{3.9}$$

and

$$\sigma_s = (\mathrm{i}\pi\chi_2 - \Lambda_0)/(\pi + \mathrm{i}\Lambda_2) \tag{3.10}$$

measures the effect of non-parallelism.

We consider a particular form of disturbance that consists of three modes upstream. The upstream condition for the amplitudes of the seeded modes is then given by

$$\begin{aligned}\tilde{A} \to &(a_0^-\exp(\mathrm{i}\varphi_0^-)\exp(-\kappa_\nu\bar{x} + \mathrm{i}\Delta\tau) + a_0 + a_0^+\exp(\mathrm{i}\varphi_0^+)\exp(\kappa_\nu\bar{x} - \mathrm{i}\Delta\tau)) \\ &\times\exp(\sigma_s\bar{x}^2/2 + \kappa_l\bar{x} - \mathrm{i}S_0\tau)\end{aligned} \tag{3.11}$$

as $\bar{x} \to -\infty$, or equivalently,

$$\begin{aligned}[A^{(-1)}, A^{(0)}, A^{(1)}] \to &[a_0^-\exp(\mathrm{i}\varphi_0^-)\exp(-\kappa_\nu\bar{x}), a_0, a_0^+\exp(\mathrm{i}\varphi_0^+)\exp(\kappa_\nu\bar{x})] \\ &\times\exp(\sigma_s\bar{x}^2/2 + \kappa_l\bar{x}),\end{aligned} \tag{3.12}$$

and $A^{(L)} \to 0$ for other $|L| \geqslant 2$ as $\bar{x} \to -\infty$. Here, $a_0^\pm$, $\varphi_0^\pm$ and $\kappa_l \pm \kappa_\nu$ represent the initial amplitudes, phases and linear growth rates of the upper and lower sidebands, respectively,

https://doi.org/10.1017/jfm.2022.252 Published online by Cambridge University Press

whose frequencies are $\omega_0 \pm \omega_\nu = \omega_0 \pm \epsilon^{1/2}\Delta = \alpha c + \epsilon^{1/2}(S_0 \pm \Delta)$. Inserting (3.11) into (3.8), we have $\kappa_l = \mathrm{i}S_0/c_g$ and $\kappa_\nu = \mathrm{i}\Delta/c_g$.

The Fourier decompositions (3.6) and (3.7) are substituted into the coupled equations (3.2) to obtain the equations for $A^{(L)}$, $T_n^{(L)}$ and $Q_n^{(L)}$ as (4.27) in [I]; these equations, together with their upstream-boundary conditions, are listed in Appendix B. It should be noted that the nonlinear terms must be calculated as the Cauchy products or the discrete convolutions with respect to τ, due to the presence of sidebands,

$$f^{(L)} = f_1^{(L)} * f_2^{(L)} = \sum_{k=-\infty}^{\infty} f_1^{(k)} f_2^{(L-k)}, \tag{3.13}$$

where $f_k^{(L)}$ stands for the coefficient of the $\exp(-\mathrm{i}L\Delta\tau)$ component. This nonlinear operation characterises the interactions between the sidebands within the corresponding fundamental, harmonics or mean-flow distortion.

3.3. *Physical sound source and the acoustic features*

The low-frequency acoustic far field is characterised by the directivity $\mathscr{D}(\bar{\varphi})$ (see (2.76)) and spectrum $|\mathscr{S}(\omega, \bar{\varphi})|$ (see (2.73)). The spectrum is a function of the equivalent sound source a_M^+, which consists of $\mathcal{U}$ and $\mathcal{I}_R$. Letting f represent any of these quantities, we have the decomposition

$$f(\bar{x}, \bar{\varphi}; \tau) = \sum_{L=-\infty}^{\infty} f^{(L)}(\bar{x}, \bar{\varphi}) \exp(-\mathrm{i}L\Delta\tau). \tag{3.14}$$

Thus we have

$$\widehat{a_M^+}^{(L)}(\kappa) = \frac{\mathrm{i}\kappa\, \hat{\mathcal{U}}^{(L)}(\kappa)}{c(\kappa - L\Delta)^2} + \frac{1}{r_c}\int_0^\infty \frac{r\, \hat{\mathcal{S}}_R^{(L)}(\kappa, r)}{[\bar{U}(r)\,\kappa/c - L\Delta]^2}\,\mathrm{d}r, \tag{3.15}$$

where $\hat{\mathcal{U}}^{(L)}$ denotes the critical-layer contributed source component with frequency $\omega = L\omega_\nu$. From the critical-layer analysis (see also (5.23) in [I]), we may express it in terms of $A^{(L)}$ and $T_0^{(L)}$ as

$$\hat{\mathcal{U}}^{(L)}(\kappa) = \frac{\mathrm{i}p_Q}{\alpha^2 \bar{U}_c'^2}\left[(\Lambda_2\kappa - \Lambda_1\omega)\,\widehat{B^{(L)}} + p_3(\kappa - L\Delta)\fint_{-\infty}^{\infty} \eta^* \widehat{T_0^{(L)}}(\kappa, \eta^*)\,\mathrm{d}\eta^\star\right], \tag{3.16}$$

where we have defined $B(\tau, \bar{x}) \equiv |\tilde{A}(\tau, \bar{x})|^2$ so that

$$B^{(L)}(\bar{x}) = A^{(L)}(\bar{x}) * A^{(-L)*}(\bar{x}). \tag{3.17}$$

The contribution from the inviscid main shear layer to the acoustic source, $\hat{\mathcal{S}}_R^{(L)}$, is obtained by inserting the outer expansion of each flow quantity into $\mathcal{S}_R$ (see (2.37)). This is a function of $\hat{p}_0(r)$, $\hat{p}_0'(r)$, $J_{rj}^{\pm}(r)$ and S_{ik} ($i, k = 1, 2, 3$ and $j = 0, 1, 2$), namely,

$$\hat{\mathcal{S}}_R^{(L)}(\kappa, r) = -(\alpha^2 \bar{U}_c')^{-2}\,\widehat{B^{(L)}}[c^{-2}\kappa^2\,\tilde{\mathcal{S}}_1(r) + (\kappa - L\Delta)^2\,\tilde{\mathcal{S}}_2(r) + c^{-1}\kappa(\kappa - L\Delta)\,\tilde{\mathcal{S}}_3(r)], \tag{3.18}$$

where

$$\tilde{\mathcal{S}}_i(r) = S_{i0}^\dagger + S_{i1}^\dagger \hat{p}_0^2 + S_{i2}^\dagger \hat{p}_0'^2 + S_{i3}^\dagger \hat{p}_0' \hat{p}_0, \tag{3.19}$$

with the expressions for $S_{ij}^\dagger$ being given in Appendix C.

https://doi.org/10.1017/jfm.2022.252 Published online by Cambridge University Press

Each sound wave with a frequency $\omega = L\omega_v = \epsilon^{1/2}L\Delta$ has its own directivity, which is defined as

$$\mathscr{D}^{(L)}(\bar{\varphi}) = \left|\mathscr{D}_p(\bar{\varphi})\right| \left|\mathscr{S}^{(L)}\right|. \tag{3.20}$$

The overall directivity is introduced based on the acoustic energy distribution, namely,

$$\mathscr{D}(\bar{\varphi}) = \sqrt{\sum_{L=-\infty}^{\infty} \left[\mathscr{D}^{(L)}(\bar{\varphi})\right]^2} = \left|\mathscr{D}_p(\bar{\varphi})\right| \sqrt{\sum_{L=-\infty}^{\infty} \left|\mathscr{S}^{(L)}\right|^2}. \tag{3.21}$$

3.4. *Choice of the non-parallel mean-flow profile*

The theory is now applied to an axisymmetric circular jet formed between a core flow and a coflow. As in many previous studies, rather than solving the Reynolds-averaged compressible boundary-layer equations, we specify proper profiles of both the velocity and temperature agreeing with experimental data broadly. In this subsection, we determine the mean flow and related quantities, including $\bar{U}$, $\bar{V}$ (the scaled mean radial velocity), $\bar{T}$ and their derivatives with respect to r and $\tilde{x}$. The mean axial velocity profile is taken to be of the self-similar form

$$\bar{U} = \bar{U}_R + f[\eta^\dagger(\tilde{x}, r)], \tag{3.22}$$

where $\bar{U}_R = (U_I^* + U_O^*)/(U_I^* - U_O^*)$ denotes the dimensionless averaged velocity, which is related to the ratio of upstream velocities via $\beta_U = 1 - 2/(\bar{U}_R + 1)$, and $\eta^\dagger$ is the self-similar variable

$$\eta^\dagger(\tilde{x}, r) = \frac{r - R_0(\tilde{x})}{\delta_T(\tilde{x})} = \eta_c^\dagger + \frac{r - r_T(\tilde{x})}{\delta_T(\tilde{x})}, \tag{3.23}$$

where R_0 and δ_T, which are functions of $\tilde{x}$ defined by (2.6), represent the central position and the shear-layer thickness, respectively, and $\eta_c^\dagger$ denotes the location of the generalised inflection point and is independent of $\tilde{x}$, as (2.17) shows. It follows that

$$r_T = R_0 + \eta_c^\dagger \delta_T \tag{3.24}$$

and it represents the critical level at an arbitrary axial location $\tilde{x}$.

There are three typical positions in the radial direction, which are to be distinguished by subscripts '+', 'c' and 'a' denoting the quantities as $r \to \infty$, at the critical level r_c, and at $r = 0$, respectively. The phase speed of the neutral mode at the neutral position, c, is given by

$$c = \bar{U}_c = \bar{U}_R + f(\eta_c^\dagger). \tag{3.25}$$

The mean-temperature profile is obtained by the generalised Crocco's relation (see [I])

$$\bar{T}(\eta^\dagger) = -\sqrt{Pr_T}\,\frac{(\gamma - 1)\,Ma^2}{2}(\bar{U} - \bar{U}_a)(\bar{U} - \bar{U}_+) + \frac{1 - \beta_T}{2}(\bar{U} - \bar{U}_+) + \beta_T, \tag{3.26}$$

which can be deduced from the energy equation when the turbulent Prandtl number is $Pr_T = 1$.

To find the relationship between $\dot{r}_T$ and $\dot{\delta}_T$ (where a dot over a quantity denotes differentiation with respect to $\tilde{x}$), as well as the rescaled mean-flow radial velocity at the

https://doi.org/10.1017/jfm.2022.252 Published online by Cambridge University Press

critical level, we analyse the continuity and momentum equations of the mean flow. As is shown in Appendix D, $\dot{r}_T$ and $\bar{V}_c$ can be expressed as functions of $\dot{\delta}_T$ as

$$\frac{\dot{r}_T}{r_c} = \left(1 - 2\,\frac{\mathscr{C}_\infty^{(1)} - \bar{U}_+\mathscr{C}_c^{(1)}}{\mathscr{C}_\infty^{(0)} - \bar{U}_+\mathscr{C}_c^{(0)}}\right)\dot{\delta}_T - \frac{\mathscr{C}_\mu}{\mathscr{C}_\infty^{(0)} - \bar{U}_+\mathscr{C}_c^{(0)}}, \tag{3.27}$$

$$\bar{V}_c = \bar{T}_c[(r_c\bar{U}_c/\bar{T}_c - \mathscr{C}_c^{(0)})(\dot{r}_T/r_c) + (\mathscr{C}_\infty^{(0)} - 2\mathscr{C}_\infty^{(1)})\dot{\delta}_T], \tag{3.28}$$

in which $\mathscr{C}_\infty^{(i)}$, $\mathscr{C}_c^{(i)}$ and $\mathscr{C}_\mu$ are constants determined by the mean-flow profile, and their expressions and derivations are given in Appendix D. Here, $\dot{\delta}_T$ is related to the spreading rate of the shear-layer momentum thickness, as (3.34) would indicate.

For the self-similar mean-flow profile, the values of $\bar{U}_1$, $\bar{T}_1$ and $\bar{U}_1''$ (represented by F_1) can be found as

$$F_1 = \sigma\,\frac{\partial F}{\partial\tilde{x}}\bigg|_{\tilde{x}=\tilde{x}_N} = \sigma\left(\frac{\partial F}{\partial\eta^\dagger}\,\frac{\partial\eta^\dagger}{\partial\tilde{x}}\right)\bigg|_{\tilde{x}=\tilde{x}_N} = -\frac{\sigma}{\delta_T}\left[(r-r_c)\dot{\delta}_T/\delta_T + \dot{r}_T\right]\frac{\partial}{\partial\eta^\dagger}F(\eta^\dagger), \tag{3.29}$$

where $\delta = \delta_T(\tilde{x}_N) = 1$ and $r_c = r_T(\tilde{x}_N)$. Inserting these into (2.25) shows that

$$J_{r0} = -\frac{\sigma}{r_c}\int_0^\infty \frac{r\bar{T}}{(\bar{U}-c)^2}(\hat{\mathcal{G}}_{01}\hat{p}_0'\hat{p}_0 + \alpha^2\hat{\mathcal{G}}_{02}\hat{p}_0^2)[(r-r_c)\dot{\delta}_T/\delta_T + \dot{r}_T]\mathrm{d}r, \tag{3.30}$$

with the expressions for $\hat{\mathcal{G}}_{01}$ and $\hat{\mathcal{G}}_{02}$ being the same as in (6.35) of [I]. Through these calculations, the parameters characterising non-parallelism are all found as linear functions of $\dot{\delta}_T$.

In the present numerical investigation, we choose a self-similar velocity profile, for (3.22) and (3.23), as

$$f[\eta^\dagger(\tilde{x}, r)] = -(1 + q_c\,\mathrm{sech}^2\,\eta^\dagger)\tanh\eta^\dagger, \tag{3.31}$$

where q_c is a parameter measuring the influence of turbulence, which has to be assigned an experimental value.

As was pointed out by Cohen & Wygnanski (1987), this mean-flow velocity profile fits well with the measured profiles up to $x^*/D^* = 4$, where D^* is the dimensional diameter of the exhaust nozzle; within this axial region, the central velocity varies only moderately. The dimensional shear-layer momentum thickness Θ^* can be expressed as

$$\Theta^* = \mathscr{C}_1\delta_0^*\delta_T, \tag{3.32}$$

where $\mathscr{C}_1$ is a constant depending on the mean-flow profiles (see also (6.25) in [I])

$$\mathscr{C}_1 = \mathscr{C}_{m-t}\int_{\eta_a^\dagger}^\infty [\bar{T}(\eta^\dagger)]^{-1}[\bar{U}(\eta^\dagger) - \bar{U}_+][\bar{U}_a - \bar{U}(\eta^\dagger)]\,\mathrm{d}\eta^\dagger, \tag{3.33}$$

with $\mathscr{C}_{m-t} = (\bar{T}_+^{-1}\bar{U}_+^2 - \bar{T}_+^{-1}\bar{U}_+\bar{U}_a - \bar{T}_a^{-1}\bar{U}_+\bar{U}_a + \bar{T}_a^{-1}\bar{U}_a^2)^{-1}$. In the limit of $Ma \ll 1$ (incompressible) and $R_0 \gg \delta_T$ (quasi-dimensional), $\mathscr{C}_1 = \frac{1}{2}(1 - \frac{2}{3}q_c - \frac{2}{15}q_c^2)$ (Wu & Zhuang 2016). The constant factor $\mathscr{C}_1$ relates the shear-layer thickness δ_T to the *momentum thickness* Θ^*. Differentiating (3.32) with respect to the dimensional axial coordinate x^*, the parameter $\dot{\delta}_T$ is found as

$$\dot{\delta}_T = \mathscr{C}_1^{-1}R_T(\mathrm{d}\Theta^*/\mathrm{d}x^*), \tag{3.34}$$

in which $\mathrm{d}\Theta^*/\mathrm{d}x^*$ is measured experimentally.

https://doi.org/10.1017/jfm.2022.252 Published online by Cambridge University Press

4. Numerical solutions

4.1. *Numerical methods*

The core numerical work is to solve the strongly nonlinear evolution–modulation system (3.2) or its equivalent component-form (B1), subject to the self-consistent upstream and boundary conditions. The system is truncated in the region $-5 \leqslant \bar{x} \leqslant 25$ and $-\tilde{H} \leqslant \eta \leqslant \tilde{H}$, with step and mesh sizes $\Delta x = 0.001$ and $\Delta\eta = 0.005$, and transverse domain size $\tilde{H} = 60$. The Fourier series for $T_n^{(L)}$ and $Q_n^{(L)}$ consist of 15 harmonics, i.e. $0 \leqslant n \leqslant 15$ with 8 modes on each side ($-8 \leqslant L \leqslant 8$) in the present discrete-sideband case for each central-frequency component.

As in [I], the amplitude equation is marched downstream using a predictor–corrector scheme consisting of a three-step Adams explicit scheme and two-step implicit schemes for the predictor and the corrector, respectively. The equations for $T_n^{(L)}$ and $Q_n^{(L)}$ are discretised by the Crank–Nicolson scheme.

For a given mean-flow profile, it is necessary to solve the compressible Rayleigh equation numerically first to find the eigenvalue, the wavenumber α and its eigenfunction $\hat{p}_0$, after which the parameters in (3.2) and (3.27)–(3.28) can be evaluated. Among these, the integrands of J_{r1}, J_{r2} and J_{r0} consist of a singularity point at the critical level $r = r_c$, which is in the form of an up to fourth-order pole $(\bar{U} - c)^{-4} \sim (r - r_c)^{-4}$. These integrals must be interpreted as the Hadamard finite parts, which are defined according to the asymptotic behaviours of the integrands near the singular point.

4.2. *Numerical results of nonlinear evolution–modulation of ring-mode coherent structures*

As with planar free shear layers, detailed experimental data about nonlinear dynamics of CS on a circular jet are available only in the low-speed (incompressible) regime, for which quantitative comparisons between the theory and experiments are possible, and will be reported in separate paper. In the present paper, the calculations will be performed for circular jets in the compressible regime to reveal the qualitative dynamical behaviours of CS and the main features of the radiated acoustic field.

We choose a baseline case, termed 'case-$\mathcal{H}_R$', for which the parameters are the mean-flow parameter $q_c = 0.2$, the scaled shear-layer central position $r_c = 5$, the dimensionless average velocity $\bar{U}_R = 1.25$, the ratio of the upstream temperatures $\beta_T = 7/8$, the Mach number of the exhaust flow $Ma_J = 0.6$, the Haberman parameter $\bar{\lambda} = 0.005$, the spreading rate of the shear-layer thickness $\delta_T = 0.05$, the Prandtl number $Pr = 0.7$, the turbulent Prandtl number $Pr_T = 1$, and the specific heat ratio $\gamma = 1.4$. Other coefficients, which do not influence the dynamics of CS significantly, are given reasonable values: the initial amplitude of the disturbance $\epsilon = 0.09$; the phase lags $\hat{\theta}_1 = \hat{\theta}_2 = \pi/5$ (with $\hat{\theta}_i = \alpha c \hat{\tau}_i$; see [I]); the rescaled eddy conductivity and viscosity $\tilde{\lambda}_i = \bar{\lambda}_i$ $(i = 1, 2)$, with which the mathematical problem is well posed (see Wu & Zhuang (2016) and [I]); the deviation of the disturbance frequency from that of the neutral mode $\epsilon^{1/2} S_0 = -\alpha c/6$; the frequency difference for sidebands $\omega_\nu = 0.025\omega_0$; and the scaled turbulent Reynolds number $\sigma = 1$. Unless specifically declared, the parameters in other cases would remain the same as those in the baseline case. We will not carry out a parametric study of initial conditions since it has already been done in [I]. Presently, the seeded modes include the central mode with $(a_0, \varphi_0) = (1, 0)$, and the lower and upper sidebands with initial amplitudes and phases $(a_0^-, \varphi_0^-) = (0.18, -\pi/3)$ and $(a_0^+, \varphi_0^+) = (0.3, \pi/6)$, for all cases.

https://doi.org/10.1017/jfm.2022.252 Published online by Cambridge University Press

The strongly nonlinear theory can describe the most significant features of large-scale CS: roll-up of vorticity and modulation/saturation of the amplitude. Figures 2(*a*,*b*) show the formation of roller structures by displaying the rescaled critical-layer temperature T_c and vorticity Ω_c at several axial locations $\bar{x} = -2$, 0, 2 and 10, where T_c and Ω_c are defined as

$$\begin{aligned} T_c(\bar{\zeta},\tau,\bar{x},\eta) &= \frac{\bar{T}_c''}{2\alpha^2\bar{U}_c'^2}(\eta+S_0)^2 + \left(\frac{\bar{T}_{cM}'}{\alpha\bar{U}_c'} + \chi_1\bar{x}\right)(\eta+S_0) \\ &\quad + \sum_{n=-\infty}^{\infty} T_n(\tau,\bar{x},\eta)\exp(\mathrm{i}n(\bar{\zeta}-S_0\tau)) \\ &\quad + \left\{\left[\frac{\bar{T}_c''}{\bar{U}_c'} + (\gamma-1)\,Ma^2\bar{U}_c'\right]\frac{A(\bar{x})}{\alpha^2\bar{U}_c'}\exp(\mathrm{i}(\bar{\zeta}-S_0\tau)) + \mathrm{c.c.}\right\}, \end{aligned} \tag{4.1}$$

$$\begin{aligned} \Omega_c(\bar{\zeta},\tau,\bar{x},\eta) &= \frac{\bar{U}_c'''}{2\alpha^2\bar{U}_c'^2 p_Q}(\eta+S_0)^2 + \chi_2\bar{x}\,(\eta+S_0) \\ &\quad + \sum_{n=-\infty}^{\infty} Q_n(\tau,\bar{x},\eta)\exp(\mathrm{i}n(\bar{\zeta}-S_0\tau)) \\ &\quad + \left[\left(\alpha^2 + \frac{Ma^2\bar{U}_c'^2}{\bar{T}_c} - \frac{\bar{T}_c'}{\bar{T}_c}b_1 - j\right)\frac{A(\bar{x})}{\alpha^2\bar{U}_c' p_Q}\exp(\mathrm{i}(\bar{\zeta}-S_0\tau)) + \mathrm{c.c.}\right], \end{aligned} \tag{4.2}$$

which are the same as (6.43) and (6.44) in [I], respectively. Note that each of T_n, Q_n and A is a superposition of the central-frequency component and its sidebands. Figures 2(*a*,*b*) show T_c and Ω_c at a certain time $\tau = T/6$, where $T = 2\pi/\omega_v = \epsilon^{-1/2}2\pi/\Delta$ is the long period, over which the CS modulates periodically. In order to monitor the wavepacket, we examine $\tilde{u}_c = \tilde{u}_1(\tau,\bar{x},\eta=0,\bar{\zeta})$, the axial velocity of the CS at a certain level $\eta = 0$, with

$$\tilde{u}_1(\tau,\bar{x},\eta,\bar{\zeta}) = \sum_{n=-\infty}^{\infty}\sum_{L=-\infty}^{\infty}\tilde{u}_1^{\langle n\rangle(L)}(\bar{x},\eta)\exp(\mathrm{i}n(\bar{\zeta}-S_0\tau) - \mathrm{i}L\Delta\tau), \tag{4.3}$$

where

$$\tilde{u}_1^{\langle 0\rangle(L)}(\bar{x},\eta) = \epsilon^{3/2}\frac{p_Q}{\alpha\bar{U}_c'}\int_{-\infty}^{\eta} Q_0^{(L)}(\bar{x},\eta^\star)\,\mathrm{d}\eta^\star, \tag{4.4}$$

$$\tilde{u}_1^{\langle n\rangle(L)}(\bar{x},\eta) = \epsilon^{3/2}\left[\frac{p_Q}{\alpha\bar{U}_c'}\int_{-\infty}^{\eta} Q_n^{(L)}\,\mathrm{d}\eta^\star + \hat{u}_1^{\langle n\rangle-}\Big|^{(L)}\right] \quad (n=2,3,\ldots), \tag{4.5}$$

$$\begin{aligned} \tilde{u}_1^{\langle 1\rangle(L)}(\bar{x},\eta) &= -\frac{\epsilon b_1}{\alpha^2\bar{U}_c'}A^{(L)} + \epsilon^{3/2}\frac{p_Q}{\alpha\bar{U}_c'}\left[\left(\mathrm{i}\frac{\partial}{\partial\bar{x}} + L\Delta + S_0 + \chi_2\bar{x}\right)A^{(L)}\ln\frac{\epsilon^{1/2}}{\alpha|\bar{U}_c'|}\right] \\ &\quad + \epsilon^{3/2}\frac{p_Q}{\alpha\bar{U}_c'}\lim_{\tilde{H}\to\infty}\left[\left(\mathrm{i}\frac{\partial}{\partial\bar{x}} + L\Delta + S_0 + \chi_2\bar{x}\right)A^{(L)}\ln|\tilde{H}| + \int_{-\tilde{H}}^{\eta} Q_1^{(L)}\,\mathrm{d}\eta^\star\right] \\ &\quad + \epsilon^{3/2}\left[\left(\alpha^2 + \frac{\bar{U}_c'''}{\bar{U}_c'} - \frac{\bar{T}_c''}{\bar{T}_c} + \frac{Ma^2\bar{U}_c'^2}{\bar{T}_c}\right)\frac{(\eta+S_0)}{\alpha^2\bar{U}_c'}A^{(L)} + \hat{u}_1^{\langle 1\rangle-}\Big|^{(L)}\right]. \end{aligned} \tag{4.6}$$

https://doi.org/10.1017/jfm.2022.252 Published online by Cambridge University Press

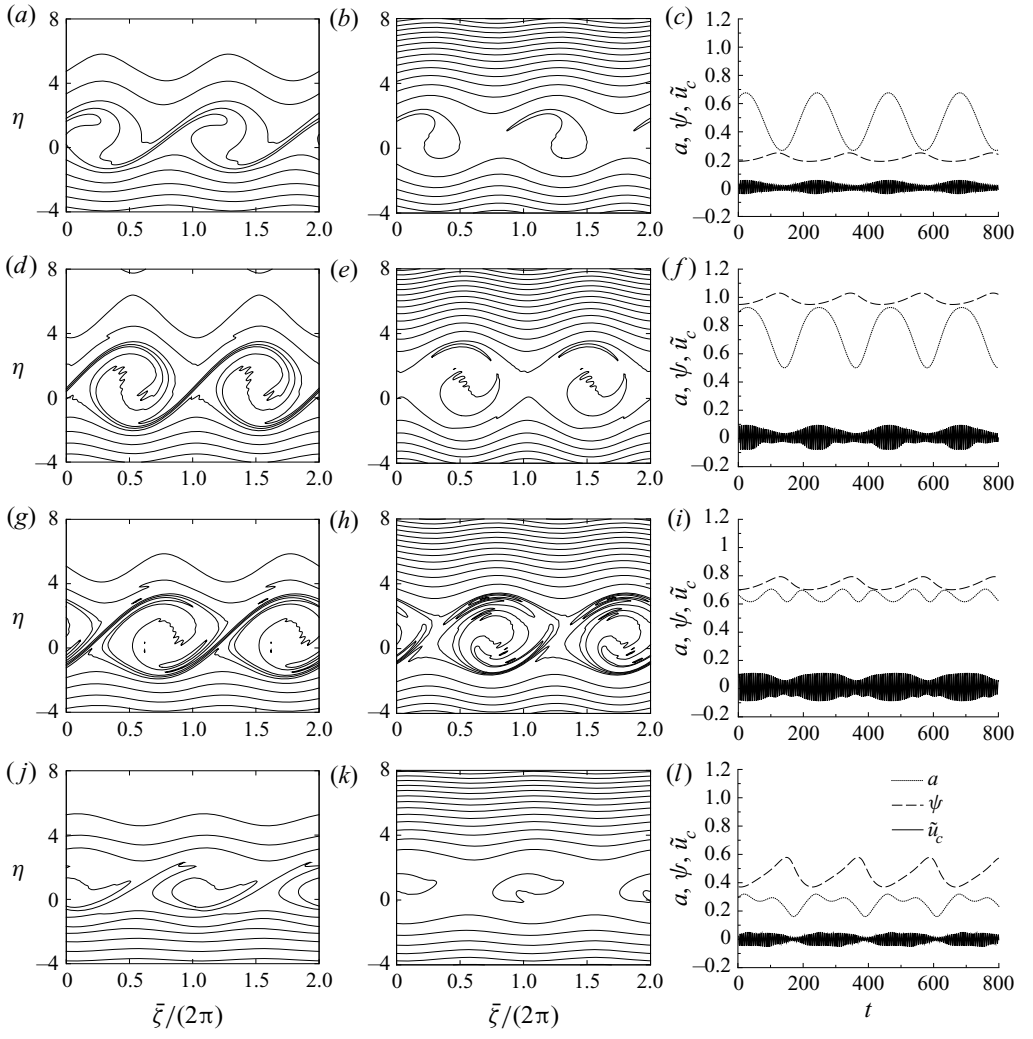


Figure 2. Contours of the scaled critical-layer temperature (*a*,*d*,*g*,*j*), vorticity (*b*,*e*,*h*,*k*), and modulated time trace of wavepackets (*c*,*f*,*i*,*l*), at four axial positions $\bar{x} = -2$ (*a–c*), $\bar{x} = 0$ (*d–f*), $\bar{x} = 2$ (*g–i*) and $\bar{x} = 10$ (*j–l*) in case-$\mathcal{H}_R$.

The time sequence of $\tilde{u}_c$ at the four axial locations is displayed in figures 2(*c*,*f*,*i*,*l*). The complex amplitude of the CS, $\tilde{A}$, can be rewritten as

$$\tilde{A}(\tau,\bar{x}) = \sum_{L=-\infty}^{\infty} A^{(L)}(\bar{x})\exp(-\mathrm{i}L\Delta\tau - \mathrm{i}S_0\tau) \overset{\text{def.}}{=\!=} a(\tau,\bar{x})\exp(\mathrm{i}2\pi\,\psi(\tau,\bar{x})), \qquad (4.7)$$

to introduce the 'amplitude' a and 'phase' $2\pi\psi$. The amplitude–phase modulation is also shown. The wavepacket envelope of the CS displays modulation with the long time scale $2\pi/\omega_v$, and is composed of the difference frequency component and its 'harmonics'. These low-frequency components will be shown to be as the physical acoustic source for emitting low-frequency sound waves.

https://doi.org/10.1017/jfm.2022.252 Published online by Cambridge University Press

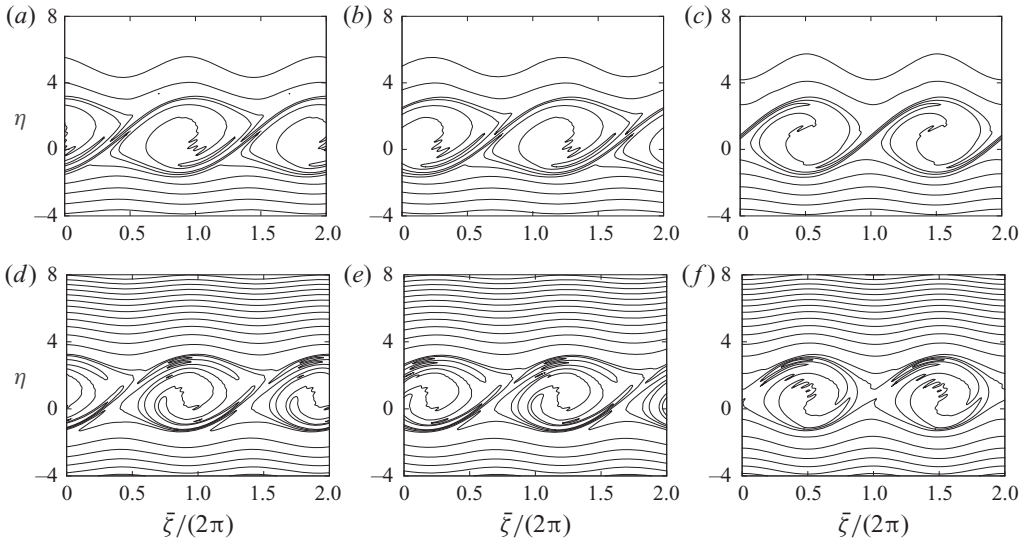


Figure 3. Contours of the scaled critical-layer temperature (*a–c*) and vorticity (*d–f*) at the axial position $\bar{x} = 3$ and three phases, $\tau = 0$ (*a*,*d*), $\tau = T/3$ (*b*,*e*) and $\tau = 2T/3$ (*c*,*f*) within a period in case-$\mathcal{H}_R$.

At $\bar{x} = -2$, the amplitude of the CS is fairly small so the evolution is essentially linear. The contours exhibit simple patterns; a large-scale vortex structure is discernable, but the vorticity or temperature field has not rolled up yet. The wavepacket is regular, with its envelope and phase undergoing simple harmonic oscillations. Downstream of $\bar{x} = 0$, the neutral position, the contours have rolled up and complete CS, with a clear braid structure, appear. The amplitude of the wavepacket envelope is enhanced. Spectrally, higher-order harmonics are all excited, which is the key characteristic of strong nonlinearity. At $\bar{x} = 2$, the roller structures maintain a nearly constant amplitude, which is evidence of nonlinear saturation. Meanwhile, the CS start to be elongated, and there appear 'small-scale' structures, which may signal the beginning of break-up. The phase and amplitude of the wavepacket deviation are obvious from the harmonic oscillations. At $\bar{x} = 10$, the ordered CS nearly disappear. Interestingly, the amplitude–phase modulation tends to be even more irregular with respect to the long time scale.

The CS are simultaneously modulated in time, as is shown in figure 3, which displays the fields of T_c and Ω_c at a fixed axial position $\bar{x} = 3$ but at different instants $\tau = 0$, $T/3$ and $2T/3$ within a period. The CS change shape and intensity appreciably.

Figure 4 shows the development of the fundamental as well as the excitation and evolution of its sidebands. Three initial modes are seeded upstream, following which other sideband modes are excited by nonlinear interactions, and their amplitudes increase quickly. In other words, the spectrum broadens around the fundamental frequency. The lower-sideband modes, i.e. the components with $L < 0$, have larger growth rates than those of the upper-sideband modes with $L > 0$, in the linear region. Due to the nonlinear interactions, the amplitudes of lower sidebands would exceed those of the upper ones, displaying an energy back-scattering phenomenon; see also Wu & Tian (2012) and [I].

Figure 5 shows the generation and evolution of the first harmonic and its sidebands, which are excited due to nonlinearity. Similar to the fundamental and its sidebands, sideband modes around the harmonic also appear and reach a considerable level.

https://doi.org/10.1017/jfm.2022.252 Published online by Cambridge University Press

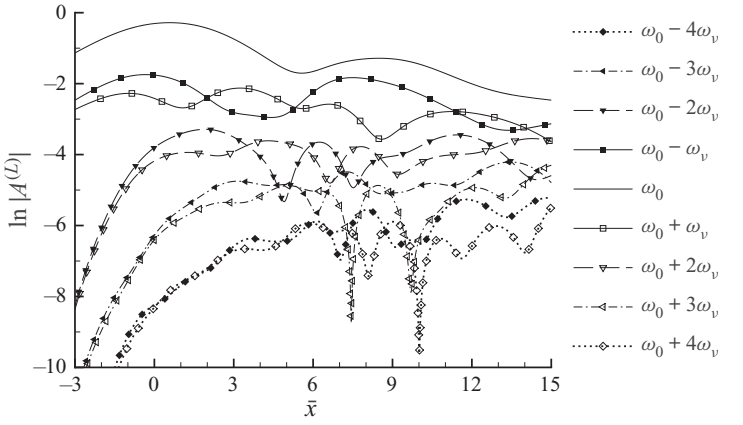


Figure 4. The development of $A^{(L)}$, the amplitudes of the fundamental and its sideband components with frequencies $\omega_0 \pm L\omega_\nu$ $(L = 0, 1, \ldots, 5)$ in case-$\mathcal{H}_R$.

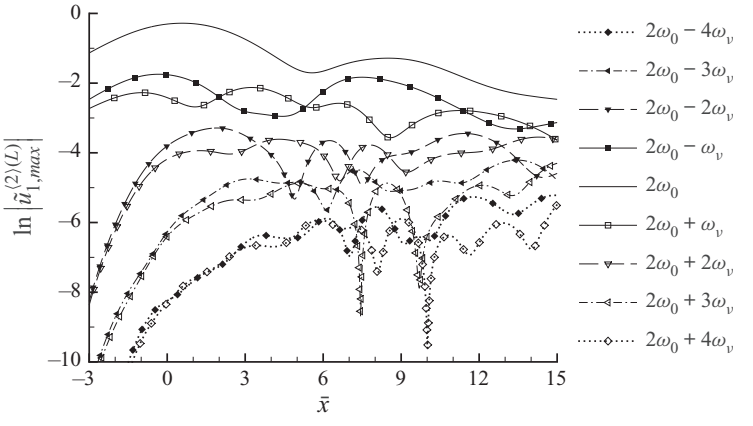


Figure 5. The development of the maximum axial velocities of the first harmonic and its sideband components $\tilde{u}_1^{\langle 2\rangle(L)}$ with frequencies $2\omega_0 + L\omega_\nu$ $(L = 0, \pm1, \pm2, \pm3)$ in case-$\mathcal{H}_R$.

Energy back-scattering and spectrum broadening take place, namely, the energy spreads to their sidebands around each central-frequency component, especially to lower sidebands.

A significant phenomenon observed in a planar free shear layer (e.g. Miksad 1973) is that there exists a large-amplitude component with the difference frequency ω_ν. This feature also occurs in a circular jet, as is shown in figure 6, where the development of the mean-flow-distortion components is plotted. Different from the sidebands around the fundamental mode and its harmonics, the low-frequency components, which stand as sidebands around the zero-frequency component ($n = 0$, $L = 0$), vary with respect to the slow time and slow axial variables τ and $\bar{x}$, respectively. It should be emphasised again that it is the slowly varying components that radiate low-frequency sound waves. An important feature is that the difference frequency components as well as certain sideband components of the fundamental and harmonics exhibit jittering, as a result of which the acoustic radiation at these frequencies would be enhanced.

Now we examine the transverse distributions of the first harmonic and the mean-flow distortion together with their sidebands. Figure 7 shows the profiles of the sidebands of the

https://doi.org/10.1017/jfm.2022.252 Published online by Cambridge University Press

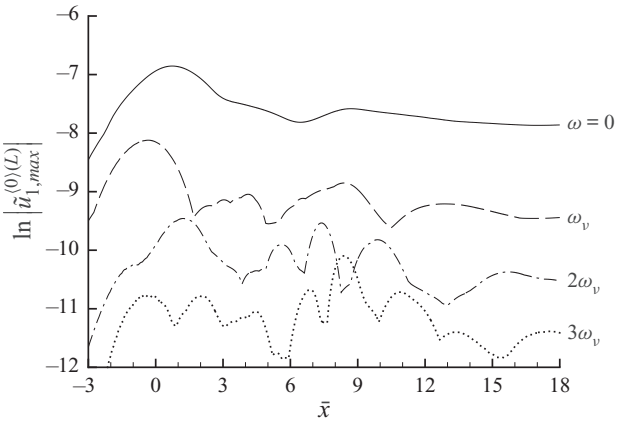


Figure 6. The development of the maximum axial velocities $\tilde{u}_1^{\langle 0\rangle(0)}$ measuring the mean-flow distortion and its sidebands with frequencies $L\omega_v$ ($L = 0, 1, 2, 3$) in case-$\mathcal{H}_R$.

first harmonic and the low-frequency components at three axial positions $\bar{x} = -2$, 0 and 5. At $\bar{x} = -2$, where the CS start to roll up (see figure 2), the first harmonic, together with its sidebands, and the mean-flow distortion, together with their low-frequency components, are all relatively small. At the neutral position, $\bar{x} = 0$, the amplitudes of the zero-frequency and first harmonic are larger than those at the previous station. Downstream at $\bar{x} = 5$, the harmonics and low-frequency components have attenuated markedly, but the mean-flow-distortion term ($n = 0$, $L = 0$) remains at a considerable level. The CS cannot maintain shape, so the roller structure would eventually disappear. Though not shown here, the features for higher harmonics are similar to those of the first harmonic as analysed above.

In order to probe into the spectrum of the CS, we consider the maximum value of a radial profile of $\tilde{u}_1^{\langle n\rangle(L)}$, which measures the strength of the component at that frequency. Figure 8 shows the spectra at five axial positions $\bar{x} = -2$, 0, 2, 5 and 10. At $\bar{x} = -2$, the spectrum is rather sharp, with the energy concentrating in the seeded central-frequency component ($L = 0$) at each order. At the neutral position $\bar{x} = 0$ and downstream locations, the sidebands around the fundamental, the harmonics and the mean-flow distortion are excited. The spectrum broadens as the CS evolve downstream.

Parametric studies have been performed in [I] for the planar case, including the effects of non-parallelism, compressibility Ma, the temperature ratio β_T, viscosity Re, or $\bar{\lambda}$, and so on. The present ring-mode CS in an axisymmetric jet are quite similar to the two-dimensional CS in a planar shear layer, except for the additional circularity effect measured by r_c^{-1}. We would only examine this effect here. Figure 9 shows the variation with r_c of the neutral-mode frequency $\omega_N \equiv \alpha c$ for different Mach numbers and q_c. The non-dimensional frequency ω_N increases with r_c but remains $O(1)$. As $r_c \to \infty$, ω_N approaches a constant, the planar limit, which is reached practically when $r_c = 5$. In the near-nozzle region, the local shear-layer thickness is $0.03D^*$ in typical experiments, and it follows that the frequencies normalised by D^* would be in the range 30–45, and correspondingly the Strouhal numbers based on D^* are in the range 5–7. Figure 10 shows the amplitude evolution of CS for $r_c = 2, 5, 10$ and two upstream temperature ratios $\beta_T = 1$ and $7/8$. The two cases with the different β_T exhibit similar evolution trends as r_c is varied. Circularity exerts little influence in the linear stage but suppresses appreciably the

https://doi.org/10.1017/jfm.2022.252 Published online by Cambridge University Press

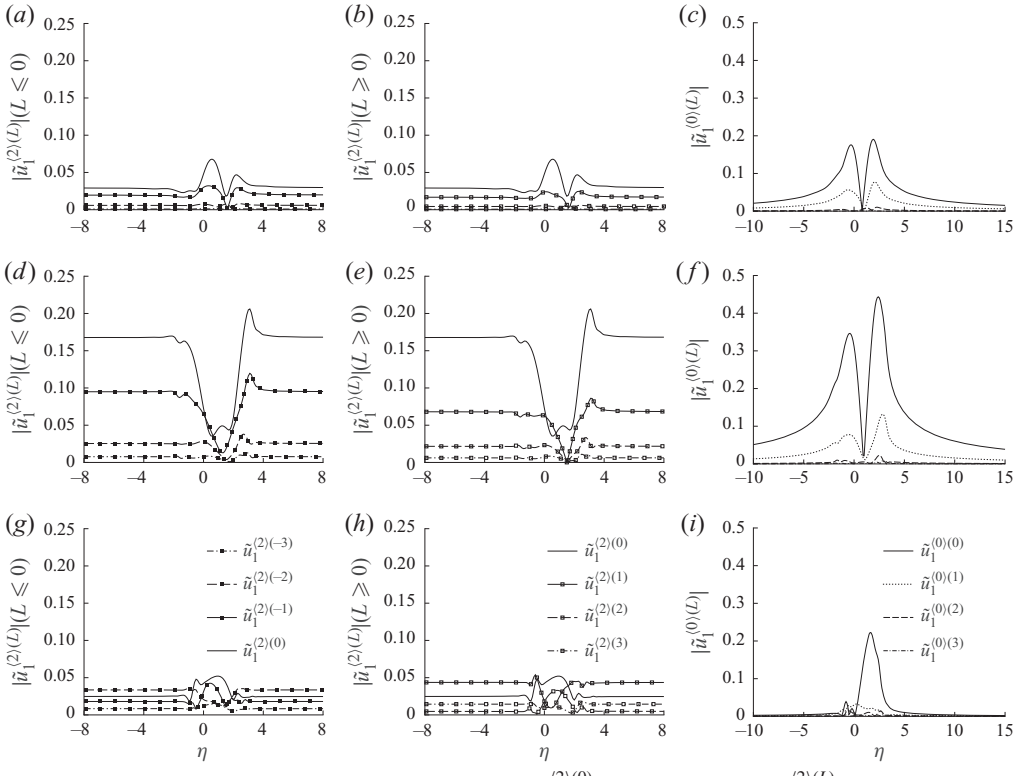


Figure 7. The radial distributions of the first harmonic $\tilde{u}_1^{\langle 2\rangle(0)}$ and its sidebands $\tilde{u}_1^{\langle 2\rangle(L)}$ ($L = \pm 1, \pm 2, \pm 3$) (*a*,*b*,*d*,*e*,*g*,*h*), and the mean-flow distortion $\tilde{u}_1^{\langle 0\rangle(0)}$ and low-frequency sidebands $\tilde{u}_1^{\langle 0\rangle(L)}$ ($L = 1, 2, 3$) (*c*,*f*,*i*) at three axial positions: $\bar{x} = -2$ (*a*–*c*), $\bar{x} = 0$ (*d*–*f*), and $\bar{x} = 5$ (*g*–*i*) in case-$\mathcal{H}_R$.

amplitude of the CS in the nonlinear regime. Theoretically, not only the Rayleigh problem, (2.13) and (2.20), but also the nonlinear evolution–modulation system, (3.2), approaches the planar limit as $r_c^{-1} \to 0$.

4.3. *Numerical results of acoustic radiation by ring-mode coherent structures*

The acoustic radiation of the baseline case is shown in figure 11. Figure 11(*a*) shows the directivity $\mathscr{D}^{(L)}$ of different frequencies $\omega = L\omega_\nu$ as well as the directivity of the overall acoustic field. The sound waves of different frequencies are somewhat different in their directivity and intensity. As the source is non-compact, a strict multipolar interpretation of acoustic field is not applicable. Nevertheless, the directivity of the lowest-frequency component behaves like a monopole, while higher ones (e.g. $4\omega_\nu$) become somewhat like dipoles. It should be emphasised that the latter components are still within sidebands of the mean-flow distortion, representing 'low-frequency sound waves'. Figure 11(*b*) shows the spectrum in different radiating directions $\bar{\varphi} = n\pi/4$ ($n = 0$–4). The lowest-frequency component is the most significant part in each case, especially in the downstream directions ($0 \leqslant \bar{\varphi} \leqslant \pi/2$), so it defines the overall directivity of the acoustic field.

While the nonlinear dynamics of the CS are rather similar in the circular jet and planar mixing layer, the directivity of jet noise turns out to be significantly different in these flows. As is shown in [I], the directivity in the planar case exhibits cusps in the upstream radiating directions. The sound generated in the present case does not have this feature

https://doi.org/10.1017/jfm.2022.252 Published online by Cambridge University Press

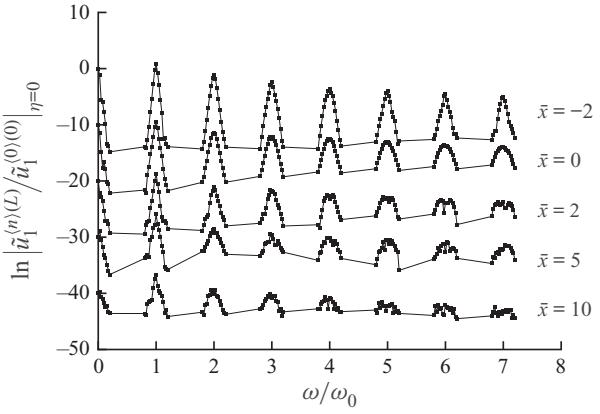


Figure 8. Spectrum of the CS, measured by axial velocity at the critical level, at positions $\bar{x} = -2$, 0, 2, 5 and 10 in case-$\mathcal{H}_R$. Note that the curves have been moved 10, 20, 30, 40 units down for $\bar{x} = 0$, 2, 5, 10, respectively.

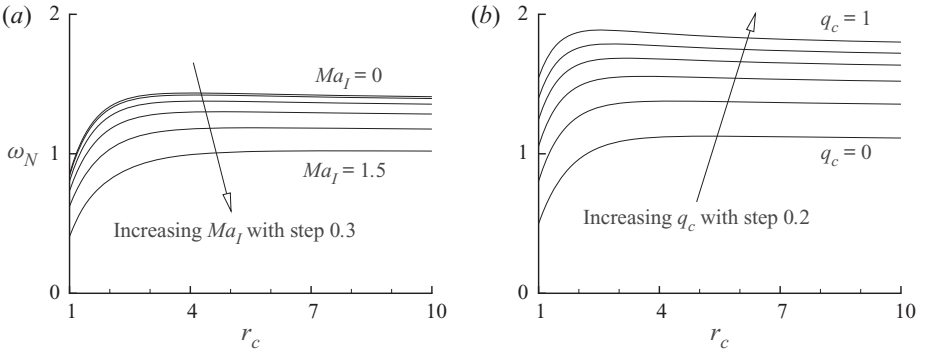


Figure 9. Variation of the neutral-mode frequency $\omega_N \equiv \alpha c$ with r_c: (*a*) $q_c = 0.2$; (*b*) $Ma_I = 0.6$. Other parameters are fixed at $\beta_T = 7/8$ and $\bar{U}_R = 1.25$.

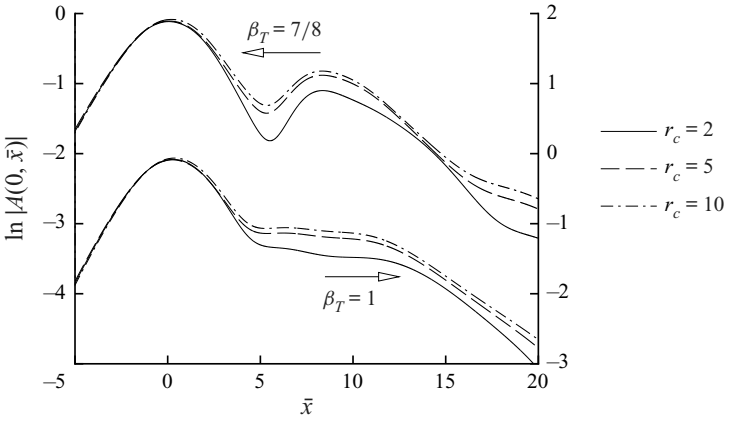


Figure 10. Amplitude evolution of the CS for $r_c = 2$, 5, 10 and two temperature ratios, $\beta_T = 7/8$ and $\beta_T = 1$, at time $\tau = 0$.

https://doi.org/10.1017/jfm.2022.252 Published online by Cambridge University Press

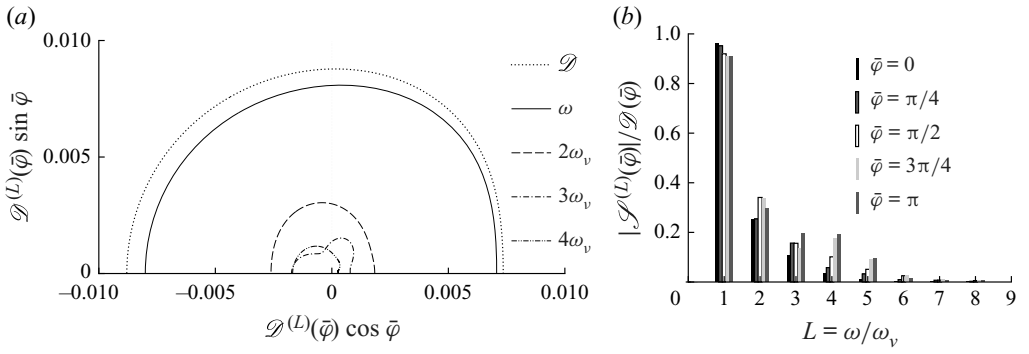


Figure 11. The acoustic field radiated from modulated CS with discrete sidebands in case-$\mathcal{H}_R$. (*a*) Directivity of the sound wave emitted by each low-frequency sideband with $\omega = L\omega_v$ ($L = 1$–4); the directivity of the overall acoustic field is also shown. (*b*) The spectrum in radiating directions $\bar{\varphi} = n\pi/4$ ($n = 0$–4).

because of the absence of an 'inner' sound field. Things would change in the near-nozzle region of the jet, where an inner sound field would appear. Furthermore, in that region there exist not only the ring-mode CS but also helical-mode CS with different azimuthal wavenumbers, and as these modes have similar growth rates and amplitudes, they would interact with each other nonlinearly. The theory for this case is being developed.

Calculations are carried out for different Ma_I and $\bar{\lambda}$. The directivity and spectrum are displayed in figure 12. The strength of the acoustic field increases with Ma_I. When Ma_I is very small, the flow is nearly incompressible, and its radiation is weak and takes on the characteristics of a monopole. The comparison between the cases with different $\bar{\lambda}$ shows that viscosity has little influence on the directivity, but components with relatively high frequencies $\geqslant 4\omega_v$ are somewhat more pronounced when viscosity is smaller.

Figure 13 shows the directivity and spectrum of the acoustic radiation for different velocity ratios $\beta_U = 1 - 2/(\bar{U}_R + 1)$ and two temperature ratios ($\beta_T = 7/8, 1$). The smallest value of $\bar{U}_R$ is 1, representing the case without coflow. For both $\beta_T = 7/8$ and $\beta_T = 1$, $\mathscr{D}$ increases appreciably with the $\bar{U}_R$, while the directivity shifts to upstream directions $\pi/2 \leqslant \bar{\varphi} < \pi$. For $\beta_T = 7/8$, a hot jet, the spectrum indicates that the $3\omega_v$, $4\omega_v$, $5\omega_v$ components are stronger in the side direction ($\bar{\varphi} = \pi/2$) than in the downstream direction ($\bar{\varphi} = 0$), a feature that is, however, not shared by the case $\beta_T = 1$. Focusing on the radiation downstream, we note that the sound is weaker in the case $\beta_T = 1$ than that with $\beta_T = 7/8$. A close examination attributes the increase of $\mathscr{D}$ with $\bar{U}_R$ to the fact that the 'refraction factor', $|\kappa_s^2 \mathscr{D}_p|$ in (2.74), turns out to increase with $\bar{U}_R$ more significantly than the reduction of the equivalent source $|\widehat{a_M^+}|$. It should be noted that a larger $\mathscr{D}$ does not necessarily mean louder noise since the reference quantities for the non-dimensionalised pressure in cases with different $\bar{U}_R$ are different; see (2.1*a–d*) and (2.2). With the normalisation factor of the pressure being taken into account, $\mathscr{D}(\bar{\varphi})[2/(1+\bar{U}_R)]^2$ measures the *radiation efficiency*. Although not shown, this is found to be more-or-less independent of $\bar{U}_R$. Since a higher $\bar{U}_R$ corresponds to a weaker shear, the amplification and hence the amplitude of CS are reduced, leading to reduced radiation of low-frequency sound waves, consistent with experimental measurements (e.g. Tanna & Morris 1977).

The directivity and spectrum of the sound generated by modulated CS for different r_c and two values of Ma_I are shown in figure 14. The strength of radiation increases with r_c, but the directivity remains more or less unchanged. Mathematically, the generated

https://doi.org/10.1017/jfm.2022.252 Published online by Cambridge University Press

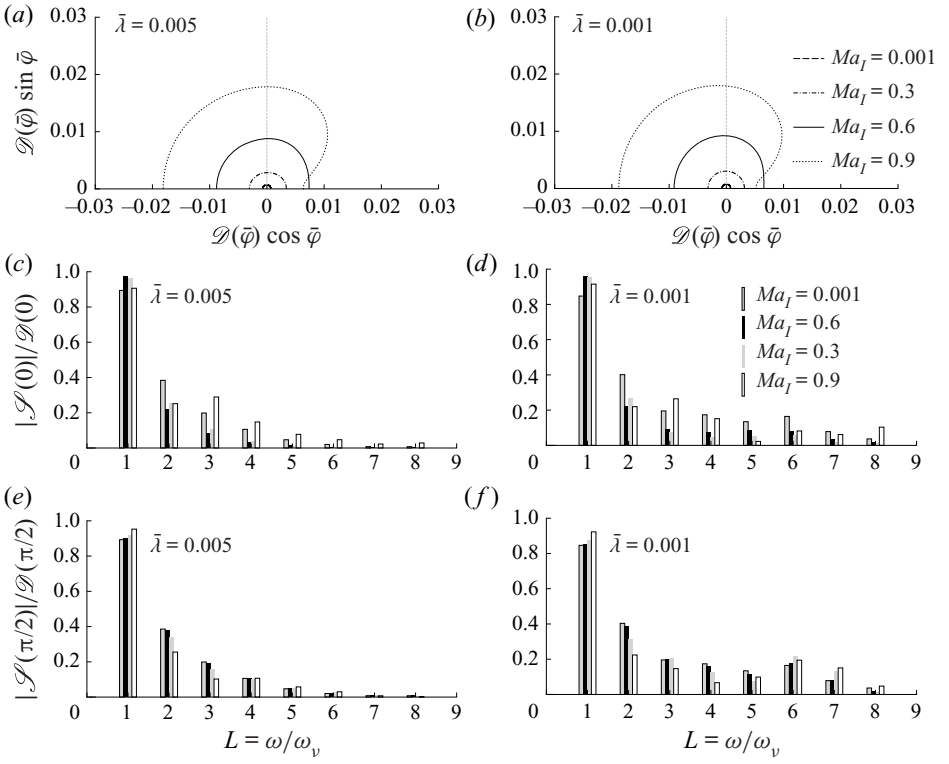


Figure 12. The acoustic field radiated from modulated CS with discrete sidebands for different Ma_I and two values of the scaled viscosity parameter $\bar{\lambda}$: (*a*,*b*) directivity; (*c*–*f*) the spectrum in two radiating directions, $\bar{\varphi} = 0$ and $\pi/2$.

sound field is of $O(\epsilon^3 r_c)$ when $1 \ll r_c \ll \epsilon^{-1/2}$, as can be inferred by inspecting (2.60) and (2.57), in which $\hat{\mathcal{I}}_R$ remains as (2.41) except that $r = r_c + y$ in the integrand may be approximated by r_c. The estimate of an $O(\epsilon^3 r_c)$ acoustic field could alternatively be derived by considering a 'circularity deck' corresponding to $\breve{r} = r/r_c = O(1)$, but this is not pursued here. However, the sound cannot become louder without limit as $r_c \to \infty$ because once r_c is comparable with $O(\epsilon^{-1/2})$, there would appear an inner sound field, which also influences the radiation outside. In those cases, the acoustic perturbations are always $O(\epsilon^{5/2})$, as was derived in [I]. The present theory for radiation breaks down when $r_c = O(\epsilon^{-1/2})$, which is also a motivation towards constructing a unified or composite theory for any r_c in future investigations.

Another relevant factor is the frequency difference of the seeded modes, which is measured by ω_v/ω_0. Here we test several cases with $\omega_v/\omega_0 = 0.0125$, 0.025, 0.05 and 0.075 for $r_c = 5$ and 10, and the results are shown in figure 15. Because the radiation strength differs significantly, the directivity is rescaled for each case by $\mathscr{D}(\pi/2)$, whose values are listed in table 1. When ω_v/ω_0 is very small, the CS behave like single-frequency perturbations, the radiation of which is quite weak. As ω_v/ω_0 is increased, the radiation intensifies considerably. For sufficiently large ω_v/ω_0 (0.05 and 0.075), the loudest component shifts to a higher frequency, about $0.3\omega_0$, as is displayed in figures 15(*c*–*f*). Note that as we plot the spectrum against L, the bars with the same L denote different

https://doi.org/10.1017/jfm.2022.252 Published online by Cambridge University Press

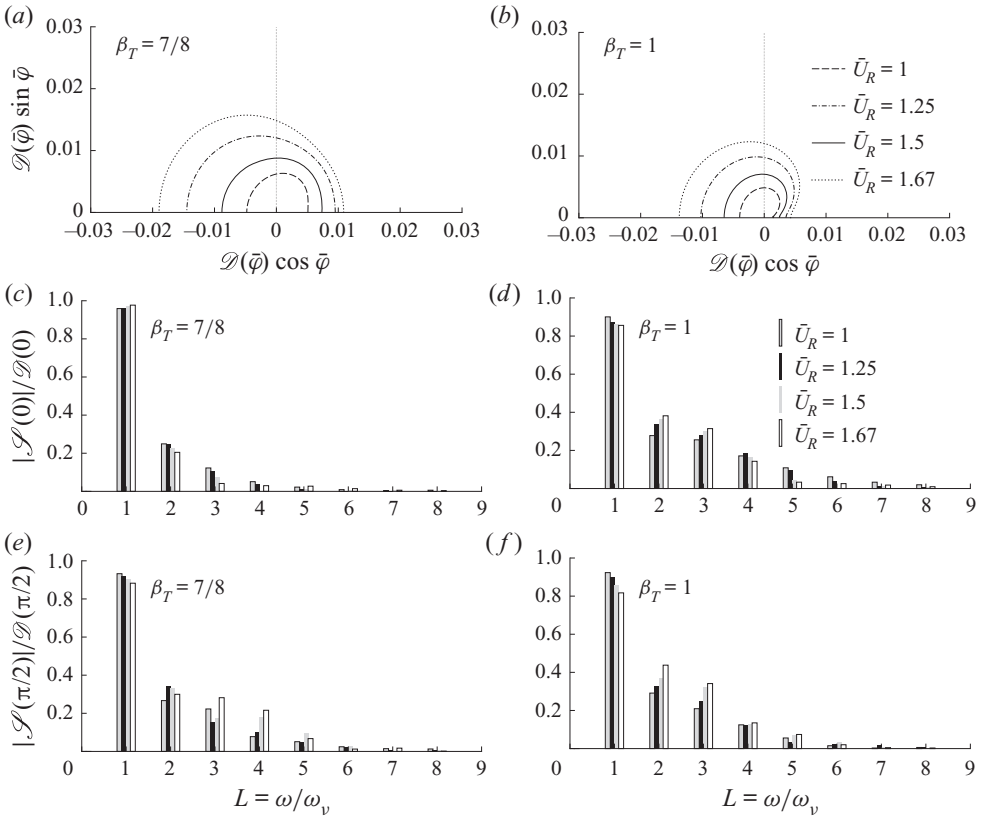


Figure 13. The acoustic field radiated from modulated CS with discrete sidebands for different $\bar{U}_R$ and two values of β_T: (*a*,*b*) directivity; (*c*–*f*) spectrum in two radiating directions, $\bar{\varphi} = 0$ and $\pi/2$.

ω_v/ω_0	0.0125	0.025	0.05	0.075
$r_c = 5$	1.016×10^{-3}	8.778×10^{-3}	1.189×10^{-1}	1.547×10^{1}
$r_c = 10$	1.990×10^{-3}	1.736×10^{-2}	1.783×10^{-1}	2.576×10^{1}

Table 1. Values of the directivity function $\mathscr{D}(\pi/2)$ for different ω_v/ω_0; these values are used to normalise $\mathscr{D}(\bar{\varphi})$ in figures 15(*a*,*b*).

physical frequencies. For cases with the same ω_v/ω_0, the radiation strength increases with r_c, consistent with what figures 14(*a*,*b*) show.

Finally, we consider nonlinear evolution and acoustic radiation of CS represented by wavepackets with a continuum of sidebands, for which the spectrum of the amplitude, $\hat{A}(\omega, \bar{x})$, is a continuous function of ω. Instead of (3.11) for discrete-sideband cases, the upstream condition is specified for the amplitude spectrum in the form

$$\hat{A}(\omega, \bar{x}) \to \hat{A}_0(\omega)\exp(\sigma_s \bar{x}^2/2 + \mathrm{i}\omega\bar{x}/c_g) \quad \text{as } \bar{x} \to -\infty, \tag{4.8}$$

where the initial spectrum $\hat{A}_0$ is Gaussian,

$$\hat{A}_0(\omega) = (d\sqrt{2\pi})^{-1}\exp[-\omega^2/(2d^2)], \tag{4.9}$$

https://doi.org/10.1017/jfm.2022.252 Published online by Cambridge University Press

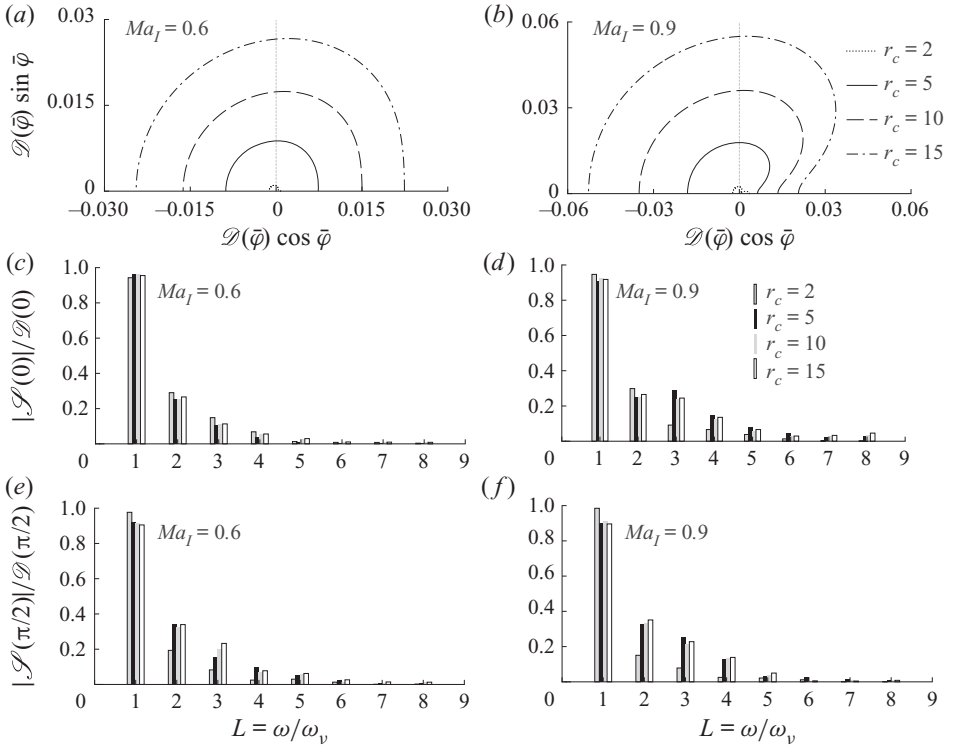


Figure 14. The acoustic field radiated from modulated CS with discrete sidebands for different r_c at $Ma_I = 0.6$ (*a*,*c*,*e*), and $Ma_I = 0.9$ (*b*,*d*,*f*): (*a*,*b*) directivity; (*c*–*f*) spectrum in two radiating directions, $\bar{\varphi} = 0$ and $\pi/2$.

with d measuring the frequency bandwidth of the sideband. For the upstream and boundary conditions for $\tilde{T}$ and $\tilde{Q}$, the reader is referred to § 4.4.2 in [I].

In our numerical computations, we used 65 sample points ($-32 \leqslant L \leqslant 32$) to discretise the spectrum in the range $-\frac{1}{2}\omega_0 < \omega < \frac{1}{2}\omega_0$. The nonlinear behaviours, including roll-up and amplitude modulation, are similar to those in discrete-sideband cases and hence are not shown here. Figure 16 shows the spectrum of the axial velocity at the critical level at four positions, $\bar{x} = 0$, 5, 10 and 15, for two bandwidths, $6d = 0.375\omega_0$ and $0.5\omega_0$. The spectrum features peaks at zero and the fundamental and harmonic frequencies, plus the sidebands around them. The latter broaden gradually, with the peaks becoming less as sharp as the CS evolve downstream.

Calculations of the acoustic radiation are performed for $6d/\omega_0 = 0.125$, 0.25, 0.375 and 0.5, and two values of r_c, 5 and 10, with the Haberman parameter $\bar{\lambda} = 0.02$. The directivity and spectrum of the sound field are shown in figure 17. Again, since the strength of radiation is very different, the directivity has also been rescaled for each case by its own $\mathscr{D}(\pi/2)$, the values of which are listed in table 2. The data indicate that the radiation becomes stronger with the bandwidth and r_c, and the directivity of the overall acoustic field is akin to that of a monopole, similar to discrete-sideband cases. The far-field acoustic spectrum in two radiating directions is shown in figures 17(*c*–*f*), in which the Strouhal number is introduced as

$$St = \epsilon^{1/2}\delta_0^* f^*/U_0^* = \epsilon^{1/2}\omega/(2\pi), \tag{4.10}$$

https://doi.org/10.1017/jfm.2022.252 Published online by Cambridge University Press

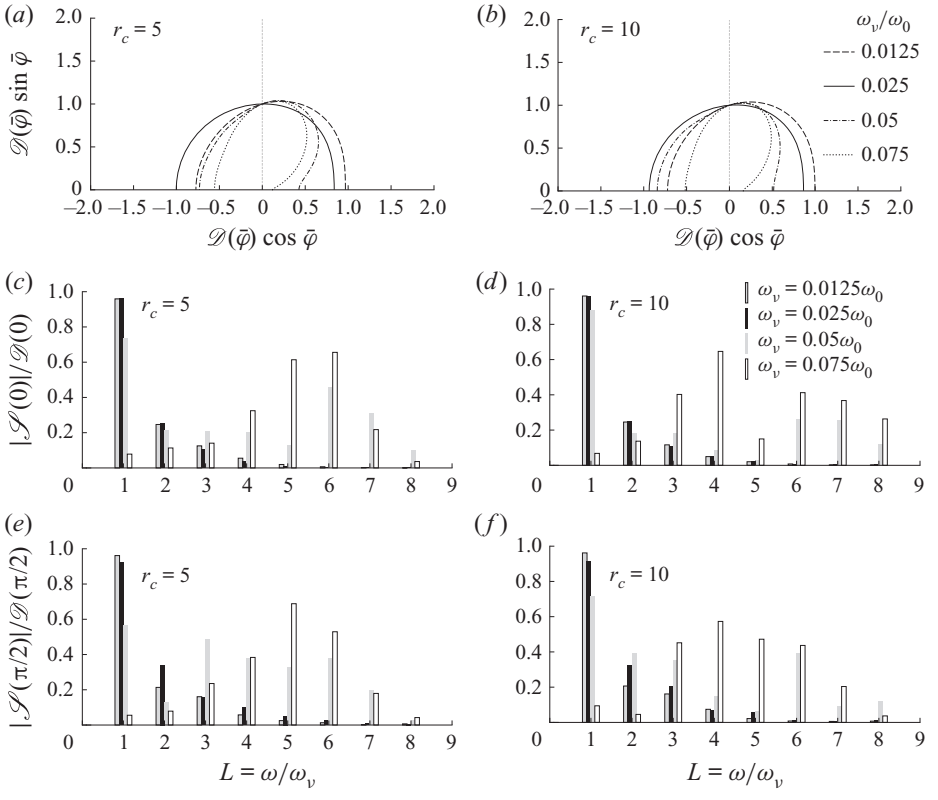


Figure 15. The acoustic field radiated from modulated CS with discrete sidebands for $r_c = 5$ (*a*,*c*,*e*), and $r_c = 10$ (*b*,*d*,*f*). For each r_c difference frequency, $\omega_v/\omega_0 = 0.0125$, 0.025, 0.05 and 0.07 are considered: (*a*,*b*) directivity; (*c*–*f*) spectrum in two radiating directions, $\bar{\varphi} = 0$ and $\pi/2$.

with $\epsilon^{1/2}f^*$ being the physical frequency in Hertz (Hz) of the radiated low-frequency sound waves. The frequency band of the acoustic field increases with that of the amplitude spectrum. When $6d = 0.5\omega_0$, the acoustic field spectrum extends to $St = 0 \sim 0.04$, while the fundamental waves of the CS are centred at the Strouhal numbers $\omega_0/(2\pi) \approx 0.1822$ and 0.1798 for $r_c = 5$ and 10, respectively. Following the practice in experiments, we may introduce the Strouhal number St_D based on the nozzle diameter D^* and jet exit velocity U_j^*, as $St_D = \epsilon^{1/2}f^*D^*/U_j^*$. It follows that St_D is related to St via

$$St_D = D^*/(2\delta_0^*)(1 - \beta_U)\, St. \tag{4.11}$$

Since $D^*/(2\delta_0^*) \approx r_c$ for $r_c = 5$ and 10, in terms of St_D, the acoustic field spectrum extends approximately to $St_D = 0.18$ and 0.36, which makes up a substantial portion of overall jet mixing noise, and in the latter contains the peak radiation frequency ($St_D \approx 0.2$) (Tam *et al.* 2008; Viswanathan 2008; Brès *et al.* 2016). The high-frequency components are more pronounced in the radiating direction $\bar{\varphi} = \pi/2$ than those with $\bar{\varphi} = 0$.

Although a definitive quantitative comparison between the theory and experiments is not possible at this stage, it is interesting to note that for all the cases, whether the CS consist of discrete or continuous sidebands, the directivity predicted resembles the measurement shown in figure 21(*a*) of Zaman (1985).

https://doi.org/10.1017/jfm.2022.252 Published online by Cambridge University Press

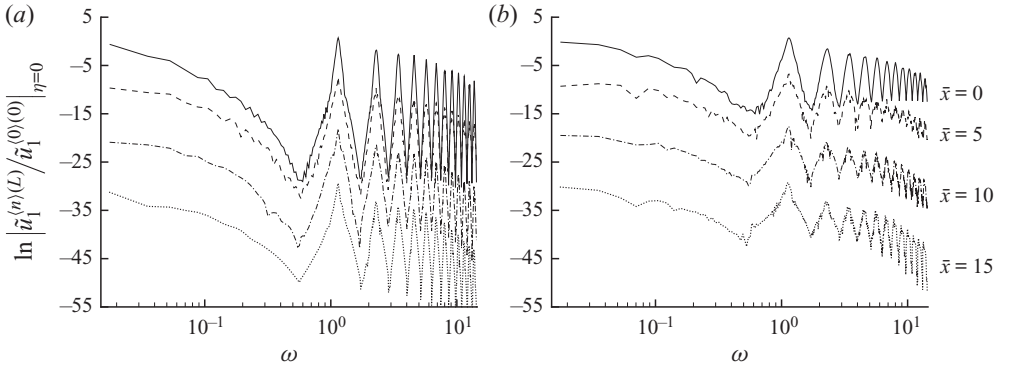


Figure 16. Spectrum of the axial velocity at the critical level at four axial positions $\bar{x} = 0$, 5, 10 and 15 for CS with a continuum of sidebands with two bandwidths, $6d = 0.25\omega_0$ (*a*), and $0.5\omega_0$ (*b*). The curves for $\bar{x} = 5$, 10, 15 have been moved 10, 20, 30 units downwards, respectively.

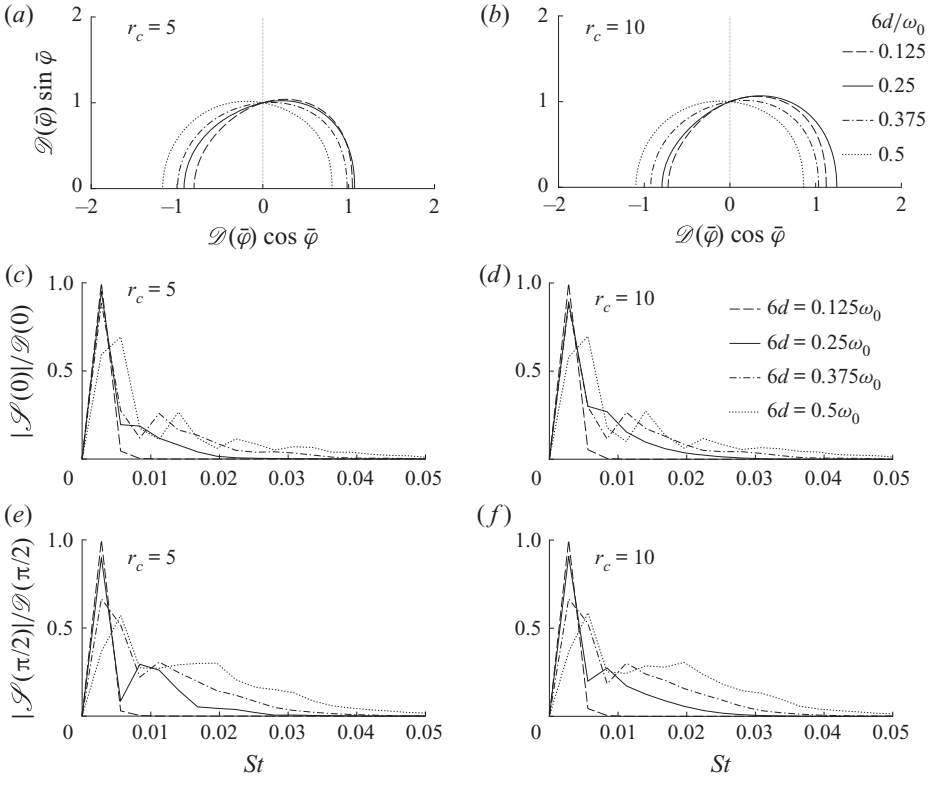


Figure 17. The acoustic field radiated from modulated CS consisting of a continuum of sidebands with different bandwidths $6d = 0.125\omega_0$, $0.25\omega_0$, $0.375\omega_0$ and $0.5\omega_0$, and $r_c = 5$ (*a*,*c*,*e*) and $r_c = 10$ (*b*,*d*,*f*): (*a*,*b*) directivity; (*c*–*f*) spectrum in two radiating directions, $\bar{\varphi} = 0$ and $\pi/2$.

4.4. *Limitation of the present work and comparison with experiments*

The limitation of the present work should be pointed out in the context of the overall jet noise. The latter is contributed by CS in the developed and near-nozzle regions, and possibly by fine-scale turbulence. CS in those regions have distinct scales and take

https://doi.org/10.1017/jfm.2022.252 Published online by Cambridge University Press

$6d/\omega_0$	0.125	0.25	0.375	0.5
$r_c = 5$	3.260×10^{-4}	3.266×10^{-3}	7.599×10^{-3}	1.442×10^{-2}
$r_c = 10$	7.688×10^{-4}	7.920×10^{-3}	1.496×10^{-2}	2.835×10^{-2}

Table 2. Values of the directivity function $\mathscr{D}(\pi/2)$ for different bandwidths in the continuum-sideband cases; these values are used to normalise $\mathscr{D}(\bar{\varphi})$ in figures 17(*a*,*b*).

different forms, e.g. ring mode and helical modes. Represented by wavepackets, CS may emit sound waves by (at least) two mechanisms: a linear mechanism, through which a spatially modulated wave radiates a sound wave of the same frequency (Tam & Morris 1980; Crighton & Huerre 1990; Cavalieri *et al.* 2012), and a nonlinear mechanism (Wu & Huerre 2009; Suponitsky *et al.* 2010; [I]), through which a spatially and temporally modulated wavepacket generates sound waves in a band of frequencies much lower than the central frequency of the CS. These two mechanisms operate simultaneously in reality, and their relative importance remains to be quantified. The present work has considered only the nonlinear mechanism pertinent just to ring-mode CS in the axial region just before the potential core ends. The sound waves so emitted are merely a low-frequency part of the overall broadband jet noise that is often measured. This makes a direct comparison hard. Zaman (1985) measured the directivity of a low-frequency sound wave with Strouhal number $St_D = 0.1$ under natural and forced conditions. Unfortunately, the data for the latter were expressed in terms of the excess sound over the former case. Comparison may be made only with the data for the natural condition, assuming that the dominant CS are close to the preferred mode with $St_D = 0.68$. Specific calculations were performed for the same flow conditions as in the experiment, with exhaust nozzle diameter $D^* = 25.4$ mm, jet exit velocity $U_j^* = 148\ \mathrm{m\ s^{-1}}$ and Mach number $M_J = 0.44$. With the air being supplied from the room, the jet was neither heated nor cooled, so its *total* temperature equals the ambient temperature, from which we obtain the ratio of the jet and ambient temperatures, $\beta_T = 1.040$.

From figure 21 of Zaman (1985), we infer that the low-frequency sound wave with $St_D = 0.1$ is radiated from a source located at $x^*/D^* = 7.5$, which should correspond to the neutral position of the preferred mode with $St_D = 0.68$. As the local momentum thickness is not available directly in the data, it is selected to be $\Theta^* = 1.524$ mm (or $0.06D^*$) such that the local neutral mode has $St_D = 0.68$. This value of Θ^* corresponds to a local shear-layer thickness $\delta_0^* = 4.39$ mm, or $r_c = 2.89$, which indicates that the jet is fairly well developed. Here, a velocity profile with $q_c = 0.4$ is used (and calculations for other values $0 < q_c < 0.5$ do not show significant difference). The Reynolds number based on δ_0^* is $Re = 21\,951$. The spreading rate of the shear layer is taken to be $\mathrm{d}\Theta^*/\mathrm{d}x^* = 0.0075$.

The initial seeded disturbance consists of three sideband components, specified as $(A_0^{(-1)}, A_0^{(0)}, A_0^{(1)}) = (\mathrm{e}^{-\mathrm{i}\pi/3}, 0.5, 1.5\,\mathrm{e}^{\mathrm{i}\pi/6})$. We select $\epsilon = 0.183$ such that the predicted sound intensity is of similar magnitude. With $Re = 21\,951$, the Haberman parameter is $\bar{\lambda} = 0.000582$, while other parameters are the same as those in case-$\mathcal{H}_R$, which we believe to be reasonable. The sound wave with $St_D = 0.1$, considered as being emitted through the present nonlinear mechanism, has a physical frequency $f_s^* = 582.68$ Hz, and the dimensionless frequency is $\omega_s = 4\pi f_s^* \delta_0^*/U_j^* = 0.217$. The difference frequency among the sideband modes is chosen to be $\omega_\nu = \frac{1}{2}\omega_s$ (so that $\Delta = 0.254$), and the directivity

https://doi.org/10.1017/jfm.2022.252 Published online by Cambridge University Press

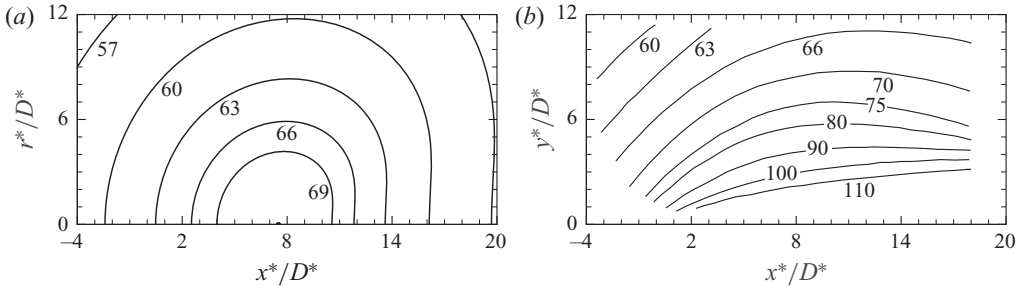


Figure 18. Comparison of contours of the low-frequency sound pressure level in dB with $St_D = 0.1$: (*a*) theoretical prediction by a model of modulated wavepacket with discrete sideband; (*b*) reproduction of the experimental measurement by Zaman (1985).

of the sound wave with $St_D = 0.1$ is represented by $\mathscr{D}^{(2)}$. The pressure contours of this sound wave are displayed in figure 18(*a*), while the measurement (figure 21(*a*) of Zaman 1985) is reproduced in figure 18(*b*). The qualitative features of the predicted and measured acoustic fields in the region $r^*/D^* > 6$ (i.e. $y^*/D^* > 6$) are quite similar, indicating that the nonlinear mechanism is at least a plausible one. Significant differences exist in the region $r^*/D^* < 6$ (i.e. $y^*/D^* < 6$), which is not surprising because the pressure in this radial range has not yet acquired the full character of sound, and on the other hand the theoretical result, the far-field asymptote, is not expected to hold either. Furthermore, the measured sound field may consist of contributions by other sources (e.g. CS of helical modes), which are not accounted for in our theory. Recently, LES were performed at high Reynolds numbers for clearly defined conditions, and the contributions to jet noise from the ring and helical modes have been documented (Lorteau, Cléro & Vuillot 2015; Brès *et al.* 2018). A proper comparison of the present theoretical prediction must be made with low-frequency sound waves that can be attributed to nonlinear mechanisms. Unfortunately, this cannot be done presently because on the one hand existing LES data of jet noise have not made clear attribution, and on the other hand the theory is yet to be extended to include multiple interacting helical modes. Further efforts on both fronts are required in order to perform definitive quantitative comparisons.

5. Conclusions and discussions

5.1. *Conclusions*

In this paper, a mathematical description was developed for the strongly nonlinear dynamics and the acoustic radiation of ring-mode CS on a subsonic turbulent circular jet, and with a minor modification it is also applicable to subsonic-mode ring-mode CS on supersonic turbulent jets. CS in such turbulent flows are regarded as wavepackets of unstable waves on the time-averaged mean flow profile, and can be described by hydrodynamic stability theories. The matched asymptotic expansion and multiple-scale methods were employed to derive the system that governs the nonlinear spatial–temporal evolution and modulation of the CS. The system consists of the amplitude equation for the envelope of the wavepacket, and the advection–diffusion type of equations for the vorticity and temperature in the critical layer. Different from laminar flows, it is necessary to taken into account the stronger non-parallelism, which consists of two aspects: (i) the axial variation of the mean-flow profile and the radial mean velocity; (ii) the drift of the critical level. Numerical solutions of the evolution system captured the most significant

https://doi.org/10.1017/jfm.2022.252 Published online by Cambridge University Press

characteristics of the CS, including vortex roll-up, saturation and attenuation, which are strongly nonlinear phenomena, mathematically related to the simultaneous excitation and amplification of higher harmonics. The theory shows that due to nonlinear effects, the low-frequency components as well as certain sidebands of the fundamental and harmonics exhibit significant jittering, which is likely to enhance acoustic radiation.

By analysing the far-field asymptote of the flow field associated with the CS under consideration, the precise physical process of radiation is described, physical sources in the present context are identified, and the radiated sound waves are determined on the basis of the first principles for the model considered. Here we concentrated on the low-frequency acoustic radiation, which is a nonlinear process. Wavepackets representing CS consist of a discrete band, or a continuum, of modes whose frequencies are quite close to each other, and the envelope modulates slowly in both time and axial direction. The nonlinear interaction of the wavepacket generates, in addition to high harmonics, spatially and temporally modulated mean-flow distortions, which consist of components with long time and length scales comparable with those of the wavepacket envelope. The dominant mean-flow distortion is, however, trapped completely within the critical layer. It is the subdominant breathing mean-flow distortion that acts as a non-compact emitter, with its constituting low-frequency components radiating sound waves to the far field. The Reynolds stresses driving this mean-flow distortion were thus identified to be the physical sources of sound. Since this mean-flow distortion does not play a leading order in the nonlinear dynamics of the CS, the sound waves are radiated by a dynamically insignificant part of the near-field fluctuations.

The nonlinear dynamics of ring-mode CS on a circular jet closely resemble that of two-dimensional CS on a planar mixing layer, and furthermore their acoustic radiations are through broadly the same radiation mechanism as described above. However, there are notable differences. For a circular jet, the equivalent source appearing in the acoustic analogy (of Lighthill form) can be determined fully before the acoustic field is, but that is impossible for a planar mixing layer (see [I]). The circularity of the jet flow weakens the strength of the radiated sound waves from $O(\epsilon^{5/2})$ for a planar shear layer to $O(\epsilon^3)$. Our theory predicts that the low-frequency acoustic field features a monopole-like directivity, consistent with experimental measurements available. The spectrum of the acoustic field can also be predicted. The calculations showed that the spectrum could cover a significant frequency band of jet noise, including the peak-radiation frequency, provided that the spectrum of the wavepacket modelling the CS has a suitable bandwidth.

5.2. *Reflection and prospect*

The result that the equivalence source could be determined raises the possibility of treating the acoustic radiation by ring-mode CS in the framework of an acoustic analogy. Our analysis indicates that the equivalent source consists of two parts, the Reynolds stresses $\mathcal{S}_R$, generated by the quadratic nonlinear interaction of the wavepacket in the main jet flow, and the interaction in the critical layer leading to jump $\mathcal{U}$. It appears that the radiation due to the first part could be accounted for alternatively and equivalently (in the asymptotic sense) by using the Lilley–Goldstein analogy, or a more general form (e.g. Goldstein 2005) since the wave operator in the analogy can be viewed as a composite representation of the equations in the main jet and the acoustic region in our approach. However, it is rather doubtful to account for in the same way the radiation due to the second part because the generation of the jump by the critical-layer forcing is a full hydrodynamic process, described by viscous

https://doi.org/10.1017/jfm.2022.252 Published online by Cambridge University Press

and strongly nonlinear operators, both effects being absent in the wave operator of the acoustic analogy.

The omnidirectional nature of the acoustic field prompts us to speculate about the generation of the noise attributed to fine-scale turbulence, which exhibits a similar directivity (Tam *et al.* 1996). An intriguing feature of this part of jet noise is that its dominant components are actually in the fairly low or moderate frequency band corresponding to the nozzle-diameter-based Strouhal number $St_D < 1.5$, despite the fact that fine-scale turbulent fluctuations in the shear region concentrate in a high-frequency spectral band $St_D > 3$. The frequency disparity in the spectra may imply that rather than fine-scale turbulence, the direct emitters of the dominant noise must be near-field fluctuations with much lower frequencies and hence much longer wavelengths. Such fluctuations may be of a similar kind to the slowly modulating mean-flow distortion described in the present paper, and are probably driven or sustained by the Reynolds stresses of fine-scale turbulence and/or large-scale CS. It appears that two fundamental mechanisms may be operating simultaneously in a circular jet to generate mixing noise: the linear Mach-wave radiation mechanism by which CS emit sound waves of the same frequencies to directions making small angles to the downstream axis, and the nonlinear mechanism by which CS and fine-scale turbulence radiate lower-frequency sound waves to all directions. In the present paper, we focused on the second mechanism and CS, but it would be interesting to analyse the first as well for the same CS in order to quantify the relative importance of the two mechanisms. It is worth noting that the instability of the near-nozzle region occurs in a frequency band up to $St_D \approx 7$. It is not unreasonable to expect that CS in this region could generating lower-frequency sound waves in a band up to $St_D = 1.5$ through the nonlinear mechanism, while emitting high-frequency noise with $St_D > 1.5$ through the direct Mach-wave radiation.

The factor $r_c^{-1} = \delta_T^*/r_T^*$ influences both the dynamics and radiation of CS on jets, where δ_T^* and r_T^* measure the shear-layer thickness and its central position, respectively. The present theory assumes that $r_c = O(1)$, but needs to be modified in the near-nozzle regions where $r_c^{-1} \ll 1$. A distinguished near-nozzle region corresponds to $r_c^{-1} = O(l_\gamma)$, where l_γ is the magnitude of the linear growth rate of the disturbance. In this region, the evolution–modulation system might retain the present form for the present ring-mode CS, but the description of the acoustic radiation requires modification because an inner sound field would arise, rendering the radiation to be like that in the planar case considered in [I]. Furthermore, helical-mode CS are known to co-exist with the ring-mode CS, and sound waves emitted by modes with different azimuthal wavenumbers display different directivity and spectra. It is therefore important to analyse the dynamics of multiple co-existing modes as well as their radiation. Finally, the relative importance of the linear Mach-wave and nonlinear low-frequency radiation mechanisms needs to be quantified. Further work on these aspects is being pursued in order to enable a definitive quantitative comparison with emerging detailed numerical (LES or DNS) and experimental data, which is necessary for establishing the role of the currently plausible nonlinear radiation mechanism in jet noise.

Acknowledgements. We would like to thank the reviewers for their comments and suggestions.

Funding. This work was supported by NSFC (Grant nos 91752116, 11472190).

Declaration of interests. The authors report no conflict of interest.

Author ORCIDs.
Zhongyu Zhang https://orcid.org/0000-0002-4447-6014;
Xuesong Wu https://orcid.org/0000-0002-3406-8017.

https://doi.org/10.1017/jfm.2022.252 Published online by Cambridge University Press

Appendix A. Derivations of the governing equations

Substituting expansions (2.42) and (2.43), the scalings (2.8*a*,*b*)–(2.10) and the Taylor expansions of the mean flow about the critical level into CS equations, we can obtain a series of equations at $O(\epsilon^{(k+1)/2})$ ($k = 1, 2, 3$). The solution within the critical layer for $\tilde{v}_0$ and $\tilde{p}_0$ is found as

$$\tilde{v}_0 = -\mathrm{i}\alpha A^\dagger \,\mathrm{e}^{\mathrm{i}\alpha\zeta} + \mathrm{c.c.}, \quad \tilde{p}_0 = \left(\bar{U}_c'/\bar{T}_c\right) A^\dagger \,\mathrm{e}^{\mathrm{i}\alpha\zeta} + \mathrm{c.c.}, \tag{A1a,b}$$

which are simply the trivial continuation of the outer solution. Collecting $O(\epsilon^{3/2})$ terms of the energy equation shows that $\tilde{T}_0$ satisfies the equation

$$\mathcal{L}_{N,1}^\dagger \tilde{T}_0 = (\gamma - 1)\, Ma^2 \bar{T}_c \left[\frac{\partial \tilde{p}_0}{\partial \tau} + \frac{\partial \tilde{p}_0}{\partial \bar{x}} + \left(\bar{U}_c' Y + \bar{U}_{1,c}\bar{x}\right)\frac{\partial \tilde{p}_0}{\partial \zeta}\right] - \left(\bar{T}_c'' Y + \bar{T}_{1,c}'\bar{x} + \bar{T}_{cM}'\right)\tilde{v}_0, \tag{A2}$$

where $\mathcal{L}_{N,1}^\dagger$ is defined by (2.49). In order to aid the matching with the outer solution, we make a substitution (2.45) and then arrive at (2.47).

At $O(\epsilon)$ expansions of the continuity and momentum equations, we have

$$\frac{\partial \tilde{u}_0}{\partial \zeta} + \frac{\partial \tilde{v}_1}{\partial Y} + \frac{\tilde{v}_0}{r_c} = 0, \tag{A3}$$

$$\mathcal{L}_{N,2}^\dagger \tilde{u}_0 = -\bar{U}_c' \tilde{v}_1 - \left(\bar{U}_c'' Y + \bar{U}_{1,c}'\bar{x}\right)\tilde{v}_0 - \bar{T}_c\left(\frac{\partial \tilde{p}_1}{\partial \zeta} + \frac{\partial \tilde{p}_0}{c\,\partial \bar{x}}\right) - \left(\bar{T}_c' Y + \bar{T}_{1,c}\bar{x}\right)\frac{\partial \tilde{p}_0}{\partial \zeta}, \tag{A4}$$

$$\frac{\partial \tilde{p}_1}{\partial Y} = 0, \tag{A5}$$

where $\bar{T}_c' = O(1)$ is reinstated since scaling $\bar{T}_c'$ as $O(\epsilon^{1/2})$ is only to make the dynamical system strongly nonlinear. Differentiating (A4) with respect to Y, and inserting (A1*b*), (A3) and (A5), we have

$$\mathcal{L}_{N,2}^\dagger \tilde{u}_{0,Y} = -\bar{U}_c'\left(\frac{\bar{T}_c'}{\bar{T}_c} - \frac{\bar{U}_c''}{\bar{U}_c'} + \frac{1}{r_c}\right)\tilde{v}_0; \tag{A6}$$

the right-hand side vanishes in view of the generalised-inflection-point condition. The solution matching with the outer expansion is found as

$$\tilde{u}_0 = -b_1 A^\dagger \,\mathrm{e}^{\mathrm{i}\alpha\zeta} + \mathrm{c.c.} \tag{A7}$$

The $O(\epsilon^{3/2})$ expansions of the continuity and momentum equations give

$$\begin{aligned}
&\left[\frac{\partial}{\partial \tau} + \frac{\partial}{\partial \bar{x}} + (\bar{U}_c' Y + \bar{U}_{1,c}\bar{x})\frac{\partial}{\partial \zeta} - (\mathrm{i}\alpha A^\dagger \,\mathrm{e}^{\mathrm{i}\alpha\zeta} + \mathrm{c.c.} - \sigma \bar{V}_c)\frac{\partial}{\partial Y}\right]\tilde{T}_0 \\
&\quad + \left(\bar{T}_c'' Y + \bar{T}_{1,c}'\bar{x} + \bar{T}_{cM}'\right)\tilde{v}_0 - \gamma\, Ma^2 \bar{T}_c\left[\frac{\partial}{\partial \tau} + \frac{\partial}{\partial \bar{x}} + \left(\bar{U}_c' Y + \bar{U}_{1,c}\bar{x}\right)\frac{\partial}{\partial \zeta}\right]\tilde{p}_0 \\
&= \bar{T}_c\left(\frac{\partial \tilde{u}_1}{\partial \zeta} + \frac{\partial \tilde{v}_2}{\partial Y} + \frac{\partial \tilde{u}_0}{c\,\partial \bar{x}} + \frac{\tilde{v}_1}{r_c} - \frac{\tilde{v}_0 Y}{r_c^2}\right) + \left(\bar{T}_c' Y + \bar{T}_{1,c}\bar{x}\right)\left(\frac{\partial \tilde{u}_0}{\partial \zeta} + \frac{\partial \tilde{v}_1}{\partial Y} + \frac{\tilde{v}_0}{r_c}\right),
\end{aligned} \tag{A8}$$

https://doi.org/10.1017/jfm.2022.252 Published online by Cambridge University Press

$$\mathcal{L}^{\dagger}_{N,2}\tilde{u}_1 = \bar{\lambda}\bar{T}_c\bar{U}'_c\mu'_c\frac{\partial\tilde{T}_0}{\partial Y} - \bar{T}_c\left(\frac{\partial\tilde{p}_2}{\partial\zeta} + \frac{\partial\tilde{p}_1}{c\,\partial\bar{x}}\right) - \left(\bar{T}'_cY + \bar{T}_{1,c}\bar{x}\right)\left(\frac{\partial\tilde{p}_1}{\partial\zeta} + \frac{\partial\tilde{p}_0}{c\,\partial\bar{x}}\right)$$
$$- \left(\frac{1}{2}\bar{T}''_cY^2 + \bar{T}'_{1,c}\bar{x}Y + \frac{1}{2}\bar{T}_{2,c}\bar{x}^2\right)\frac{\partial\tilde{p}_0}{\partial\zeta} - \tilde{T}_0\frac{\partial\tilde{p}_0}{\partial\zeta} - \tilde{u}_0\frac{\partial\tilde{u}_0}{\partial\zeta}$$
$$- \bar{U}'_c\tilde{v}_2 - \left(\bar{U}''_cY + \bar{U}'_{1,c}\bar{x}\right)\tilde{v}_1 - \left(\frac{1}{2}\bar{U}'''_cY^2 + \bar{U}''_{1,c}\bar{x}Y + \frac{1}{2}\bar{U}'_{2,c}\bar{x}^2\right)\tilde{v}_0$$
$$- \bar{U}_{1,c}\tilde{u}_0 - \left(\bar{U}'_cY + \bar{U}_{1,c}\bar{x}\right)\frac{\partial\tilde{u}_0}{c\,\partial\bar{x}} - \left(\frac{1}{2}\bar{U}''_cY^2 + \bar{U}'_{1,c}\bar{x}Y + \frac{1}{2}\bar{U}_{2,c}\bar{x}^2\right)\frac{\partial\tilde{u}_0}{\partial\zeta}$$
$$- (\gamma\,Ma^2\tilde{p}_0 - \tilde{T}_0/\bar{T}_c)(\bar{U}_{1,c} + c^{-1}\sigma\bar{U}'_c\bar{V}_c), \tag{A9}$$

$$\frac{\partial\tilde{v}_0}{\partial\tau} + \frac{\partial\tilde{v}_0}{\partial\bar{x}} + \left(\bar{U}'_cY + \bar{U}_{1,c}\bar{x}\right)\frac{\partial\tilde{v}_0}{\partial\zeta} = -\bar{T}_c\frac{\partial\tilde{p}_2}{\partial Y}. \tag{A10}$$

To find the vorticity, we differentiate (A9) with respect to Y and obtain the equation

$$\mathcal{L}^{\dagger}_{N,2}\tilde{u}_{1,Y} = \bar{\lambda}\bar{T}_c\bar{U}'_c\mu'_c\frac{\partial^2\tilde{T}_0}{\partial Y^2} - \bar{T}_c\frac{\partial^2\tilde{p}_2}{\partial Y\,\partial\zeta} - \bar{T}'_c\left(\frac{\partial\tilde{p}_1}{\partial\zeta} + \frac{\partial\tilde{p}_0}{c\,\partial\bar{x}}\right) - \left(\bar{T}''_cY + \bar{T}'_{1,c}\bar{x}\right)\frac{\partial\tilde{p}_0}{\partial\zeta}$$
$$- \frac{\partial\tilde{T}_0}{\partial Y}\frac{\partial\tilde{p}_0}{\partial\zeta} - \bar{U}''_c\tilde{v}_1 - \left(\bar{U}'''_cY + \bar{U}''_{1,c}\bar{x}\right)\tilde{v}_0 - \bar{U}'_c\left(\frac{\partial\tilde{u}_1}{\partial\zeta} + \frac{\partial\tilde{v}_2}{\partial Y} + \frac{\partial\tilde{u}_0}{c\,\partial\bar{x}}\right)$$
$$- \left(\bar{U}''_cY + \bar{U}'_{1,c}\bar{x}\right)\left(\frac{\partial\tilde{u}_0}{\partial\zeta} + \frac{\partial\tilde{v}_1}{\partial Y}\right) + \frac{\bar{U}'_c}{\bar{T}_c}\left(\bar{U}_{1,c}/\bar{U}'_c + \sigma\bar{V}_c/c\right)\frac{\partial\tilde{T}_0}{\partial Y}. \tag{A11}$$

On the right-hand side, $(\partial_\zeta\tilde{u}_0 + \partial_Y\tilde{v}_1)$, $(\partial_\zeta\tilde{u}_1 + \partial_Y\tilde{v}_2 + c^{-1}\partial_{\bar{x}}\tilde{u}_0)$, $(\partial_\zeta\tilde{p}_1 + c^{-1}\partial_{\bar{x}}\tilde{p}_0)$ and $\partial^2_{\zeta Y}\tilde{p}_2$ can be derived from (A3), (A8), (A4) and (A10), respectively, and (A11) becomes

$$\mathcal{L}^{\dagger}_{N,2}\tilde{u}_{1,Y} = -\bar{\lambda}\bar{U}'_c\left(\mu_c/Pr - \bar{T}_c\mu'_c\right)\frac{\partial^2\tilde{T}_0}{\partial Y^2} - \frac{\tilde{\lambda}\bar{U}'_c\tilde{\mu}_{t,c}}{Pr_T}\frac{\partial^2\tilde{T}_0(t-\hat{\tau}_1)}{\partial Y^2}$$
$$+ \frac{\bar{U}'_c}{\bar{T}_c}\frac{\partial\tilde{T}_0}{\partial Y}\left(\tilde{v}_0 + \bar{U}_{1,c}/\bar{U}'_c + \sigma\bar{V}_c/c\right) + \bar{U}'_c\left(\frac{\bar{T}'_c}{\bar{T}_c} - \frac{\bar{U}''_c}{\bar{U}'_c} + \frac{1}{r_c}\right)\tilde{v}_1$$
$$- \bar{U}'_c\left[\left(\frac{\bar{U}'''_c}{\bar{U}'_c} - \frac{\bar{T}'''_c}{\bar{T}_c}\right)Y + \left(\frac{\bar{U}''_{1,c}}{\bar{U}'_c} - \frac{\bar{T}'_{1,c}}{\bar{T}_c}\right)\bar{x}\right]\tilde{v}_0$$
$$+ \frac{\bar{U}'_c}{r_c}\left[\left(\frac{\bar{U}''_c}{\bar{U}'_c} - \frac{1}{r_c}\right)Y + \frac{\bar{U}'_{1,c}}{\bar{U}'_c}\bar{x}\right]\tilde{v}_0$$
$$+ \bar{T}'_c\frac{\bar{U}'_c}{\bar{T}_c}\left[\left(\frac{\bar{U}''_c}{\bar{U}'_c} - \frac{\bar{T}'_c}{\bar{T}_c}\right)Y + \left(\frac{\bar{U}'_{1,c}}{\bar{U}'_c} - \frac{\bar{T}_{1,c}}{\bar{T}_c}\right)\bar{x}\right]\tilde{v}_0$$
$$+ \left[\frac{\partial}{\partial\tau} + \frac{\partial}{\partial\bar{x}} + \left(\bar{U}'_cY + \bar{U}_{1,c}\bar{x}\right)\frac{\partial}{\partial\zeta}\right]\left(\frac{\partial\tilde{v}_0}{\partial\zeta} + \bar{U}'_cMa^2\tilde{p}_0 + \frac{\bar{T}'_c}{\bar{T}_c}\tilde{u}_0\right). \tag{A12}$$

https://doi.org/10.1017/jfm.2022.252 Published online by Cambridge University Press

After substituting r_c^{-1} by $[(\bar{U}_c''/\bar{U}_c') - (\bar{T}_c'/\bar{T}_c)]$, (A12) becomes

$$\begin{aligned}\mathcal{L}_{N,2}^{\dagger}\tilde{u}_{1,Y} = &-\bar{\lambda}\bar{U}_c'\left(\mu_c/Pr - \bar{T}_c\mu_c'\right)\frac{\partial^2\tilde{T}_0}{\partial Y^2} - \frac{\tilde{\lambda}\bar{U}_c'\tilde{\mu}_{t,c}}{Pr_T}\frac{\partial^2\tilde{T}_0(t-\hat{\tau}_1)}{\partial Y^2}\\ &+\frac{\bar{U}_c'}{\bar{T}_c}\frac{\partial\tilde{T}_0}{\partial Y}\left(\tilde{v}_0 + \bar{U}_{1,c}/\bar{U}_c' + \sigma\bar{V}_c/c\right) + \bar{U}_c'\left(jY + j_1\bar{x}\right)\tilde{v}_0\\ &+\left[\frac{\partial}{\partial\tau} + \frac{\partial}{\partial\bar{x}} + \left(\bar{U}_c'Y + \bar{U}_{1,c}\bar{x}\right)\frac{\partial}{\partial\zeta}\right]\left(\frac{\partial\tilde{v}_0}{\partial\zeta} + \bar{U}_c'Ma^2\tilde{p}_0 + \frac{\bar{T}_c'}{\bar{T}_c}\tilde{u}_0\right). \quad \text{(A13)}\end{aligned}$$

After substituting (2.46) into (A13), we finally arrive at (2.48).

Appendix B. Governing equations and the upstream and boundary conditions in terms of the Fourier components

Inserting (3.6) and (3.7) into (3.2) yields the equations governing $A^{(L)}$, $T_n^{(L)}$ and $Q_n^{(L)}$:

$$\begin{aligned}&(\tilde{\Lambda}_2 + L\Delta\tilde{\Lambda}_{d,2})\frac{\partial A^{(L)}}{\partial\bar{x}} + (\tilde{\Lambda}_0 - L\Delta\tilde{\Lambda}_1 + L^2\Delta^2\tilde{\Lambda}_{d,1})A^{(L)}\\ &\quad= \left(q_1 - q_2\bar{x} + \frac{2L\Delta\Lambda_d}{\tilde{H}\Lambda_2}\right)I_{10}^{(L)} + \frac{2}{\tilde{H}}I_{11}^{(L)} + \frac{4}{\tilde{H}^2\Lambda_2}[I_{12}^{(L)} + \mathrm{i}\chi I_{10}^{(L)} - A^{(-L)*} * I_{20}^{(L)}], \quad \text{(B1}a\text{)}\\ &\left(\frac{\partial}{\partial\bar{x}} + \mathrm{i}n\eta - \mathrm{i}L\Delta + \chi\frac{\partial}{\partial\eta} - \lambda_{1n}\frac{\partial^2}{\partial\eta^2}\right)T_n^{(L)} + \mathrm{i}\frac{\partial}{\partial\eta}[A^{(-L)*} * T_{n+1}^{(L)} - A^{(L)} * T_{n-1}^{(L)}]\\ &\quad= -\delta_{n1}\left(p_1\frac{\partial}{\partial\bar{x}} - \mathrm{i}p_1L\Delta - \mathrm{i}p_1S_0 - \mathrm{i}p_2 - \mathrm{i}\chi_1\bar{x}\right)A^{(L)}, \quad \text{(B1}b\text{)}\\ &\left(\frac{\partial}{\partial\bar{x}} + \mathrm{i}n\eta - \mathrm{i}L\Delta + \chi\frac{\partial}{\partial\eta} - \lambda_{2n}\frac{\partial^2}{\partial\eta^2}\right)Q_n^{(L)} + \mathrm{i}\frac{\partial}{\partial\eta}[A^{(-L)*} * Q_{n+1}^{(L)} - A^{(L)} * Q_{n-1}^{(L)}]\\ &\quad= \mathrm{i}p_3\frac{\partial}{\partial\eta}[A^{(-L)*} * T_{n+1}^{(L)} - A^{(L)} * T_{n-1}^{(L)}] + p_3\chi\frac{\partial T_n^{(L)}}{\partial\eta}\\ &\qquad- p_3\lambda_{3n}\frac{\partial^2 T_n^{(L)}}{\partial\eta^2} - \delta_{n1}\left(\frac{\partial}{\partial\bar{x}} - \mathrm{i}L\Delta - \mathrm{i}S_0 - \mathrm{i}\chi_2\bar{x}\right)A^{(L)}, \quad \text{(B1}c\text{)}\end{aligned}$$

where $\tilde{H}$ is a large domain size but finite, and

$$I_{nk}^{(L)}(\bar{x}) = \int_{-\tilde{H}}^{\tilde{H}} Q_n^{(L)}(\bar{x},\eta)\,\eta^k\,\mathrm{d}\eta. \quad \text{(B2)}$$

https://doi.org/10.1017/jfm.2022.252 Published online by Cambridge University Press

Here, (B1*a*) is a reduced ordinary differential equation for $A^{(L)}$, whose derivation is similar to that in the Appendix A of Wu & Zhuang (2016), and the coefficients are

$$\left.\begin{aligned}
\Lambda_d &= \Lambda_1 - \Lambda_2,\\
\tilde{\Lambda}_1 &= -(q_1 - q_2\bar{x})[\Lambda_1 - 2\,(S_0 - p_1p_3\chi + \chi_2\bar{x})\,/\tilde{H}]\\
&-\frac{2}{\tilde{H}}\{l_1 + l_2\bar{x} + \Lambda_d[(\Lambda_0 + 2p_3\chi_1\chi/\tilde{H})\bar{x} + S_1]/\Lambda_2 - 2\mathrm{i}\chi_2\Lambda_d/(\tilde{H}\Lambda_2)\},\\
\tilde{\Lambda}_2 &= -(q_1 - q_2\bar{x})[\Lambda_2 - 2\,(S_0 - p_1p_3\chi + \chi_2\bar{x})\,/\tilde{H}] - 2(l_1 + l_2\bar{x})/\tilde{H},\\
\tilde{\Lambda}_{d,j} &= 2\Lambda_d[\Lambda_2 - 2\,(S_0 - p_1p_3\chi + \chi_2\bar{x})\,/\tilde{H} + \Lambda_j]/(\tilde{H}\Lambda_2) \quad (j = 1, 2),\\
\tilde{\Lambda}_0 &= (q_1 - q_2\bar{x})[(\Lambda_0 + 2p_3\chi_1\chi/\tilde{H})\bar{x} + S_1 - 2\mathrm{i}\chi_2/\tilde{H}] + 2(r_1 + r_2\bar{x})/\tilde{H},
\end{aligned}\right\} \tag{B3}$$

with

$$\left.\begin{aligned}
S_1 &= 2(S_0\Lambda_1 + S_0p_1p_3\chi + p_2p_3\chi)/\tilde{H},\\
q_1 &= \Lambda_2 - 2(S_0 - p_1p_3\chi)/\tilde{H} + 4/\Lambda_2 + 2S_1/(\tilde{H}\Lambda_2),\\
q_2 &= 2\chi_2/\tilde{H} - 2(\Lambda_0 + 2p_3\chi_1\chi/\tilde{H})/(\tilde{H}\Lambda_2),\\
l_1 &= 2\tilde{H} + S_1 + 4(S_0 - p_1p_3\chi)/\Lambda_2 + 4\mathrm{i}(\Lambda_0 + 2p_3\chi_1\chi/\tilde{H})/(\tilde{H}\Lambda_2) - 4\mathrm{i}\chi_2/\tilde{H},\\
l_2 &= (\Lambda_0 + 2p_3\chi_1\chi/\tilde{H}) + 4\chi_2/\Lambda_2, \quad r_2 = 2\chi_2\tilde{H},\\
r_1 &= 2(S_0 - p_1p_3\chi)\tilde{H} + \mathrm{i}(\Lambda_0 + 2p_3\chi_1\chi/\tilde{H}) + 4\mathrm{i}\chi_2/\Lambda_2.
\end{aligned}\right\} \tag{B4}$$

We now determine the upstream conditions for $T_n^{(L)}$ and $Q_n^{(L)}$. As $\bar{x} \to -\infty$, the nonlinear terms in (B1*b*) and (B1*c*) can be dropped due to small initial amplitude, so only the fundamental components, $T_1^{(L)}$ and $Q_1^{(L)}$, are present and are found as

$$\begin{aligned}
[T_1^{(L)}, Q_1^{(L)}] \to -\int_0^\infty &[\mathscr{T}_A^{(L)}(\xi;\tau,\bar{x})\exp(-\lambda_{11}\xi^3/3), \mathscr{Q}_A^{(L)}(\xi;\tau,\bar{x})\exp(-\lambda_{21}\xi^3/3)]\\
&\times \exp(\mathrm{i}\chi\xi^2/2 - \mathrm{i}\bar{\eta}\xi)\,\mathrm{d}\xi,
\end{aligned} \tag{B5}$$

with

$$\left.\begin{aligned}
\mathscr{T}_A^{(L)}(\xi;\tau,\bar{x}) &= \left[p_1\left(\frac{\partial}{\partial\tau} + \frac{\partial}{\partial\bar{x}}\right) - \mathrm{i}p_2 - \mathrm{i}\chi_1\,(\bar{x} - \xi)\right]A^{(L)}(\tau - \xi, \bar{x} - \xi),\\
\mathscr{Q}_A^{(L)}(\xi;\tau,\bar{x}) &= p_3\,\mathscr{T}_A^{(L)}(\xi;\tau,\bar{x})\int_0^\xi (\lambda_{31}\xi^{\dagger 2} - \mathrm{i}\chi\xi^\dagger)\exp(-(\lambda_{11} - \lambda_{21})\xi^{\dagger 3}/3)\,\mathrm{d}\xi^\dagger\\
&+\left[\frac{\partial}{\partial\tau} + \frac{\partial}{\partial\bar{x}} - \mathrm{i}\chi_2\,(\bar{x} - \xi)\right]A^{(L)}(\tau - \xi, \bar{x} - \xi),
\end{aligned}\right\} \tag{B6}$$

and λ_{i1} $(i = 1, 2, 3)$ being the normalised complex eddy conductivities and viscosities for the fundamental components, defined as

$$\lambda_{1n} = \bar{\lambda}_1 + \tilde{\lambda}_1\,\mathrm{e}^{\mathrm{i}n\omega\hat{\tau}_1}, \quad \lambda_{2n} = \bar{\lambda}_2 + \tilde{\lambda}_2\,\mathrm{e}^{\mathrm{i}n\omega\hat{\tau}_2}, \quad \lambda_{3n} = \bar{\lambda}_3 + \tilde{\lambda}_3\,\mathrm{e}^{\mathrm{i}n\omega\hat{\tau}_1}, \quad n \in \mathbb{N}. \tag{B7}$$

For the mathematical problem to be well posed, the effective conductivity and diffusivity must be positive for $\hat{\tau}_i \neq 0$ $(i = 1, 2)$, and it is thus necessary to restrict $\tilde{\lambda}_i \leqslant \bar{\lambda}_i$ $(i = 1, 2)$.

https://doi.org/10.1017/jfm.2022.252 Published online by Cambridge University Press

The boundary conditions of $T_n^{(L)}$ and $Q_n^{(L)}$ follow from the dominant balances in (B1*b*)–(B1*c*) as $\eta \to \pm\infty$. After ignoring the $O(\eta^{-4})$ terms, they are written as

$$T_1^{(L)} \to \left(\frac{\mathrm{i}}{\eta} - \frac{\mathcal{D}_0^{(L)}}{\eta^2} - \frac{\mathrm{i}\mathcal{D}_0^{(L)}\mathcal{D}_0^{(L)}}{\eta^3} + \frac{\chi}{\eta^3}\right)(p_1\mathcal{D}_0^{(L)} - \mathrm{i}p_1 S_0 - \mathrm{i}p_2 - \mathrm{i}\chi_1\bar{x})A^{(L)} + O(\eta^{-4}), \tag{B8a}$$

$$\begin{aligned} T_0^{(L)} \to & -\frac{p_1 A^{(L)} * A^{(-L)*}}{\eta^2} \\ & + \frac{2}{\eta^3}[\mathrm{i}p_1[A^{(L)} * \mathcal{D}_0^{(L)}A^{(-L)*} - A^{(-L)*} * \mathcal{D}_0^{(L)}A^{(L)} + \mathrm{i}S_0 A^{(L)} * A^{(-L)*}] \\ & - (p_2 + \chi_1\bar{x})\, A^{(L)} * A^{(-L)*} - (\chi_1 + p_1\chi)\, \mathcal{B}_1^{(L)}] + O(\eta^{-4}), \end{aligned} \tag{B8b}$$

$$T_2^{(L)} \to -\frac{\mathrm{i}}{2\eta^3}A^{(L)} * (p_1\mathcal{D}_0^{(L)} - \mathrm{i}p_1 S_0 - \mathrm{i}p_2 - \mathrm{i}\chi_1\bar{x})A^{(L)} + O(\eta^{-4}), \tag{B8c}$$

$$\begin{aligned} Q_1^{(L)} \to & \left(\frac{\mathrm{i}}{\eta} - \frac{\mathcal{D}_0^{(L)}}{\eta^2} - \frac{\mathrm{i}\mathcal{D}_0^{(L)}\mathcal{D}_0^{(L)}}{\eta^3} + \frac{\chi}{\eta^3}\right)(\mathcal{D}_0^{(L)} - \mathrm{i}S_0 - \mathrm{i}\chi_2\bar{x})A^{(L)} \\ & - p_3\chi\left(\frac{\mathrm{i}}{\eta^2} - \frac{2\mathcal{D}_0^{(L)}}{\eta^3}\right)(p_1\mathcal{D}_0^{(L)} - \mathrm{i}p_1 S_0 - \mathrm{i}p_2 - \mathrm{i}\chi_1\bar{x})A^{(L)} + O(\eta^{-4}), \end{aligned} \tag{B9a}$$

$$\begin{aligned} Q_0^{(L)} \to & -\frac{(1 - p_1 p_3)\, A^{(L)} * A^{(-L)*}}{\eta^2} \\ & + \frac{2}{\eta^3}\{\mathrm{i}\,(1 - p_1 p_3)\,[A^{(L)} * \mathcal{D}_0^{(L)}A^{(-L)*} - A^{(-L)*} * \mathcal{D}_0^{(L)}A^{(L)}] \\ & - [S_0 - p_3\,(p_1 S_0 + p_2 + p_1\chi) + (\chi_2 - p_3\chi_1)\,\bar{x}]A^{(L)} * A^{(-L)*} \\ & - [\chi_2 - p_3\chi_1 + \chi\,(1 - p_1 p_3)]\mathcal{B}_1^{(L)}\} + O(\eta^{-4}), \end{aligned} \tag{B9b}$$

$$Q_2^{(L)} \to -\frac{\mathrm{i}A^{(L)}}{2\eta^3} * \{-p_3(p_1\mathcal{D}_0^{(L)} - \mathrm{i}p_1 S_0 - \mathrm{i}p_2 - \mathrm{i}\chi_1\bar{x}) + \mathcal{D}_0^{(L)} - \mathrm{i}S_0 - \mathrm{i}\chi_2\bar{x}\}A^{(L)} + O(\eta^{-4}), \tag{B9c}$$

where we have put

$$\mathcal{D}_0^{(L)} = \frac{\partial}{\partial\bar{x}} - \mathrm{i}L\Delta, \quad \mathcal{B}_1^{(L)}(\tau,\bar{x}) = \int_0^\infty A^{(L)}(\tau - \xi, \bar{x} - \xi) * A^{(-L)*}(\tau - \xi, \bar{x} - \xi)\,\mathrm{d}\xi. \tag{B10a,b}$$

https://doi.org/10.1017/jfm.2022.252 Published online by Cambridge University Press

Appendix C. List of coefficients in the expression of $\mathcal{S}_R$ in (3.18)–(3.19)

$$\tilde{J}^{\pm}_{rj}(r) = \frac{1}{r}\int_{\infty(0)}^{r} \frac{r^{\star}\bar{T}}{(\bar{U}-c)^2}\left(\mathcal{G}_{j1}\hat{p}_0'\hat{p}_0 + \alpha^2\mathcal{G}_{j2}\hat{p}_0^2\right)\mathrm{d}r^{\star} \quad (j=0,1,2); \tag{C1}$$

$$\left.\begin{aligned}
S^{\dagger}_{10}(r) &= 2\bar{T}'\tilde{J}^{\pm}_{r1}(r) + 2\left[(\bar{U}-c)^2 Ma^2 - \bar{T}\right]p_{Mr},\\
S^{\dagger}_{11}(r) &= (\gamma+1)\,Ma^2\bar{T} - \frac{\bar{T}^2}{(\bar{U}-c)^2} - (2\gamma+1)\,Ma^4(\bar{U}-c)^2,\\
S^{\dagger}_{12}(r) &= \frac{\bar{T}^2(\bar{U}''-\bar{U}'/r)}{\alpha^4(\bar{U}-c)^3} + \frac{\bar{T}^2}{\alpha^2(\bar{U}-c)^2} - \frac{\bar{U}'^2\bar{T}^2}{\alpha^4(\bar{U}-c)^4}\\
&\quad + \frac{3\bar{U}'\bar{T}'\bar{T}}{\alpha^2(\bar{U}-c)^3} - \frac{3Ma^2\bar{T}}{\alpha^2},\\
S^{\dagger}_{13}(r) &= \frac{5\bar{T}'\bar{T}}{\alpha^2(\bar{U}-c)^2} - \frac{2\bar{U}'\bar{T}^2}{\alpha^2(\bar{U}-c)^3} - \frac{2Ma^2\bar{U}'\bar{T}}{\alpha^2(\bar{U}-c)} - \frac{(\gamma+3)Ma^2\bar{T}'}{\alpha^2};
\end{aligned}\right\} \tag{C2}$$

$$\left.\begin{aligned}
S^{\dagger}_{20}(r) &= -Ma^2\bar{U}'\,\tilde{J}^{\pm}_{r2}(r) + 2Ma^2 p_{Mr},\\
S^{\dagger}_{21}(r) &= -Ma^2\bar{T}/(\bar{U}-c)^2 - (\gamma-2)\,Ma^4,\\
S^{\dagger}_{22}(r) &= \frac{\bar{T}'^2}{\alpha^4(\bar{U}-c)^4} - \frac{3Ma^2\bar{T}}{\alpha^2(\bar{U}-c)^2},\\
S^{\dagger}_{23}(r) &= \frac{4\bar{T}\bar{T}'}{\alpha^2(\bar{U}-c)^4} - \frac{2(\gamma+1)Ma^2\bar{U}'\bar{T}}{\alpha^2(\bar{U}-c)^3} - \frac{6Ma^4\bar{T}'}{\alpha^2(\bar{U}-c)^2};
\end{aligned}\right\} \tag{C3}$$

$$\left.\begin{aligned}
S^{\dagger}_{30}(r) &= 2Ma^2\bar{U}'\,\tilde{J}^{\pm}_{r1}(r) - \bar{T}'\,\tilde{J}^{\pm}_{r2}(r) + 4Ma^2(\bar{U}-c)p_{Mr},\\
S^{\dagger}_{31}(r) &= -(3\gamma-1)\,Ma^4(\bar{U}-c) - (\gamma-1)\,Ma^2\bar{T}/(\bar{U}-c),\\
S^{\dagger}_{32}(r) &= \frac{\bar{T}^2(\bar{U}''-\bar{U}'/r)}{\alpha^4(\bar{U}-c)^4} - \frac{6Ma^2\bar{T}}{\alpha^2(\bar{U}-c)} + \frac{\bar{T}'^2}{\alpha^4(\bar{U}-c)^3} + \frac{2\bar{U}'\bar{T}'\bar{T}}{\alpha^2(\bar{U}-c)^4},\\
S^{\dagger}_{33}(r) &= \frac{8\bar{T}'\bar{T}}{\alpha^2(\bar{U}-c)^3} + \frac{(\gamma-9)\,Ma^2\bar{T}'}{\alpha^2(\bar{U}-c)} - \frac{2(\gamma+2)\,Ma^2\bar{U}'\bar{T}}{\alpha^2(\bar{U}-c)^2}.
\end{aligned}\right\} \tag{C4}$$

Appendix D. Derivations for $\dot{r}_T$ (3.27) and $\bar{V}_c$ (3.28)

With the prescribed mean axial velocity and temperature profiles, the transverse velocity and the axial variation of the shear-layer thickness, which play a leading-order role in the dynamics of CS, can be obtained from the compressible boundary-layer equations

$$\frac{\partial r\bar{\rho}\bar{U}}{\partial\tilde{x}} + \frac{\partial r\bar{\rho}\bar{V}}{\partial r} = 0, \tag{D1}$$

$$\bar{\rho}\bar{U}\frac{\partial\bar{U}}{\partial\tilde{x}} + \bar{\rho}\bar{V}\frac{\partial\bar{U}}{\partial r} = \frac{\partial}{\partial r}\mu_t\frac{\partial\bar{U}}{\partial r}. \tag{D2}$$

https://doi.org/10.1017/jfm.2022.252 Published online by Cambridge University Press

Using (D1), we may rewrite (D2) as

$$\frac{\partial r\bar{\rho}\bar{U}\bar{U}}{\partial\tilde{x}}+\frac{\partial r\bar{\rho}\bar{V}\bar{U}}{\partial r}=r\frac{\partial}{\partial r}\left(\mu_t\frac{\partial\bar{U}}{\partial r}\right)\quad(0\leqslant r<r_c),\tag{D3a}$$

$$\frac{\partial r\bar{\rho}\bar{U}(\bar{U}-\bar{U}_+)}{\partial\tilde{x}}+\frac{\partial r\bar{\rho}\bar{V}(\bar{U}-\bar{U}_+)}{\partial r}=r\frac{\partial}{\partial r}\left(\mu_t\frac{\partial\bar{U}}{\partial r}\right)\quad(r>r_c),\tag{D3b}$$

where μ_t is the eddy viscosity introduced in the closure model for the time-averaged Reynolds stresses.

On noting that $\bar{\rho}=\bar{T}^{-1}$, the equations can be integrated with respect to r from 0 to ∞ first, and then integrated with respect to $\tilde{x}$ again, to obtain

$$\frac{1}{r_c}\int_0^{r_c}\frac{\bar{U}^2}{\bar{T}}\,r\,\mathrm{d}r+\frac{1}{r_c}\int_{r_c}^{\infty}\frac{\bar{U}(\bar{U}-\bar{U}_+)}{\bar{T}}\,r\,\mathrm{d}r=\mathscr{C}_\infty^{(1)}+\int_{\tilde{x}_N}^{\tilde{x}}\mathscr{C}_{V,0}(\xi)\,\mathrm{d}\xi,\tag{D4}$$

where $\mathscr{C}_\infty^{(1)}$ is a constant and

$$\mathscr{C}_{V,0}(\tilde{x})=-\bar{U}_+\frac{\bar{V}_{c,0}(\tilde{x})}{\bar{T}_{c,0}(\tilde{x})}-\frac{1}{r_c}\int_0^{\infty}\mu_t\bar{U}'\,\mathrm{d}r.\tag{D5}$$

After performing the substitution (3.23), equation (D4) becomes

$$\frac{1}{r_c}\int_{\eta^\dagger_{a,0}}^{\eta^\dagger_{c,0}}\frac{\bar{U}^2}{\bar{T}}\,\eta^\ddagger\,\mathrm{d}\eta^\dagger+\frac{1}{r_c}\int_{\eta^\dagger_{c,0}}^{\infty}\frac{\bar{U}(\bar{U}-\bar{U}_+)}{\bar{T}}\,\eta^\ddagger\,\mathrm{d}\eta^\dagger=\frac{1}{\delta_T^2}\left[\mathscr{C}_\infty^{(1)}+\int_{\tilde{x}_N}^{\tilde{x}}\mathscr{C}_{V,0}(\xi)\,\mathrm{d}\xi\right],\tag{D6}$$

where we have put

$$\eta^\ddagger(\tilde{x})=\eta^\dagger-\eta_c^\dagger+r_T/\delta_T,\quad\eta^\dagger_{c,0}(\tilde{x})=\eta_c^\dagger+(r_c-r_T)/\delta_T,\quad\eta^\dagger_{a,0}(\tilde{x})=\eta_c^\dagger-r_T/\delta_T.\tag{D7a–c}$$

Differentiating (D6) with respect to $\tilde{x}$, we have

$$\begin{aligned}&\left(\dot{r}_T-r_T\dot{\delta}_T/\delta_T\right)\mathscr{C}_{U,0}(\tilde{x})/r_c-\bar{U}_+\left(\bar{U}_{c,0}/\bar{T}_{c,0}\right)\left[\dot{r}_T+(r_c-r_T)\dot{\delta}_T/\delta_T\right]\\&\quad=\mathscr{C}_{V,0}(\tilde{x})-2\left(\dot{\delta}_T/\delta_T\right)\left[\mathscr{C}_\infty^{(1)}+\int_{\tilde{x}_N}^{\tilde{x}}\mathscr{C}_{V,0}(\xi)\,\mathrm{d}\xi\right],\end{aligned}\tag{D8}$$

where the quantities with subscript '$c,0$' denote the values of the mean flow at the neutral-position critical level $r=r_c$, and

$$\mathscr{C}_{U,0}(\tilde{x})=\delta_T\left[\int_{\eta^\dagger_{a,0}}^{\infty}\frac{\bar{U}^2}{\bar{T}}\,\mathrm{d}\eta^\dagger-\bar{U}_+\int_{\eta^\dagger_{c,0}}^{\infty}\frac{\bar{U}}{\bar{T}}\,\mathrm{d}\eta^\dagger\right].\tag{D9}$$

The scaled mean radial velocity $\bar{V}$ can be derived from the continuity equation (D1) by defining the stream function $\Psi_B[\eta^\dagger(\tilde{x},r)]$ or $\Psi[\eta^\dagger(\tilde{x},r),\tilde{x}]$ such that

$$r\bar{\rho}\bar{U}=\frac{\partial\Psi_B}{\partial r}=\frac{1}{\delta_T}\frac{\partial\Psi}{\partial\eta^\dagger},\tag{D10a}$$

$$r\bar{\rho}\bar{V}=-\frac{\partial\Psi_B}{\partial\tilde{x}}=\frac{1}{\delta_T}\left[\dot{r}_T+(\eta^\dagger-\eta_c^\dagger)\dot{\delta}_T\right]\frac{\partial\Psi}{\partial\eta^\dagger}-\frac{\partial\Psi}{\partial\tilde{x}}.\tag{D10b}$$

https://doi.org/10.1017/jfm.2022.252 Published online by Cambridge University Press

Equation (D10*a*) is integrated to obtain

$$\Psi = \delta_T^2 \int_{\eta_{a,0}^\dagger}^{\eta^\dagger} \frac{\bar{U}(\eta^\star)}{\bar{T}(\eta^\star)} \eta^\ddagger(\tilde{x}, \eta^\star)\, \mathrm{d}\eta^\star + \psi_T(\tilde{x}), \tag{D11}$$

where ψ_T is an arbitrary function of $\tilde{x}$. Differentiation of (D11) with respect to $\tilde{x}$ gives

$$\begin{aligned}\bar{V}(\eta^\dagger) = \frac{\bar{T}(\eta^\dagger)}{\delta_T \eta^\ddagger} \Bigg\{ \delta_T \left[\dot{r}_T + (\eta^\dagger - \eta_c^\dagger)\dot{\delta}_T \right] \frac{\bar{U}(\eta^\dagger)}{\bar{T}(\eta^\dagger)} \eta^\ddagger - \dot{\psi}_T \\ - \frac{2 r_T \dot{\delta}_T}{\delta_T} F_{\bar{V}}^{(1)}(\eta^\dagger) - (\dot{r}_T - r_T \dot{\delta}_T/\delta_T) F_{\bar{V}}^{(0)}(\eta^\dagger) \Bigg\},\end{aligned} \tag{D12}$$

where we have put

$$F_{\bar{V}}^{(i)}(\eta^\dagger) = \frac{\delta_T^{i+1}}{r_T^i} \int_{\eta_{a,0}^\dagger}^{\eta^\dagger} \frac{\bar{U}(\eta^\star)}{\bar{T}(\eta^\star)} \left(\eta^\star - \eta_c^\dagger + \frac{r_T}{\delta_T} \right)^i \mathrm{d}\eta^\star, \quad i = 0, 1. \tag{D13}$$

Unlike a planar mixing layer, an axisymmetric shear layer does not extend to $-\infty$; rather, $\eta^\dagger$ approaches the finite value $\eta_a^\dagger$ at $r = 0$, where $\bar{V}(\eta^\dagger \to \eta_a^\dagger) = 0$. This imposes two conditions on the expression (D12): (i) the value of the expression in the braces must be zero at $\eta^\dagger = \eta_a^\dagger$, which leads to

$$\dot{\psi}_T = 0; \tag{D14}$$

(ii) the derivative of the expression in the braces with respect to $\eta^\dagger$ at $\eta^\dagger = \eta_a^\dagger$ must also vanish, which turns out to be true automatically.

Specifically, at the neutral position $\tilde{x} = \tilde{x}_N$ we have $\delta_T(\tilde{x}_N) = \delta = 1$ and $r_T(\tilde{x}_N) = r_c$. Setting $\tilde{x} = \tilde{x}_N$ in (D8) and (D12), we obtain the equations for $\dot{r}_T$ and $\bar{V}_c = \bar{V}(\eta^\dagger = \eta_{c,0}^\dagger)$ at the neutral position as

$$\left[\dot{r}_T/r_c - \dot{\delta}_T/\delta \right] \mathscr{C}_\infty^{(0)} - \bar{U}_+ \left(\bar{U}_c/\bar{T}_c \right) \dot{r}_T = -\left[\bar{U}_+ \left(\bar{V}_c/\bar{T}_c \right) + \mathscr{C}_\mu \right] - 2\mathscr{C}_\infty^{(1)} \dot{\delta}_T/\delta, \tag{D15a}$$

$$\bar{V}_c = \bar{T}_c \left[\left(\bar{U}_c/\bar{T}_c \right) \dot{r}_T - 2\mathscr{C}_c^{(1)} \dot{\delta}_T/\delta - \left(\dot{r}_T/r_c - \dot{\delta}_T/\delta \right) \mathscr{C}_c^{(0)} \right], \tag{D15b}$$

where

$$\left.\begin{aligned}\mathscr{C}_\infty^{(i)} = \frac{\delta^{i+1}}{r_c^i} \left[\int_{\eta_a^\dagger}^{\infty} \frac{\bar{U}^2}{\bar{T}} \left(\eta^\dagger - \eta_c^\dagger + \frac{r_c}{\delta} \right)^i \mathrm{d}\eta^\dagger - \bar{U}_+ \int_{\eta_c^\dagger}^{\infty} \frac{\bar{U}}{\bar{T}} \left(\eta^\dagger - \eta_c^\dagger + \frac{r_c}{\delta} \right)^i \mathrm{d}\eta^\dagger \right], \\ \mathscr{C}_c^{(i)} = F_{\bar{V}}^{(i)}(\eta_c^\dagger), \quad \mathscr{C}_\mu = \frac{\delta}{r_c} \int_{\eta_{a,0}^\dagger}^{\infty} \mu_t \bar{U}'\, \mathrm{d}\eta^\dagger.\end{aligned}\right\} \tag{D16}$$

sAmong these, $\mathscr{C}_\infty^{(i)}$ follows from setting $\tilde{x} = \tilde{x}_N$ in (D6). The system (D15) is solved to obtain (3.27) and (3.28).

To determine the profile of the eddy viscosity $\mu_t(\eta^\dagger)$, we assume that the shear-layer thickness $\delta_T \propto \sqrt{1 + 2\tilde{x}}$, and the axial momentum equation becomes, coupled with an

https://doi.org/10.1017/jfm.2022.252 Published online by Cambridge University Press

auxiliary function $\bar{G}(\eta^\dagger)$,

$$\begin{cases} \dfrac{\mathrm{d}}{\mathrm{d}\eta^\dagger}\left(\mu_t \dfrac{\mathrm{d}\bar{U}}{\mathrm{d}\eta^\dagger}\right) + \dfrac{\bar{G}}{\eta^\dagger - \eta_c^\dagger + r_c/\delta}\dfrac{\mathrm{d}\bar{U}}{\mathrm{d}\eta^\dagger} = 0, & \text{(D17}a\text{)} \\ \dfrac{\mathrm{d}\bar{G}}{\mathrm{d}\eta^\dagger} = \delta\,\dfrac{\bar{U}}{\bar{T}}\left[\dot{r}_T + \dfrac{r_c}{\delta}\,\dot{\delta}_T + 2(\eta^\dagger - \eta_c^\dagger)\dot{\delta}_T\right], & \text{(D17}b\text{)} \end{cases}$$

subject to the boundary conditions

$$\left(\mu_t, \bar{G}\right) \to \left(\mu_{t,a}, 0\right) \quad \text{as } \eta^\dagger \to \eta_a^\dagger, \tag{D18}$$

where $\mu_{t,a}$ is the value of the eddy viscosity on the axis to be determined together with $\dot{r}_T$ and $\bar{V}_c$. In fact, if the energy equation is included into (D17), then we have

$$\frac{1}{Pr_T}\frac{\mathrm{d}}{\mathrm{d}\eta^\dagger}\mu_t\frac{\mathrm{d}\bar{T}}{\mathrm{d}\eta^\dagger} + \bar{G}\frac{\mathrm{d}\bar{T}}{\mathrm{d}\eta^\dagger} + (\gamma-1)\,Ma^2\mu_t\frac{\mathrm{d}\bar{U}}{\mathrm{d}\eta^\dagger}\frac{\mathrm{d}\bar{U}}{\mathrm{d}\eta^\dagger} = 0, \tag{D19}$$

which is satisfied by (3.26) if the turbulent Prandtl number Pr_T is unity.

References

Afsar, M.Z., Sescu, A. & Leib, S.J. 2019*a* Modelling and prediction of the peak-radiated sound in subsonic axisymmetric air jets using acoustic analogy-based asymptotic analysis. *Phil. Trans. R. Soc. Lond.* A **377** (2159), 20190073.

Afsar, M.Z., Sescu, A. & Sassanis, V. 2019*b* Effect of non-parallel mean flow on the acoustic spectrum of heated supersonic jets: explanation of 'jet quietening'. *Phys. Fluids* **31** (10), 105107.

Baqui, Y.B., Agarwal, A., Cavalieri, A.V.G. & Sinayoko, S. 2015 A coherence-matched linear source mechanism for subsonic jet noise. *J. Fluid Mech.* **776**, 235–267.

Beavers, G.S. & Wilson, T.A. 1970 Vortex growth in jets. *J. Fluid Mech.* **44**, 97–112.

Bechert, D. & Pfizenmaier, E. 1975 On the amplification of broad band jet noise by a pure tone excitation. *J. Sound Vib.* **43** (3), 581–587.

Bechert, D.W. & Pfizenmaier, E. 1977 Amplification of jet noise by a higher-mode acoustical excitation. *AIAA J.* **15** (9), 1268–1271.

Bogey, C. & Bailly, C. 2007 An analysis of the correlations between the turbulent flow and the sound pressure fields of subsonic jets. *J. Fluid Mech.* **583**, 71–97.

Bogey, C., Bailly, C. & Juvé, D. 2003 Noise investigation of a high subsonic, moderate Reynolds number jet using a compressible large eddy simulation. *Theor. Comput. Fluid Dyn.* **16** (4), 273–297.

Bogey, C. & Sabatini, R. 2019 Effects of nozzle-exit boundary-layer profile on the initial shear-layer instability, flow field and noise of subsonic jets. *J. Fluid Mech.* **876**, 288–325.

Brès, G.A., Jaunet, V., Le Rallic, M., Jordan, P., Towne, A., Schmidt, O., Colonius, T., Cavalieri, A.V. & Lele, S.K. 2016 Large eddy simulation for jet noise: azimuthal decomposition and intermittency of the radiated sound. In *22nd AIAA/CEAS Aeroacoustics Conference, AIAA Paper* 2016-3050.

Brès, G.A., Jordan, P., Jaunet, V., Rallic, M.L., Cavalieri, A.V.G., Towne, A., Lele, S.K., Colonius, T. & Schmidt, O.T. 2018 Importance of the nozzle-exit boundary-layer state in subsonic turbulent jets. *J. Fluid Mech.* **851**, 83–124.

Bridges, J. & Hussain, F. 1992 Direct evaluation of aeroacoustic theory in a jet. *J. Fluid Mech.* **240**, 469–501.

Bridges, J.E. & Hussain, A.K.M.F. 1987 Roles of initial condition and vortex pairing in jet noise. *J. Sound Vib.* **117** (2), 289–311.

Cavalieri, A.V.G. & Agarwal, A. 2014 Coherence decay and its impact on sound radiation by wavepackets. *J. Fluid Mech.* **748**, 399–415.

Cavalieri, A.V.G., Daviller, G., Comte, P., Jordan, P., Tadmor, G. & Gervais, Y. 2011*a* Using large eddy simulation to explore sound-source mechanisms in jets. *J. Sound Vib.* **330** (17), 4098–4113.

Cavalieri, A.V.G., Jordan, P., Agarwal, A. & Gervais, Y. 2011*b* Jittering wave-packet models for subsonic jet noise. *J. Sound Vib.* **330** (18–19), 4474–4492.

https://doi.org/10.1017/jfm.2022.252 Published online by Cambridge University Press

CAVALIERI, A.V.G., JORDAN, P., COLONIUS, T. & GERVAIS, Y. 2012 Axisymmetric superdirectivity in subsonic jets. *J. Fluid Mech.* **704**, 388–420.
CAVALIERI, A.V.G., JORDAN, P., GERVAIS, Y., WEI, M. & FREUND, J.B. 2010 Intermittent sound generation and its control in a free-shear flow. *Phys. Fluids* **22** (11), 115113.
CAVALIERI, A.V.G., JORDAN, P. & LESSHAFFT, L. 2019 Wave-packet models for jet dynamics and sound radiation. *Appl. Mech. Rev.* **71** (2), 020802.
CAVALIERI, A.V.G., RODRIGUEZ, D., JORDAN, P., COLONIUS, T. & GERVAIS, Y. 2013 Wavepackets in the velocity field of turbulent jets. *J. Fluid Mech.* **730**, 559–592.
CHEUNG, L.C. & LELE, S.K. 2009 Linear and nonlinear processes in two-dimensional mixing layer dynamics and sound radiation. *J. Fluid Mech.* **625**, 321–351.
COHEN, J. & WYGNANSKI, I. 1987 The evolution of instabilities in the axisymmetric jet. Part 1. The linear growth of disturbances near the nozzle. *J. Fluid Mech.* **176**, 191–219.
CORKE, T.C., SHAKIB, F. & NAGIB, H.M. 1991 Mode selection and resonant phase locking in unstable axisymmetric jets. *J. Fluid Mech.* **223**, 253–311.
CRAWLEY, M., GEFEN, L., KUO, C.W., SAMIMY, M. & CAMUSSI, R. 2018 Vortex dynamics and sound emission in excited high-speed jets. *J. Fluid Mech.* **839**, 313–347.
CRIGHTON, D.G. & HUERRE, P. 1990 Shear-layer pressure fluctuations and superdirective acoustic sources. *J. Fluid Mech.* **220**, 355–368.
CROW, S.C. 1970 Aerodynamic sound emission as a singular perturbation problem. *Stud. Appl. Maths* **49** (1), 21–46.
CROW, S.C. & CHAMPAGNE, F.H. 1971 Orderly structure in jet turbulence. *J. Fluid Mech.* **48**, 547–591.
FFOWCS WILLIAMS, J.E. 1969 Hydrodynamic noise. *Annu. Rev. Fluid Mech.* **1** (1), 197–222.
FFOWCS WILLIAMS, J.E. 1977 Aeroacoustics. *Annu. Rev. Fluid Mech.* **9** (1), 447–468.
FFOWCS WILLIAMS, J.E. & KEMPTON, A.J. 1978 The noise from the large-scale structure of a jet. *J. Fluid Mech.* **84**, 673–694.
FONTAINE, R.A., ELLIOTT, G.S., AUSTIN, J.M. & FREUND, J.B. 2015 Very near-nozzle shear-layer turbulence and jet noise. *J. Fluid Mech.* **770**, 27–51.
FREUND, J.B. 2001 Noise sources in a low-Reynolds-number turbulent jet at Mach 0.9. *J. Fluid Mech.* **438**, 277–305.
FU, Z., AGARWAL, A., CAVALIERI, A.V.G., JORDAN, P. & BRÈS, G.A. 2017 Turbulent jet noise in the absence of coherent structures. *Phys. Rev. Fluids* **2** (6), 064601.
GARNAUD, X., LESSHAFFT, L., SCHMID, P.J. & HUERRE, P. 2013 The preferred mode of incompressible jets: linear frequency response analysis. *J. Fluid Mech.* **716**, 189–202.
GASTER, M., KIT, E. & WYGNANSKI, I. 1985 Large-scale structures in a forced turbulent mixing layer. *J. Fluid Mech.* **150**, 23–39.
GOLDSTEIN, M.E. 1984 Aeroacoustics of turbulent shear flows. *Annu. Rev. Fluid Mech.* **16** (1), 263–285.
GOLDSTEIN, M.E. 2001 An exact form of Lilley's equation with a velocity quadrupole/temperature dipole source term. *J. Fluid Mech.* **443**, 231–236.
GOLDSTEIN, M.E. 2003 A generalized acoustic analogy. *J. Fluid Mech.* **488**, 315–333.
GOLDSTEIN, M.E. 2005 On identifying the true sources of aerodynamic sound. *J. Fluid Mech.* **526**, 337–347.
GOLDSTEIN, M.E. 2011 Recent developments in the application of the generalized acoustic analogy to jet noise prediction. *Intl J. Aeroacoust.* **10** (2–3), 89–115.
GOLDSTEIN, M.E. & LEIB, S.J. 2005 The role of instability waves in predicting jet noise. *J. Fluid Mech.* **525**, 37–72.
GOLDSTEIN, M.E. & LEIB, S.J. 2008 The aeroacoustics of slowly diverging supersonic jets. *J. Fluid Mech.* **600**, 291–337.
GOLDSTEIN, M.E., SESCU, A. & AFSAR, M.Z. 2012 Effect of non-parallel mean flow on the Green's function for predicting the low-frequency sound from turbulent air jets. *J. Fluid Mech.* **695**, 199–234.
GRINSTEIN, F.F., ORAN, E.S. & BORIS, J.P. 1987 Direct numerical simulation of axisymmetric jets. *AIAA J.* **25** (1), 92–98.
HABERMAN, R. 1972 Critical layers in parallel shear flows. *Stud. Appl. Maths* **51**, 139–161.
HARPER-BOURNE, M. & FISHER, M.J. 1974 The noise from shock waves in supersonic jets. In *Noise Mechanisms, AGARD-CP-131*, pp. 11.1–11.13.
HILEMAN, J.I., THUROW, B.S., CARABALLO, E.J. & SAMIMY, M. 2005 Large-scale structure evolution and sound emission in high-speed jets: real-time visualization with simultaneous acoustic measurements. *J. Fluid Mech.* **544**, 277–307.
HUSSAIN, A.K.M.F. & HASAN, M.A.Z. 1985 Turbulence suppression in free turbulent shear flows under controlled excitation. Part 2. Jet-noise reduction. *J. Fluid Mech.* **150**, 159–168.
HUSSAIN, A.K.M.F. & REYNOLDS, W.C. 1972 The mechanics of an organized wave in turbulent shear flow. Part 2. Experimental results. *J. Fluid Mech.* **54**, 241–261.

https://doi.org/10.1017/jfm.2022.252 Published online by Cambridge University Press

JEUN, J., NICHOLS, J.W. & JOVANOVIĆ, M.R. 2016 Input–output analysis of high-speed axisymmetric isothermal jet noise. *Phys. Fluids* **28** (4), 047101.
JORDAN, P. & COLONIUS, T. 2013 Wave packets and turbulent jet noise. *Annu. Rev. Fluid Mech.* **45**, 173–195.
JUVÉ, D., SUNYACH, M. & COMTE-BELLOT, G. 1980 Intermittency of the noise emission in subsonic cold jets. *J. Sound Vib.* **71** (3), 319–332.
KEARNEY-FISCHER, M., SINHA, A. & SAMIMY, M. 2013 Intermittent nature of subsonic jet noise. *AIAA J.* **51** (5), 1142–1155.
KIBENS, V. 1980 Discrete noise spectrum generated by acoustically excited jet. *AIAA J.* **18** (4), 434–441.
LIGHTHILL, M.J. 1952 On sound generated aerodynamically. I. General theory. *Proc. R. Soc. Lond.* A **211**, 564–587.
LILLEY, G.M. 1974 On the noise from jets. In *Noise Mechanisms, AGARD-CP-131*, pp. 13.1–13.12.
LIU, J.T.C. 1974 Developing large-scale wavelike eddies and the near jet noise field. *J. Fluid Mech.* **62**, 437–464.
LIU, J.T.C. 1989 Coherent structures in transitional and turbulent free shear flows. *Annu. Rev. Fluid Mech.* **21**, 285–315.
LORTEAU, M., CLÉRO, F. & VUILLOT, F. 2015 Analysis of noise radiation mechanisms in hot subsonic jet from a validated large eddy simulation solution. *Phys. Fluids* **27** (7), 075108.
MICHALKE, A. 1965 On spatially growing disturbances in an inviscid shear layer. *J. Fluid Mech.* **23**, 521–544.
MICHALKE, A. & FREYMUTH, P. 1966 The instability and the formation of vortices in a free boundary layer. In *AGARD Conference Proc. on Separated Flows, Part 2* (ed. J.J. Ginoux & H. Eubelhac), pp. 575–595.
MICHALKE, A. & FUCHS, H.V. 1975 On turbulence and noise of an axisymmetric shear flow. *J. Fluid Mech.* **70**, 179–205.
MIKSAD, R.W. 1973 Experiments on nonlinear interactions in the transition of a free shear layer. *J. Fluid Mech.* **59**, 1–21.
MOLLO-CHRISTENSEN, E., KOLPIN, M.A. & MARTUCCELLI, J.R. 1964 Experiments on jet flows and jet noise far-field spectra and directivity patterns. *J. Fluid Mech.* **18**, 285–301.
MOORE, C.J. 1977 The role of shear-layer instability waves in jet exhaust noise. *J. Fluid Mech.* **80**, 321–367.
NARAYANAN, S., BARBER, T.J. & POLAK, D.R. 2002 High subsonic jet experiments: turbulence and noise generation studies. *AIAA J.* **40** (3), 430–437.
NICHOLAS, J.W. & LELE, S.K. 2011 Global modes and transient response of a cold supersonic jet. *J. Fluid Mech.* **669**, 225–241.
PASCHEREIT, C.O., OSTER, D., LONG, T.A., FIEDLER, H.E. & WYGNANSKI, I. 1992 Flow visualization of interactions among large coherent structures in an axisymmetric jet. *Exp. Fluids* **12** (3), 189–199.
PASCHEREIT, C.O., WYGNANSKI, I. & FIEDLER, H.E. 1995 Experimental investigation of subharmonic resonance in an axisymmetric jet (referred to as 'PWF'). *J. Fluid Mech.* **283**, 365–407.
PETERSON, L.F. & HAMA, F.R. 1978 Instability and transition of the axisymmetric wake of a slender body of revolution. *J. Fluid Mech.* **88** (1), 71–96.
PHILLIPS, O.M. 1960 On the generation of sound by supersonic turbulent shear layers. *J. Fluid Mech.* **9**, 1–28.
RAMAN, G. 1999 Supersonic jet screech: half-century from Powell to the present. *J. Sound Vib.* **225** (3), 543–571.
RAMAN, G., RICE, E.J. & RESHOTKO, E. 1994 Mode spectra of natural disturbances in a circular jet and the effect of acoustic forcing. *Exp. Fluids* **17** (6), 415–426.
RONNEBERGER, D. & ACKERMANN, U. 1979 Experiments on sound radiation due to non-linear interaction of instability waves in a turbulent jet. *J. Sound Vib.* **62** (1), 121–129.
ROSHKO, A. 1976 Structure of turbulent shear flows: a new look. *AIAA J.* **14** (10), 1349–1357.
SAMIMY, M., KIM, J.-H., KASTNER, J., ADAMOVICH, I. & UTKIN, Y. 2007 Active control of high-speed and high-Reynolds-number jets using plasma actuators. *J. Fluid Mech.* **578**, 305–330.
SANDHAM, N.D. & SALGADO, A.M. 2008 Nonlinear interaction model of subsonic jet noise. *Phil. Trans. R. Soc. Lond.* A **366** (1876), 2745–2760.
SCHMIDT, O.T., TOWNE, A., COLONIUS, T., CAVALIERI, A.V.G., JORDAN, P. & BRÈS, G.A. 2017 Wavepackets and trapped acoustic modes in a turbulent jet: coherent structure eduction and global stability. *J. Fluid Mech.* **825**, 1153–1181.
SEINER, J. 1984 Advances in high speed jet aeroacoustics. In *9th Aeroacoustics Conference, AIAA Paper* 1984-2275.
SINAYOKO, S., AGARWAL, A. & HU, Z. 2011 Flow decomposition and aerodynamic sound generation. *J. Fluid Mech.* **668**, 335–350.
SINHA, A., RODRIGUEZ, D., BRÈS, G.A. & COLONIUS, T. 2014 Wavepacket models for supersonic jet noise. *J. Fluid Mech.* **742**, 71–95.
SPARKS, C.A. & WU, X. 2008 Nonlinear development of subsonic modes on compressible mixing layers: a unified strongly nonlinear critical-layer theory. *J. Fluid Mech.* **614**, 105–144.

https://doi.org/10.1017/jfm.2022.252 Published online by Cambridge University Press

SUPONITSKY, V., SANDHAM, N.D. & MORFEY, C.L. 2010 Linear and nonlinear mechanisms of sound radiation by instability waves in subsonic jets. *J. Fluid Mech.* **658**, 509–538.
SUZUKI, T. 2013 Coherent noise sources of a subsonic round jet investigated using hydrodynamic and acoustic phased-microphone arrays. *J. Fluid Mech.* **730**, 659–698.
SUZUKI, T. & COLONIUS, T. 2006 Instability waves in a subsonic round jet detected using a near-field phased microphone array. *J. Fluid Mech.* **565**, 197–226.
TAM, C., GOLEBIOWSKI, M. & SEINER, J. 1996 On the two components of turbulent mixing noise from supersonic jets. In *2nd AIAA/CEAS Aeroacoustics Conference, AIAA Paper* 1996-1716.
TAM, C.K.W. 1991 Broadband shock-associated noise from supersonic jets in flight. *J. Sound Vib.* **151** (1), 131–147.
TAM, C.K.W. 1995 Supersonic jet noise. *Annu. Rev. Fluid Mech.* **27** (1), 17–43.
TAM, C.K.W. 2019 A phenomenological approach to jet noise: the two-source model. *Phil. Trans. R. Soc. Lond.* A **377** (2159), 20190078.
TAM, C.K.W. & BURTON, D.E. 1984 Sound generated by instability waves of supersonic flow. Part 2. Axisymmetric jets. *J. Fluid Mech.* **138**, 273–295.
TAM, C.K.W. & MORRIS, P.J. 1980 The radiation of sound by the instability waves of a compressible plane turbulent shear layer. *J. Fluid Mech.* **98**, 349–381.
TAM, C.K.W., VISWANATHAN, K., AHUJA, K.K. & PANDA, J. 2008 The sources of jet noise: experimental evidence. *J. Fluid Mech.* **615**, 253–292.
TANNA, H.K. & MORRIS, P.J. 1977 In-flight simulation experiments on turbulent jet mixing noise. *J. Sound Vib.* **53** (3), 389–405.
TOWNE, A. & COLONIUS, T. 2015 One-way spatial integration of hyperbolic equations. *J. Comput. Phys.* **300**, 844–861.
VISWANATHAN, K. 2004 Aeroacoustics of hot jets. *J. Fluid Mech.* **516**, 39–82.
VISWANATHAN, K. 2008 Investigation of noise source mechanisms in subsonic jets. *AIAA J.* **46** (8), 2020–2032.
VISWANATHAN, K. 2010 Distributions of noise sources in heated and cold jets: are they different? *Intl J. Aeroacoust.* **9** (4–5), 589–625.
WAN, Z., YANG, H., ZHANG, X. & SUN, D. 2016 Instability waves and aerodynamic noise in a subsonic transitional turbulent jet. *Eur. J. Mech. (*B*/Fluids)* **57**, 192–203.
WU, X. 2005 Mach wave radiation of nonlinearly evolving supersonic instability modes in shear layers. *J. Fluid Mech.* **523**, 121–159.
WU, X. 2019 Nonlinear theories for shear-flow instabilities: physical insights and practical implications. *Annu. Rev. Fluid Mech.* **51**, 421–485.
WU, X. & HUERRE, P. 2009 Low-frequency sound radiated by a nonlinear modulated wavepacket of helical modes on a subsonic circular jet. *J. Fluid Mech.* **637**, 173–211.
WU, X. & TIAN, F. 2012 Spectral broadening and flow randomization in free shear layers. *J. Fluid Mech.* **706**, 431–469.
WU, X. & ZHANG, Z. 2019 First-principle description of acoustic radiation of shear flows. *Phil. Trans. R. Soc. Lond.* A **377** (2159), 20190077.
WU, X. & ZHUANG, X. 2016 Nonlinear dynamics of large-scale coherent structures in turbulent free shear layers. *J. Fluid Mech.* **787**, 396–439.
ZAMAN, K.B.M.Q. 1985 Far-field noise of a subsonic jet under controlled excitation. *J. Fluid Mech.* **152**, 83–111.
ZAMAN, K.B.M.Q. & HUSSAIN, A.K.M.F. 1980 Vortex pairing in a circular jet under controlled excitation. Part 1. General jet response. *J. Fluid Mech.* **101**, 449–491.
ZAMAN, K.B.M.Q. & HUSSAIN, A.K.M.F. 1981 Turbulence suppression in free shear flows by controlled excitation. *J. Fluid Mech.* **103**, 133–159.
ZAMAN, K.B.M.Q. & HUSSAIN, A.K.M.F. 1984 Natural large-scale structures in the axisymmetric mixing layer. *J. Fluid Mech.* **138**, 325–351.
ZHANG, Z. & WU, X. 2020 Nonlinear evolution and acoustic radiation of coherent structures in subsonic turbulent free shear layers (referred to as '[I]'). *J. Fluid Mech.* **884**, A10.

https://doi.org/10.1017/jfm.2022.252 Published online by Cambridge University Press